IPP-Report

Ahmed Hosny Abdelhameed

Fabrication and Optimization of Novel Thermally-Stable Tungsten Nitride Thin Films for Potential Applications in Nuclear Fusion Research

IPP 2018-04
Februar 2018

Fabrication and Optimization of Novel Thermally-Stable Tungsten Nitride Thin Films for Potential Applications in Nuclear Fusion Research

Master Thesis at Ulm University and Max Planck Institute for Plasma Physics in Munich

Ahmed Hosny Abdelhameed

ahmed.abdelhameed@uni-ulm.de

Academic supervisor: apl. Prof. Dr. Emanuele Poli

Thesis supervisor: Dr. habil. Wolfgang Jacob

Department of Physics
Ulm University

This thesis is submitted for the degree of
Master of Science

December 2017

To my mom who raised me with a love of science and supported me in all my pursuits.

Declaration

I hereby declare that except where specific reference is made to the work of others, the contents of this dissertation are original and have not been submitted in whole or in part for consideration for any other degree or qualification in this, or any other university. This dissertation is my own work and contains nothing which is the outcome of work done in collaboration with others, except as specified in the text and acknowledgments.

. . . . . .

Ahmed Hosny Abdelhameed

ahmed.abdelhameed@uni-ulm.de

December 2017

Acknowledgements

First and foremost, I would like to express my sincere gratitude to my advisor Prof. Emanuele Poli who lit up my passion for plasma physics and Nuclear fusion research. His professionalism, teaching style and enthusiasm for the topic made the lectures, I attend for him, the best I ever had in my life. In addition, I cannot be thankful enough for his never-ending support, accepting to supervise my thesis, making my stay at IPP very smooth and for never hesitating to help me. Equally, I would like to thank my research supervisor Dr. habil. Wolfgang Jacob for providing the topic, his continuous support of my M.Sc. thesis and the related research, for his patience, motivation, and immense knowledge. His guidance helped me in all the time of research and writing of this thesis. I also want to thank Prof. Dr. Ulrich Stroth for the opportunity to write my thesis at the E2M department. I am also grateful to Dr. Thomas Eich for giving me the first opportunity to get research experience at IPP through an internship at ASDEX Upgrade, besides, getting me into contact for this thesis topic. My sincere thanks also goes to Dr. Liang Gao for introducing me to all the experimental setups and his deep constructive discussions and encouragement. He was always making sure that I have all the necessary means and he provided an extensive amount of help so that the thesis comes out as it is now.

Getting through my dissertation required a lot of support from all my colleagues. Without their assistance and dedicated involvement in every step throughout the process, this thesis would have never been accomplished. I cannot begin to express my gratitude and appreciation for their support. Stefan Elgeti for teaching me XRD and helping me with the analysis. Dr. Martin Balden for SEM and CLM and his guidance towards better analysis. Dr. Armin Manhard for performing plasma loading and deutrium implantation in PlaQ, the operation of the high temperature ovens, his deep discussions and his fruitful suggestions, ideas and advices. Dr. Udo von Toussaint for his generous discussion time regarding the theoretical basics and the ion-beam analysis simulations. Till Hoeschen, first, for performing the XPS measurements, and his time for the data analysis I'm also grateful for his technical support during the period of my stay. I cannot be thankful enough for Thomas Duerbeck for providing almost every technical part I needed and his help to mount it or telling me how to get it, besides, performing the TDS measurements in TESS and the related calibrations and samples handling. Stefan Kapser for his supportive ideas, introducing me to sputtering deposition machine, as well as, his help with energy calibration of IBA. Dr. Klaus Schmid for his deep discussions regarding the back ground of IBA and his general advice towards better measurements and analysis. Rupert Brüderl for taking care of making the simple designs, for substrate holders in the deposition chamber, pieces of

art though metal machining in the workshop, I'm very grateful for him and all the workshop members who also helped me during the whole project with choosing the proper materials and doing the designs correctly. Gabriele Matern for specimens preparation and polishing in addition to SEM and FIB analysis. Dr. Johann Riesch for his support with Sputtering device and his discussions regarding better experiments. Dr. Hans Maier for his discussion time and his ideas for experimental methods. Rodrigo Arredondo for his discussion time regarding the sputtering process and his explanation in details. Martin Oberkofler for teaching me how to polish the graphite substrates and also for his discussion time. I'm very grateful for all the members of E2M department, especially, Biggy Perey for her administrative support during my stay. I'm also grateful to all the colleagues at IPP they have been unwavering in their personal and professional support during the time I spent at IPP.

In March 2017, I went to National Institute for Fusion Science (NIFS) in Toki, Japan, for few months to conduct experimental work. I would like to express my deepest gratitude to Prof. MASUZAKI, Suguru who provided me an opportunity to join his team as intern and gave access to the laboratory and research facilities. Without his precious support it would not be possible to conduct such research. He also conducted the GDOES analysis despite his tight schedule. My time there has been highly productive and an extraordinary experience. Much of the analysis presented in chapter III is owed to my time at NIFS. I must thank all the colleagues there, especially, Dr. TOKITANI, Masayuki, Prof. SAKAMOTO, Ryuichi and Mr. NAGATA, Daisuke for their precious time regarding TEM data analysis and their long discussion time. I would also like to thank Dr. YAJIMA, Miyuki for her special care during my stay there, besides, performing the SEM and TDS measurements as well as the data analysis. Moreover, I'm so grateful to Dr. HISHINUMA, Yoshimitsu for making time to teach me the nano-indentation technique and measuring the mechanical properties, as well as, his time for the data analysis and the discussion. Prof. YANAGI, Nagato for the introduction of super conducting engineering and his discussion time. Prof. SAKAKIBARA, Satoru for the introduction of plasma diagnostics in LHD. Dr. YASUHARA, Ryo for the introduction of laser applications in plasma diagnostics. Prof. Miyazawa, Junichi for the introduction of liquid metal divertor and the related material science issues. And all the stuff members there who made my stay very pleasant and always were open to answer my questions.

I would like to extend my appreciation to Prof. Laila Abulnasr, Prof. Sayed Abboudy and Dr. Mohamed Anas for their never-ending support since the first moment I got to know them, during my bachelor studies, and until now. I'm also so grateful to my best friend Mr. Ahmed Elsayed who has always been more than a brother to me.

Lastly, and most importantly, I would like to thank my family for all their love, support and encouragement. My mom who is the first one who believes in me, my brother who has always been in my back. and my sister who taught me the meaning of true love.

Abstract

Nitrogen is considered to be one of the seeding gases for radiative cooling in the divertor region of fusion devices such as ASDEX Upgrade and JET. Since tungsten is the chosen material for the divertor and is exposed directly to the plasma, it is necessary to comprehend the interaction between nitrogen and tungsten, as well as the effect on hydrogen isotopes interaction with tungsten. As WN_x layers formed by direct nitrogen implantation are too thin to allow a quantitative investigations of the interaction of N-implanted tungsten surfaces with hydrogen plasma. Magnetron-sputtered WN_x films were introduced as a model system to study such effects. In previous work, WN_x showed the ability to block the diffusion of hydrogen isotopes, however, the produced layers were not thermally stable and showed decomposition at temperatures around 850 K. To allow investigations at higher temperatures, it is desirable to develop such nitride system to be more stable at higher temperatures.

The layers considered in this thesis were produced via reactive magnetron sputtering in a mixture of argon and nitrogen. It was a hurdle to fabricate layers with thickness sufficient to allow proper characterization due to the huge residual stress in the layers which caused an instantaneous delamination (damage) of the layers once the vacuum is broken. Starting from that point, a series of optimizations was performed to find the proper deposition conditions to produce a certain phase.The following deposition parameters were varied: the nitrogen partial pressure, chamber total pressure, applied power RF or DC, current and voltage, substrate holder rotation speed,substrate bias voltage, substrate temperature. A special sample holder was designed to perform up to six depositions without breaking the vacuum or switching of the plasma in order to study the effect of each parameter as accurately as possible.

Ion Beam Analysis (IBA) was one of the main characterization techniques. More specifically, Rutherford backscattering spectroscopy (RBS) and nuclear reaction analysis (NRA) were used to quantify the elemental concentrations in the layers of mainly tungsten and nitrogen. As the tungsten-nitrogen system has many intermediate phases with partially comparable nitrogen atomic concentrations, it was a must to find a way to reduce the uncertainty due to the current measurements and the energy spread as much as possible. A new measurements procedure was developed to enable a more accurate determination of the nitrogen content in the WN_x layers. By depositing an identical, pure tungsten layer on top of all the WN_x layers the uncertainty in the evaluation of the RBS measurements was reduced to $\sim 2\%$. Additionally, NRA analysis was applied for thin WN_x layers to

independently cross check the nitrogen content. Furthermore, a variety of characterization techniques were applied to study the produced layers in more detail: X-Ray diffraction (XRD) was applied to determine the produced phase, thermal desorption spectroscopy (TDS) to study the thermal properties, X-ray photoelectron spectroscopy (XPS) to study the chemical bonding, glow-discharge optical emission spectroscopy (GDOES) to study impurities and the layers homogeneity, scanning electron microscope (SEM), energy-dispersive X-ray spectroscopy (EDX), electron backscatter diffraction (EBSD) and transmission electron microscopy (TEM) to study the micro-structure of the layers, and nanoindentation for mechanical properties estimation.

Three different phases could be distinguished by XRD, namely W_2N, WN and WN_2. W_2N was fabricated with crystallinity at least 15 times better than what is reported in literature. Since the crystallinity was improved and the possible amorphous fraction in the layers was minimized, the nitrogen release temperate became higher than 1300 K (which is closer to the predicted value of ~ 2100 K). Further step was taken towards the comprehension of the decomposition behavior as well as the substrate effect. Finally, the retention of deuterium in the WN_x layers showed a large reduction as a result of the optimization.

Table of contents

List of figures **xv**

List of tables **xxvii**

1 Introduction **1**

1.1 Fusion Energy and Fusion Reactor 1

1.1.1 Fusion 2

1.1.2 Tokamak 3

1.2 Plasma Facing Materials and Interaction 3

1.2.1 Nitrogen Interaction with Tungsten 4

1.3 Tungsten Nitride in the Lab 5

1.4 Thesis Goals and Outline 8

2 Experimental Methods **9**

2.1 Sample Preparation 9

2.1.1 Magnetron Sputtering 9

2.2 Characterization Techniques and Set-ups 13

2.2.1 X-ray Diffraction (XRD) 13

2.2.2 Ion Beam Analysis (IBA) 20

2.2.2.1 Rutherford Backscattering Spectroscopy (RBS) 23

2.2.2.2 Nuclear Reaction Analysis (NRA) 28

2.2.3 Thermal Desorption Spectroscopy (TDS) 29

2.2.4 Scanning Electron Microscope (SEM) 31

2.2.5 Transmission Electron Microscopy (TEM) . . . 32
2.2.5.1 Focused Ion Beam (FIB) . . . 35
2.2.5.2 Energy-Dispersive X-ray Spectroscopy (EDX) . . . 36
2.2.5.3 Electron Backscattered Diffraction (EBSD) . . . 37
2.2.6 X-ray Photoelectron Spectroscopy (XPS) . . . 37
2.2.7 Glow Discharge Optical Emission Spectrometry (GDOES) . . . 38
2.2.8 Nano Indenter . . . 39
2.3 Chapter Summary . . . 40

3 Progress in WN_x Fabrication 41
3.1 Main Characterization Techniques . . . 43
3.1.1 XRD Measurements . . . 43
3.1.2 More Accurate RBS Measurements . . . 44
3.2 Nitrogen Content vs. N_2-Partial Pressure . . . 45
3.3 Bias Effect . . . 49
3.4 Layers Micro-Structure Using SEM and TEM . . . 50
3.5 Annealing Effect . . . 51
3.6 Thermal Stability and Impurities Retention . . . 53
3.7 Mechanical Properties of WN_x . . . 58
3.8 Chapter Conclusion . . . 59

4 Optimized and Thermally-Stable Tungsten Nitride 63
4.1 Optimum Substrate Temperature . . . 63
4.1.1 Micro-Structure Improvement . . . 64
4.1.2 Crystal Structure and Orientation . . . 65
4.2 Calculation of WN_x Phases Density . . . 66
4.3 Analysis Using RBS . . . 66
4.3.1 Nitrogen Depth Profile . . . 67
4.3.2 N_2 Quantification Using RBS . . . 68
4.4 Porosity Estimation . . . 68

4.5 Thermal Stability of the Layers . . . 69
4.5.1 N_2 Quantification Using TDS . . . 71
4.6 An Approach to Understand the Desorption Behavior . . . 72
4.6.1 Thermal Expansion Coefficient of WN_x . . . 73
4.6.2 Substrate Material Effect . . . 75
4.6.3 Heat Treatment Effects on the Micro-Structure . . . 78
4.7 Residual Stress Evaluation . . . 79
4.8 Annealing Effect . . . 80
4.8.1 Heating Ramp Effect . . . 83
4.9 Chapter Summary . . . 84

5 Deuterium Retention in Tungsten Nitride 85
5.1 Deuterium Implantation via Plasma Exposure . . . 85
5.2 Deuterium Analysis Using NRA . . . 86
5.3 Deuterium Quantification Using NRA . . . 88
5.4 Deuterium Quantification Using TDS . . . 89
5.5 The Effect on the Micro-Structure . . . 91
5.6 Chapter Summary . . . 93

6 Conclusion and Outlook 95
6.1 Thesis Conclusion . . . 95
6.2 Outlook and Further Experiments . . . 95

References 97

Appendix A RBS and NRA Cross Section Data 103
A.1 RBS N_2 Cross Section . . . 103
A.2 RBS Cross Section of N_2, Si and C . . . 105
A.3 NRA . . . 106

Appendix B Specimen Preparation Using FIB 107

List of figures

1.1 A cross section comparison between all possible fusion fuel candidates as a function of energy in keV units showing that $D-T$ reaction (blue line) has the highest probability at the lowest energy [7]. 2

1.2 Detailed illustration of a tokamak showing the magnetic field coil (copper-color) and the plasma in the vessel (violet color) as well as the direction of the plasma current and the magnetic field lines (yellow lines)[10]. 3

1.3 (a) The structure of the tungsten divertor in ASDEX upgrade tokamak [13]. (b) Plasma discharge in ASDEX upgrade showing the interaction between plasma and the wall (magenta color) [14]. 4

1.4 Review of some the reported stable and intermediate phases of tungsten nitride with nitrogen atomic concentration and crystal structure information. [31] 6

1.5 Illustrations with nitrogen being the small blue spheres, tungsten the big lightblue spheres and red lines are the borders of the unit cells. (a) The cubic lattice structure of W_2N. (b) The unit cell of the hexagonal lattice of WN. (c) The unit cell of the rombohedral lattice of WN_2 7

1.6 Review of the lattice parameters of the reported stable and intermediate tungsten nitride phases at room temperature in nm units [30]. 7

2.1 A schematic drawing of magnetron sputtering, showing the working principle of the target and the magnetic field lines of the permanent magnets. Edited from [33] 10

2.2 Thorton's zone model as an example for the effect of the deposition conditions on the micro-structure of the deposited layers of pure elements. The typical micro-structures of deposited layers are the most favorable in the so-called T-zone. [34] 11

2.3 Real picture of the Denton device deposition chamber. The image shows a plasma ignited on both cathodes (for mixed-metals layers deposition) and the main components are indicated. 12

2.4 Calibration curve based on experimental results to estimate the thickness of the deposited layers as a function of the applied power. All the depositions were carried out for 60 *min*. The total chamber pressure was ~ 1 *Pa*. The black line represents depositions carried out in a gas mixtures of 50% Ar and 50% N_2. The red line represents depositions carried out in pure nitrogen atmosphere. The equations on the lines are empirical equations to roughly estimate the layer thickness in 60 *min* as a function of power. 13

2.5 Schematic view of the reflection of the waves form the crystallographic planes showing that the reflected waves will always have destructive interference except when the Bragg's condition is satisfied. At a certain 2θ angle a bright constructive interference occurs.[37] 14

2.6 Simple example of calculating the Miller indices and defining the lattice planes. (a) shows the dimensions of the cube relative to the crystal axis. (b) shows the plane intersects with x-axes at point a from the origin and is parallel to y- and z-axes [38]. . 15

2.7 Schematic shows the used Bragg Brentano $\theta : 2\theta$ setup, which is applied in the used device. In that case, the sample is moved by a step θ and the detector is moved by a step 2θ to fulfill the reflection law of which the incidence angle should equal the reflection angle. Since it is easier to move the specimen than moving the X-ray tube. Edited from [39] 16

2.8 Typical raw XRD spectrum for an unknown material where the intensity is plotted as a function of 2θ. After measurements this unique set of peaks is compared with the database to identify the material and define the crystal structure information. 17

2.9 Example of the crystallographic information database (PDF-2 card 25-1257) showing the exact peak positions and the relative intensities normalized to the highest peak intensity. The peaks are plotted versus 2θ on the x-axis(bottom) and versus interplanar spacing d on the x-axis(top) 17

2.10 Schematic drawings shows the degrees of freedom used to perform the texture measurements. 19

2.11 Pole figure representation of W_2N thin film for the first two XRD peaks shows the intensity variation of (111) reflex (a) and (200) reflex (b) as a function of (χ, ϕ). The figures shows a strong texture with preferred (111)-orientation as well as a slight inclination from the crystal plane to the substrate plane which could be due to the deposition angle. 19

2.12 Possible products resulting from the interaction between high energy ions and matter, blue dashed lines show the backscattering geometry of Rutherford backscattering spectrometry (RBS) and nuclear reaction analysis (NRA). Other techniques use different products for different measurements. In addition part of the beam could pass through the single crystal substrate. 21

2.13 Schematic illustration of the IBA setup showing the beam-lines for all experiments. . 22

2.14 The back scattering IBMgeometry where θ is the scattering angle [42]. 23

2.15 Schematic drawing of RBS setup showing the main components. The gray dashed line shows the beam path. 25

2.16 (a) The samples mounted on the sample holder. Next to the holder a a *cm*-scale for reference. (b) shows the load lock chamber with the calibration samples on the sample holder mounted on the manipulator. 26

2.17 Typical RBS spectrum of WN_x on *Si* substrate where the number of counts is plotted as a function of the backscattering energy. On the right hand-side the surface peak of tungsten followed by the substrate edge and the nitrogen peak overlapped with the *Si*-signal is on the left hand-side. The data is smoothed for better representation. . . . 27

2.18 Calibration spectrum from the five calibration samples from different materials. Showing that peak position depends on the element, i.e. used for element identification . . 27

2.19 Schematic drawing of the $^{14}N(\alpha, p_0)^{17}O$ reaction resulting in a backscattered proton and oxygen-17, the proton detector is placed at a scattering angle of 135° such reaction happens usually in a narrow resonance which could provide good depth resolution of thin sampls. [45] 29

2.20 Schematic drawing of TDS setup showing the used external oven in light blue as well as the quartz tube connected to the UHV chamber with a valve. The QMS is also connected to the chamber. [46] 30

2.21 Typical QMS raw signals plotted versus the QMS cycle, corresponding to time, and on the right *y*-axis is the temperature (black solid line) ramped up with a fixed rate of 15 k/min. The evolution of some signals is clear like N_2 mass 28 and Ar mass 40. . . 31

2.22 Schematic drawing of electron-material interaction showing all possible products, the relative depth of each interaction and the possible scattering and transmission. Each product of interaction could be measured with a specific detector and provide characteristic information about the material of the sample and the micro-structure. [48] 32

2.23 Schematic drawing of the possible trajectories of a high energy ion-beam with intensity I within a crystalline specimen. The beam might transmit with intensity T forming a contrast image, scatter randomly N without intense spots or get diffracted by the crystal planes of spacing d forming diffraction patterns.[50] 33

2.24 Schematic illustration of the typical diffraction patterns (lower part) as a function of the material crystallinity (upper side), i.e., the grain size and their orientation. (a) shows the typical diffraction pattern of a single crystal cubic lattice with (100) orientation. (b) shows the typical diffraction pattern of few grains with different orientation which somehow can be recognized. (c) shows the typical diffraction rings of a poly crystalline material where the grains are oriented in all possible directions.[50] 34

2.25 Schematic drawing of a diffraction pattern from one crystal showing the crystallographic planes, the diffraction spots and the angle between the spots α. [50] 35

2.26 SEM image of a lamella which was fabricated using FIB showing the C- and W-coatings to preserve the surface during cutting and the supporting Mo-structure. . . . 36

2.27 Schematic drawing of EDX showing the working principle where an electron-beam scans the surface and at each point the interaction leads to the emission of characteristic x-ray which is then collected and detected using a Si(Li) detector. That detector needs to be working at low temperature normally cooled down by liquid nitrogen.[53] 36

2.28 Schematic drawing of XPS setup showing the working principle where the material surface is illuminated with a photon source resulting in an emission of photoelectrons. Such photoelectrons are then focused and guided to an analyzer which separate the electrons based on their kinetic energies. In the lower right side some typical spectrum of pure elements where the electron intensity is plotted versus the electron kinetic energy. [55] 38

2.29 Schematic illustration of the working principle of GDOES, where the material of the sample is sputtered via a glow discharge, ionized and the emitted photons are collected with optical lenses. The collected photons are separated based on their different wavelengths and the intensity of each wavelength is then measured and matched to the elements line radiation. [57] 39

2.30 (a) Typical load-displacement curve where the applied load is plotted versus the tip depth or the displacement from the surface [59]. (b) Image of the pyramidal tip and the indent on the surface after the load was applied [60]. 40

3.1 (a) SEM image of a delaminated WN_x layer, once it was exposed to the atmospheric pressure, due to the residual stress. (b) An image of a simple substrate holder used during the optimization process in order to study the effect of each deposition parameter, while ensuring all the other parameters remain constant, i.e., not even switching off the plasma. It uses a movable shutter to cover all the substrates, after the etching process, during the deposition except for one-sixth. No substrate-rotation was used during the application of this method. 42

3.2 XRD patterns of tungsten nitride W_2N (blue line) compared with the database peak positions(red lines). 44

3.3 XRD patterns of WN_x shows the effect of the chamber total pressure. (a) Only the peaks are shown with axis breaks. (b) A zoom-in to the most intense peak ([111]) shows the peak shift as a function of the chamber total pressure. No monotonic behavior can be seen. 44

3.4 The used method to reduce the uncertainty in the RBS measurements, namely, the current measurements. (a) A typical RBS spectrum measured by 3815 keV $^4He^+$ shows the first W-peak followed by the WN_x peak simulated using SIMNRA. In that case an in-situ current calibration is made. (b) A schematic drawing of the layers system used for that method. 45

3.5 A graph representation shows the measured conversion relation from *sccm* to *Pa* for both Ar (black line) and N_2 (red line). 46

3.6 XRD patterns of different W_2N layers shows the effect of the $Ar : N_2$ relative flow rate (partial pressures). (a) A comparison of four samples with a constant Ar flow rate of 60 *sccm* while the N_2 is set to 10, 15, 20 and 25. (b) a zoom-in to the comparison of the most intense peak ([111]) shows the peak shift as a function of the N_2 flow. . . . 46

3.7 XRD patterns of layers deposited with higher N_2 percentage in the gas mixture. (a) Deposited at $Ar : N_2$ flow rate ratio of 50 : 50 resulted in a transition from W_2N to, most likely, WN, however the peaks intensity are very low. (b) Deposited in pure N_2 atmosphere as a sputtering gas. As only one peak (broad) was observed at $\sim 35.0^\circ$, deposition on W (black line) and on Si (green line) substrates were made to exclude any substrate contribution. 47

3.8 Typical RBS spectra of WN_x layers deposited at different $Ar : N_2$ ratios on graphite substrates. These samples were measured using 7414 keV $^4He^{++}$. Different peaks can be seen from the right hand side: a tungsten peak, a proton peak from $^{14}N(\alpha, p_0)^{17}O$ reaction, an oxygen peak which is relatively big since it has a much higher cross section than nitrogen, the nitrogen peak and finally the carbon substrate. It can be seen that the nitrogen and the tungsten content in the layers varies by varying the nitrogen flow rate from 10% up to 100% 48

3.9 The proton signal for the Nitrogen-NRA measured simultaneously with RBS for the same samples shown in Fig. 3.8. It shows the same trend, i.e., the peak integral which represents the nitrogen amount changes as a function of the nitrogen flow rate. The peak integral is a function of the sample thickness as well, therefore it must be normalized for a correct interpretation. 48

3.10 Typical RBS spectra measured at 3.8 MeV $^4He^+$ of three samples with different stoichiometries. (a) WN_x layer deposited on Si substrate, has a thickness ~ 4.0 μm and is covered with a thin pure-W layer. This layer contains ~ 38.0 $at.\%$ N which is close to W_2N phase. (b) WN_x layer deposited on Si substrate, has a thickness ~ 0.7 μm and is covered with a thin pure-W layer. This layer contains ~ 55.0 $at.\%$ N which is close to WN phase. (c) WN_x layer deposited on W substrate, has a thickness ~ 1.0 μm. This layer contains ~ 67.0 $at.\%$ N which is close to WN_2 phase. 49

3.11 Different layers deposited at the same $Ar : N_2$ gas flow ratio of 15 : 15 $sccm$. All the conditions were kept constant except for the substrate bias was set to different values of $0, 10, 20$ and 50 W of RF power resulting in self biasing voltages of $0,\ 92,\ 176$ and 325 V, respectively. It can be seen that the layer thickness decreases by increasing the bias power. That can be due to a re-sputtering of the deposited-layers by the energetic ions, or a change in the plasma parameters. 50

3.12 SEM images of the surface morphology of three WN_x layers have different stoichiometries as discussed earlier. (a) W_2N, (b) WN and (c) WN_2. 51

3.13 HRTEM images (scale bare of 100 nm) show the micro structure of a W_2N specimen at different focusing points: (a) over focus, (b) just focus and (c) under focus. That can show the porous structure (the black points in Fig. (a) turn white in Fig. (c)). The change can only be seen on the small dot-like spots not on the big scale black areas. . 51

3.14 XRD patterns of a W_2N sample before and after annealing at 500 $^\circ C$ for 10 hrs. (a) Performing annealing at these conditions had a minor effect on the layer. However no big change on the grain size (peak width) or on the residual stress (peak) shift can be seen. (b) a zoom-in to the most intense two peaks shows a slight change on the layer texture (the relative peak heights). 52

3.15 (a) XRD patterns of three identical W_2N samples before and after annealing at 800 $^\circ C$ by the same heat ramp up of 15 K/min for two different holding times. First, for 30 *min* then cooled quickly by turning off the heating (red line). Second, for 10 *hrs* then cooled down slowly by a rate of 1 K/min. The latter led to a transformation from W_2N to pure-W. The slow cooling (longer annealing time) led to a decrease in the peaks intensity, however, no pure-W peaks observed. (b) A Zoom in to the most intense peaks show clearly the peak shifts and the intensity changes. 52

3.16 TEM images show the diffraction patterns of a W_2N sample after annealing (a) compared with before annealing (b). The images are indexed by the reference rings positions (red half-circles) of W_2N and the spots correspond to pure-W are marked (green circles). The effect of annealing can be seen by the discontinuity of the rings to form scattered spots. 53

3.17 Confocal laser microscope (CLM) images show the cracking network of the three different stoichiometries samples (a) W_2N, (b) WN and (c) WN_2. after annealing at 700 $^\circ C$ for 3 *hrs* three times. The image scale is 30 μm and is the same for all images. 54

3.18 EDX spectrum of a W_2N (a) shows the peaks related to W and N. (b) a zoom-in shows an Ar-related peak with a measurable amount. 55

3.19 TDS desorption spectra of a W_2N on a log-scale (a) and on a linear scale (b) and a WN_2 sample on a log-scale (c) and a on a linear- scale (d). The images show a comparison between a W_2N which is deposited in a gas mixture of Ar and N_2 vs. a WN_2 sample which was deposited in a pure N_2 atmosphere. The plots on the log scale show a release of Ar compared with the other which is a sign of gas retention. However, that can not explain where exactly that gas is retained. 56

3.20 GDOES spectra of: (a) WN_2 deposited on W plotted on a log-scale. (b) the same as the latter but on a linear scale. (c) W_2N deposited on *Si* substrate and covered with a thin pure W layer. The main impurities in the layers are identified as well as to the homogeneity of the layers is verified. 57

3.21 EBSD measurements of a W_2N sample after annealing at 800 $^\circ C$ for 10 *hrs*(b) and (d) overlaid on the SEM images (a) and (c). The annealing led to cracking of the layer. Relatively big pure-W grains can be seen only around the cracks. 58

3.22 (a) Typical load-displacement curves resulted from measuring the mechanical properties of a W_2N at varying loads. (b) Image of the measurements indent. 59

3.23 (a) XRD comparison of the three observed stoichiometries shows only the most intense peak. The relative peak shift to the reference values are shown as well as the original spectrum and the smoothed spectrum. (b) RBS spectra (raw data) comparison of the three observed stoichiometries smoothed and normalized to the the identical pure tungsten peak. 60

3.24 SEM image of a FIB cross section of a W_2N layer which has the best obtained crystallinity, however the porous structure (black dots) is dominating the microstructure of the layer. 61

4.1 SEM images show a comparison of the surface morphology of (a) an optimized layer shows a grainy structure observed for the first time. (b) The surface morphology of a common layer. 64

4.2 SEM images show a FIB cross-section of the same samples in Fig. 4.1 (a) an optimized layer, (b) a common layer. 65

4.3 Comparison of XRD patterns showing the most intense peaks (normalized) of an optimized layer (blue line) and a common layer (black line) 65

4.4 Typical RBS spectra measured using 4070 keV $^4He^+$ of the optimized layer coated with a pure tungsten layer. (a) The simulation (black line) is in a very good agreement with the experimental spectrum (red line) (b) a zoom-in shows some wiggling in the spectrum which can be correlated to a minor inhomogeneity of the layer 67

4.5 Nitrogen depth profile of an optimized layer overlaid onto a SEM image of a FIB cross-section image of the sample to show the the correlation between visible microstructure and measured nitrogen content. 68

4.6 Thermal desorption spectra (TDS) of the recorded masses to mainly show the thermal behavior of the nitrogen release (blue line) as a function of the oven temperature (yellow dashed-line). (a) On a linear scale. (b) On a log scale to show the other existing masses with trace amounts. 70

4.7 The N_2- QMS signal as a function of time as shown in Fig. 4.6a. A four-Gaussian-peaks fit is applied to present the possible peak-shapes and position, however, further investigations are needed to comprehend the reason behind such slow decomposition process. 71

4.8 TDS N_2 release signal as a function of temperature for a comparison between an optimized layer (red line) and a common layer (black line). 71

4.9 Two TDS signals of nitrogen release of the optimized correspond to two heating profiles; full desorption heating profile (yellow line) and the other is heating until the first peak is obtained then the temperature was slowly set back to 900 $^{\circ}C$ by a rate of 15 $^{\circ}C/min$ and was held for 30 *min* at 900 $^{\circ}C$, then it was ramped down. The nitrogen signal shows a sudden drop when the temperature was decreased. 72

4.10 SEM images of the surface morphology after heat treatment as a comparison between an optimized and a common layer. (a) an optimized layer heated up to 1050 $^{\circ}C$ with scale 10x smaller to show the overall effect which showed expansion. (b) a common layer annealed at 800 $^{\circ}C$ which showed contraction. 73

4.11 Thermal linear expansion coefficients (a) WN_x and W up to 400 $^{\circ}C$ from [68] the closest stoichiometry to the produced layer is $WN_{0.43}$. (b) A reconstruction of the the first graph with extrapolation up to 1000 $^{\circ}C$ with comparison to the *Si* substrate. The reconstruction was done digitally using then the lines were fitted by polynomial functions then were extrapolated. 74

4.12 Confocal laser microscope image constructed by stitching and merging of multiple images. (a) Intensity image reconstructed from multiple focus levels showing, with high resolution, the damage due to thermal stresses. (b) Height image (elevation image) shows the surface topology in a color map. (c) Line profile as shown in Fig. 4.12b (green line). This figure can show that the damage of the layers was mainly due to thermal expansion of the layer and no volume loss (shrinking) as it has been believed. 75

4.13 Phase diagram of (a) *W-N* system showing the γ phase (W_2N) stability region. (b) The *W-Si* system showing the possible phases which can exist $\sim$ 950 $^{\circ}C$. 76

4.14 TDS comparison of the optimized layer deposited on *Si* and on *C*. The graph shows the N_2 signal as a function of time, as well as, the oven temperature as a function of time. It can be seen that the layer which is deposited on *C* has a sharp release peak in comparison with the release peak from the layer which is deposited on *Si*. 77

4.15 RBS spectra (smoothed) of the optimized layer deposited on *Si* and *C* substrates. Annealing above 900 $^{\circ}C$ showed diffusion of the substrate elements into the film. The layer on *Si* was annealed at 1050 $^{\circ}C$ for 3 *hrs*. the layer on carbon was annealed at 950 $^{\circ}C$ for 40 *hrs*. 78

4.16 High resolution SEM tilted-image (digitally sharpened) of a broken edge to show the micro voids (black dots) appeared on the surface after heating it up to 1050 $^{\circ}C$ then the temperature was slowly set back to 900 $^{\circ}C$ by a rate of 15 $^{\circ}C/min$ and was held for 30 *min* at 900 $^{\circ}C$, then it was ramped down a rate of 15 $^{\circ}C/min$. (b) SEM image (normal view) to get a closer look to the changes on the surface morphology (crack and volume loss). 79

4.17 (a) The residual stress in the optimized layer as a function of the horizontal distance of the substrate measured in two perpendicular directions. (b) The curvature of the substrate as a function of the horizontal distance of both the silicon substrate before deposition (light blue) and with the film after deposition (red line). 80

4.18 RBS spectra (smoothed) of the optimized layer as-deposited, after annealing at 900 $^{\circ}C$ for 50 *hr* and after annealing at 1050 $^{\circ}C$ for 5 *min*. It can be seen that no detectable loss of nitrogen has been recorded. 81

4.19 (a) The effect of annealing at 900 $^{\circ}C$ for 50 *hr* on the micro-structure showed a shift in the peak positions towards the reference value. That means that a big portion of the residual stress has been relieved. (b) a zoom-in to the two main peaks. 82

4.20 Annealing at 900 $^{\circ}C$ for 50 *hr* did not show a noticeable effect on the texture of the optimized layer. (a) as deposited (b) after annealing. 83

4.21 SEM images the optimized layer after two different heat treatments. (a)The optimized layer after heating it up to 1050 $^{\circ}C$ then the temperature was slowly set back to 900 $^{\circ}C$ by a rate of 15 $^{\circ}C/min$ and was held for 30 *min* at 900 $^{\circ}C$, then it was ramped down a rate of 15 $^{\circ}C/min$. This shows much more cracks which can be attributed to the heating ramp. (b) Annealed at 900 $^{\circ}C$ for 50 *hrs* with heating and cooling rate of 1 $^{\circ}C/min$. The scale of this image is two times bigger to show more details. This show minor cracks which can support the idea that the slow ramp can help release the stress without causing a big damage to the layers. 84

5.1 Sketch of the plasma loading device "PlaQ" [76] 86

5.2 the differential cross section of the used nuclear reaction ($D(^3He,p)^4He$) [78] 87

5.3 A comparison between the deuterium amount (the peak integral) in the optimized layer (red line) and the common layer (blue line) measured by the NRA products. (a) The proton signal. (b) the alpha particle signal. 87

5.4 The D_2 depth profile as a comparison between the optimized layer (red line) and the common layer (blue line) up to 180 *nm*. (a) Measured by the proton signal. (b) Deduced from the alpha-particle signal which has better a resolution, however, much less probing depth. 88

5.5 A simulation of the proton signal (red line) resulting from 690 *keV* $^3He^+$ 89

5.6 TDS spectrum showing certain recorded masses of a D_2-containing W_2N layer (loaded) plotted on a log scale as a function of time. The oven temperature (light-gray dashed line) is plotted on the right hand side y-axis. The D_2-related masses are $3, 4, 19$ and 20 *amu*. The blue curve is the nitrogen signal mass 14 *amu*. 90

5.7 Linear plot of Fig.5.6 showing the behavior of D_2-related masses release in comparison with N_2 (blue line). 90

5.8 SEM images showing the changes on the surface morphology due to exposure to D_2-plasma. (a) Before exposure. (b) after exposure. 92

5.9 Other layers deposited with pure N_2 as sputtering gas showed preferential sputtering of N_2 and W enrichment on the surface after plasma exposure. (a) Typical RBS spectra of the WN_x peak (zoomed-in) measured at 800 keV $^3He^+$. (b) SEM image of the layer before deposition, however, it is difficult to recognize the difference after the exposure. 92

A.1 Multiple RBS cross section data for ^4He at angle of $165^\circ \pm 5^\circ$ which show the the uncertainty. 104

A.2 (a) SIMNRA simulations of a WN_x layer on C substrate using 3.8 Mev $^4He^+$ using different cross sections. (b) Zoom-in to the nitrogen peak shows the effect of using different cross sections. 105

A.3 RBS cross section data of N, Si and C 106

A.4 NRA cross section data of the reaction $^{14}N(\alpha, p_0)^{17}O$. 106

B.1 TEM lamellas fabrication process part I 108

B.2 TEM lamellas fabrication process part II 109

List of tables

2.1 The first eigh allowed reflections in the fcc crystal structure and their interplanar spacings to easily interpret W_2N rings, i.e., by comparing the order of appearance with the table order.[50] 34

3.1 XRD diffraction peaks comparison between the measured values and the database. . 43

3.2 Summary of the deposition parameters of the three probable stoichiometries. 50

3.3 A summary of the mechanical properties of WN_x layers with different stoichiometries. 59

4.1 List of the optimized deposition parameters 64

4.2 A summary of the calculated densities of the possible WN_x phases compared with calculations of known materials to estimate the error between the theoretical and the estimated experimental values 66

4.3 A summary of the calculated porosity using the theoretical density values showing the effect of the substrate temperature during the deposition to reduce the layers porosity 69

5.1 A summary of the D_2 amount calculated from the NRA proton and alpha peaks integrals 89

5.2 Summary of D_2 amounts in the measured masses as well as an estimation in the D_2-related molecules (accurate calibration not possible), as well as, the total amount. 91

Chapter 1

Introduction

Finding a new energy source is today's major challenge. The world is desperately looking for a clean, sustainable and affordable energy source. In order to be able to cope with the tremendous economic and population growth, in addition to save the environment that we must live in at the same time, we have to explore new possibilities, learn from mother nature, and lower our fossil-fuel consumption, not just to lower the CO_2 emission, but also to be prepared to the future where we run out of fossile fuel [1]. Fusion energy is not a new source of energy, but it is one of the oldest form of energy in our universe. It is the main source in the stars and that is how the sun, our secret of life, is producing the energy. It has always been a dream to harness such inexhaustible energy on our planet. Producing fusion energy now seems achievable more than ever before, where scientists can do that by heating light gases to very high temperatures (plasma) until they fuse together while confining them in a magnetic field [2].

In this work, an investigation of the interaction between nitrogen (used to cool down the plasma before it hits the wall) and tungsten (the current candidate for the first wall that faces the plasma) will be carried out. This chapter is focusing on the basic concepts of fusion energy and fusion reactor, the nature of the interaction between the hot plasma and the wall, the possible interaction between tungsten (W) and nitrogen (N_2) and finally the possible products of such interactions.

1.1 Fusion Energy and Fusion Reactor

This section discusses the basic concepts of fusion; the conditions where fusion can be achieved, the theoretical basis and the experimental approach.

1.1.1 Fusion

The most famous formula of Einstein ($E = mc^2$) explains how a tremendous amount of energy can be produced by the loss of a tiny fraction of mass during a nuclear reaction, that mass loss is converted into energy following Eq.1.1 where c is the speed of light [3]. Indeed that friction is small, but the number of atoms is in the order of 10^{21} atoms per cubic meter which add up such tiny fractions into huge amounts.

$$E = \Delta mc^2 \tag{1.1}$$

In fission, large atoms are split into smaller nuclei [4] resulting in a difference in the nuclear masses between the original nuclei and the sum of their fission products. In contrast, fusion is achieved by fusing light elements together resulting also in mass difference. The main condition for that to happen, is that the nuclei should have enough energy to break the Coulomb barrier between similar charges [5]. Of course very light elements are the easiest to break that barrier. Another factor to choose the optimum elements for such reaction, is the cross section, which translates to the probability of a certain reaction to happen [6].

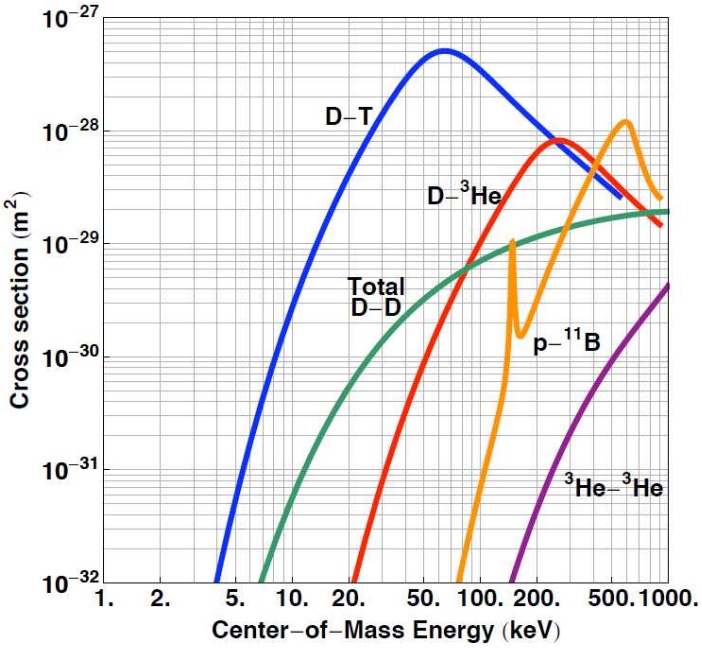

Fig. 1.1 A cross section comparison between all possible fusion fuel candidates as a function of energy in *keV* units showing that $D-T$ reaction (blue line) has the highest probability at the lowest energy [7].

Fig. 1.1 shows the cross section of some fusion candidates as a function of energy. As shown in the figure, the most probable reaction is between deuterium (D) and tritium (T) (eq. 1.2 below) where both are hydrogen isotopes. The $D-T$ has the lowest energy threshold and the highest cross section. The abundance of such fuel is very high, where deuterium exists in the sea water with amounts enough

for millions of years [8]. Tritium doesn't exist naturally. However, it can be produced from the abundant lithium with amounts enough for thousands of years [5].

Explicitly, the envisaged reaction is

$$D + T \longrightarrow He^4 + n + 17.6\,MeV \tag{1.2}$$

where the energy resulting from the mass defect is split among the products inversely proportion to their mass.

1.1.2 Tokamak

Toakmak is one of the most promising devices to produce fusion energy. It uses a donut-shaped magnetic cage to confine the plasma as shown in Fig. 1.2. The idea was proposed by two Soviet physicists Andrei Sakharov and Igor Tamm in 1950s. Such device can contain the plasma while heating it up to reach enough temperatures qualifying it to perform thermonuclear fusion. That technique uses a combination of magnetic fields in order to shape the plasma to a special configuration optimized to extract the exhaust and the excess heat from the plasma and keep the reaction sustainable [9].

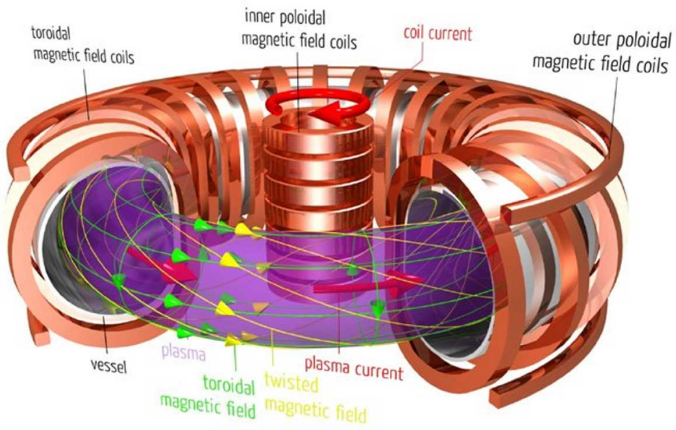

Fig. 1.2 Detailed illustration of a tokamak showing the magnetic field coil (copper-color) and the plasma in the vessel (violet color) as well as the direction of the plasma current and the magnetic field lines (yellow lines)[10].

1.2 Plasma Facing Materials and Interaction

The first wall of the vessel which is containing the plasma is exposed to very extreme conditions where it faces huge amounts of heat and energetic particles specially at a region called the divertor as shown in Figure 1.3a. The divertor region should survive heat fluxes comparable to those on the surface of

the sun. When that is put in numbers, the heat flux in a common reactor will be $\sim 80\ MW/m^2$, even though the material limit is $\sim 10-20\ MW/m^2$, compare to the sun surface $\sim 240\ MW/m^2$ and to the rocket nozzles $\sim 1-10\ MW/m^2$ [11].

By searching in the periodic table amongst all the elements, the most suitable element for that purpose is tungsten due to it is high melting point (the highest among elements), low sputtering yield and high chemical stability. Such element is commonly used in such extreme conditions, but to optimize it for such new environment, many studies should be performed to understand the full behavior [12].

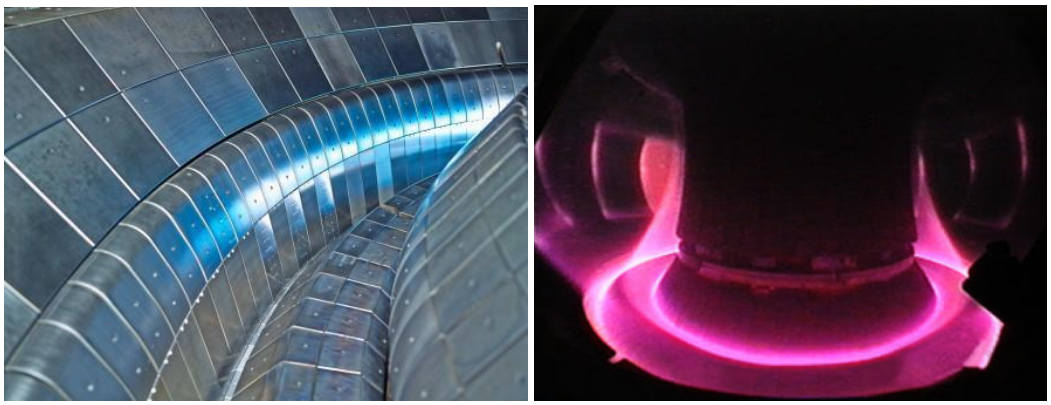

(a) **(b)**

Fig. 1.3 (a) The structure of the tungsten divertor in ASDEX upgrade tokamak [13]. (b) Plasma discharge in ASDEX upgrade showing the interaction between plasma and the wall (magenta color) [14].

One of the strategies applied to tame the high local heat fluxes is to cool down the incoming particles before they hit the wall. That process is called gas seeding, where a high radiative gas species is puffed in the divertor region to extract a large part of the heat and distribute it over larger wall areas via radiation, Fig. 1.3b, instead of being focused on such very narrow area called the strike line. In that sense one of the chosen gases for radiative cooling is nitrogen which is used in ASDEX Upgrade [15].

1.2.1 Nitrogen Interaction with Tungsten

The interaction between the high-energy ions and tungsten can lead to severe damage to the metal tiles, which can reduce the thermal conductivity which in turn leads to inefficient heat extraction, cracks or even melting of the surface. Furthermore, some chemical interactions can happen leading to formation of other materials. One of these interactions can be sputtering. In the sputtering process, the impinging ions can knock out some atoms from the metal surface via momentum transfer. In such

case the sputtered atoms can redeposit again somewhere on the surface forming layers. Those layers can be as the original element or can react with the ions forming molecules [16].

1.3 Tungsten Nitride in the Lab

Tungsten-nitride WN_x has gained much attention through the past few decades, due to its unique properties, like the high chemical stability (inertness) and the excellent resistance to metal diffusion at high temperatures. Applications are found in the field of semiconductor industry [17, 18, 19]. Such properties made the focus on producing such layers in the lab with different methods, in order to produce optimum layers for different applications which are used under different conditions. In the current work the fabrication with DC and RF magnetron sputtering was performed, but other research with several methods has been reported, e.g., ion implantation [20], reactive laser ablation[21], cathodic arc [22] and chemical vapor deposition CVD [23, 18]. Wide range of properties was investigated in detail by many researchers (based on the kind of application), the electrical properties for electronics and the mechanical properties [24] for wear and corrosion and the thermal properties [25] for high temperature applications etc.

The focus of thesis is to fabricate such layers, with the current means, to prepare crystalline phases survive at relatively high temperatures compared with the amorphous layers. Further goals are to understand the micro-structure of those layers and to get a better understanding of the hydrogen-isotopes possible retention-resistance and the pros and cons of the application of tungsten nitride layers (thermal stability and the retention.

Tungsten is one of the thermally most stable materials, it has a very high melting point and unique chemical stability [26]. Consequently, fabrication of chemical compounds is relatively difficult [27], especially, when it comes to nitrides, where nitrides are well-know for their extremely high energy of formation [28]. Common precursors are not applicable. One of the commonly used techniques is magnetron sputtering [29]. The advantage of that technique is the ability to produce non-equilibrium phases. However, the thickness is limited to few micrometers.

Several tungsten nitride phases have been reported, each phase required special conditions and fabrication method. Some phases are reproducible, some are known to be stable, however, very little is known about them. In H. A. Wriedt's work [30] the author reported many possible phases of the W-N system, among all these phases, three stable phases can be taken into account as shown in the table represented in Fig. 1.4.

Phase	at% N	Structure	Type	a [nm]	c [nm]
Stable phases					
γ	33…50	cub	NaCl	0.412…0.414	
δ	≈ 50	hex	WC	0.2893	0.2826
δ_R^V	≈ 67	hex	δ_R^V	0.289	1.640
Other phases					
δ_H^{II}	≈ 33	hex	δ_H^{II}	0.289	0.2285
δ_H^I	≈ 43…47	hex	δ_H^I	0.2885	1.546…1.530
δ_H^I (superlattice)	≈ 43	hex		0.2885	3.092
δ_R^{VI}	≈ 46	hex	δ_R^{VI}	0.289	2.335
δ_H^{IV} ($WN_{0.91}$)	≈ 48	hex	δ_H^{IV}	0.289	1.080
γ	≈ 50	tetr		0.5786	0.6048
γ' (W_3N_4)	57	cub		0.4130	
W_2N_3	60				
Intermed. I	≈ 61	hex			
Intermed. II	≈ 61	hex			
δ_H^{III}	≈ 61	hex	δ_H^{III}	0.287	1.100
δ_H^{IV} ($WN_{1.67}$)	≈ 62.5	hex	δ_H^{IV}	0.289	1.08

Fig. 1.4 Review of some the reported stable and intermediate phases of tungsten nitride with nitrogen atomic concentration and crystal structure information. [31]

W_2N **or the so-called β** Is the most common phase produced by sputtering and was reported in almost all *WN*-literature, e.g., [17, 18, 19, 20, 23].

WN **or the so-called δ** Some researchers reported the phase transition from W_2N to *WN* by the increasing the nitrogen partial pressure during sputter deposition[22, 24].

WN_2 **the so-called δ_R^V** Has not been found to be reported by magnetron sputtering deposition, however, the nitrogen content in some fabricated layers made it necessary to take it into account.

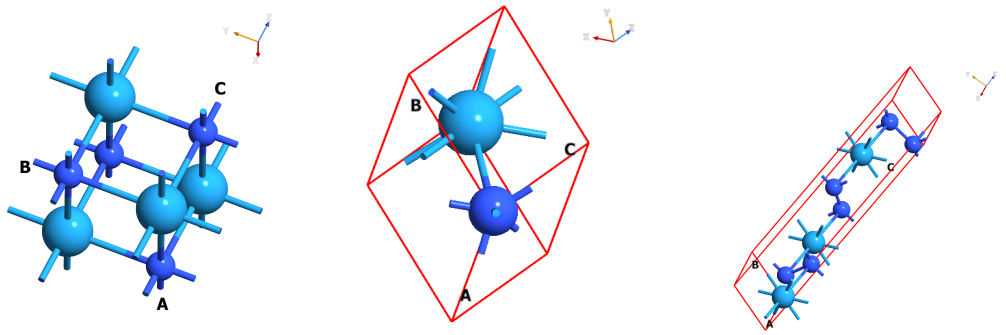

(a) (b) (c)

Fig. 1.5 Illustrations with nitrogen being the small blue spheres, tungsten the big lightblue spheres and red lines are the borders of the unit cells. (a) The cubic lattice structure of W_2N. (b) The unit cell of the hexagonal lattice of WN. (c) The unit cell of the rombohedral lattice of WN_2

It is necessary to comprehend the $W-N$ system, and the possible attainable phases under the available conditions. Only the three stable phases will be considered in this work for comparison. To facilitate visualizing those phases, Fig. 1.5 shows the lattice structure for W_2N, WN and WN_2.

Phase	Composition, at.% N	Lattice parameters, nm	
		a	*c*
Stable Phases			
(W)	0	0.31651	...
β	40 to 50(?)	0.412 to 0.414	...
δ	50	0.2893	0.2826
$\delta_R{}^V$	67	0.289	1.640
Other Phases			
$\delta_{II}{}^{II}$	33.3	0.289	2.285
$\delta_{II}{}^{I}$	~43 to ~47	0.2885	1.546 to 1.530
$\delta_{II}{}^{I}$ Superlattice	~43(?)	0.2885	3.092
$\delta_R{}^{VI}$	~46	0.289	2.335
$\delta_{II}{}^{IV}(WN_{0.91})$	~48	0.289	1.080
γ	~50	0.5786	0.6048
γ'-W_3N_4	57	0.4130	...
W_2N_3	~60	...	...
Intermediate I	~61	...	...
Intermediate II	~61	...	...
$\delta_{II}{}^{III}$	~61	0.287	1.100
$\delta_{II}{}^{IV}(WN_{1.67})$	~62.5	0.289	1.08

Fig. 1.6 Review of the lattice parameters of the reported stable and intermediate tungsten nitride phases at room temperature in *nm* units [30].

1.4 Thesis Goals and Outline

The focus of this work is to fabricate tungsten-nitride layers and to quantify the nitrogen amount in those layers. In addition, study the properties of those layers as a function of the nitrogen content and get a better understanding of the deposition parameters effects on the properties of the layers, consequently, find the optimum fabrication conditions for robust layers which are reproducible. Furthermore, try to simulate similar conditions of the produced layers in a fusion reactor to be able to study them. So in conclusion, there will be two main directions of this thesis; to produce similar layers, as those in a fusion device, but thick enough to be analyzed. Last but not least, to fabricate robust layers to be, later on, tested against the promising properties as a diffusion barrier for hydrogen isotopes [32].

In chapter 2 an explanation of the experimental techniques as well as their theoretical background will be discussed. Chapter 3 will discuss the optimization process and the resulting WN_x phases. Chapter 4 will contain the experimental results and a discussion of the novel properties of the optimized W_2N layers. Besides an explanation of the nitrogen release behavior from the layers at elevated temperatures. Chapter 5 will present the deuterium retention in the optimized WN_x layers in comparison with the common layers. Finally, chapter 6 will show a short summary of the results.

Chapter 2

Experimental Methods

In this chapter all the experimental set-ups, the sample preparation process and the sources of errors in the measurements will be discussed. To prepare and characterize very thin layers, high accuracy is needed. Furthermore, contamination must be utterly minimized, high purity working gases and materials should be chosen, sample handling and storage requires attention and care. In addition, precision while performing the measurements is extremely important to minimize the systematic errors and to assure reliable data.

2.1 Sample Preparation

Tungsten, carbon and silicon substrates were used for the thin films depositions. Each substrate needed a special treatment to be ready. Since *Si*-substrates are very common and easy to handle, $Si(100)$ wafers were mainly used as they are clean, flat and relatively low in cost. $10 \times 10\ mm^2$ *Si* samples where cut and labeled using a laser cutting machine. In case of *W* and *C*, mechanical polishing was applied prior to the cleaning process to obtain surfaces with $\sim nm$ roughness. After cutting and polishing, the samples were cleaned and soaked in acetone in an ultrasonic bath for 10 minutes then soaked ten more minutes in isopropanol and then dried slowly with clean air or nitrogen.

2.1.1 Magnetron Sputtering

Sputtering deposition has become a common method to fabricate thin films. It is a physical vapor deposition process (PVD) where atoms are ejected from a bulk material and condensed on another surface. In such process, a plasma is ignited via a glow discharge between the cathode (which is the material to be sputtered and called the target) and an anode. Ions from the plasma are accelerated towards the target where they impinge with energies typically in the several 100 *eV* range. Via momentum transfer between the plasma ions and the target atoms, the latter can aquire enough energy

to escape from the surface. These sputtered target atoms move randomly and stick to the chamber surface. Thus, the chamber is designed to maximize the deposition on the substrate holder area. The sputtering efficiency (sputtering yield) depends typically on the ion density in the plasma, the atomic masses of the ions and the target, the ions energy, the power density on the target and the incidence angle of the ions on the target etc. Therefore, a magnetic field is added around the target to confine and shape the plasma around it to maximize the sputtering yield that is why it is called magnetron sputtering. Fig.2.1 shows an illustration of the sputtering process around the target and the magnetic filed lines [29].

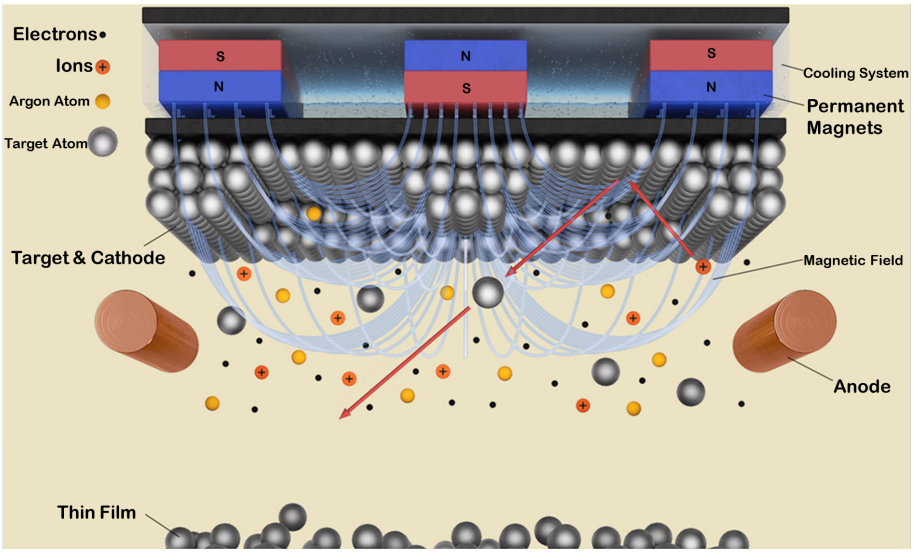

Fig. 2.1 A schematic drawing of magnetron sputtering, showing the working principle of the target and the magnetic field lines of the permanent magnets. Edited from [33]

Furthermore, the so-called reactive sputtering combines the physical deposition with a chemical deposition, where a reactive gas is added to the inert working gas. Consequentially, a chemical reaction happens with the sputtered atoms on the substrate. Such deposition uses oxygen or nitrogen as a reactive gas to deposit compounds such as oxides and nitrides and the chemical composition depends on the gas flow. Since it is the aim of the work to produce WN_x layers with good quality i.e. with the right stoichiometry, good crystallinity, low amount of defects, low residual stress and good mechanical properties, the deposition conditions such as total pressure, nitrogen partial pressure, substrate temperature, DC or RF power and the distance and angle of the target and rotation speed of the sample holder have to be optimized. Furthermore, residual oxygen and water vapor have to be minimized to produce layers with low impurity level. The optimization of the deposition conditions will be discussed in detail in chapter 3.

Fig.2.2 shows Thorton's zone model [34] explaining the general micro-structure of pure, sputter-deposited layers as a function of the substrate temperature, where T/T_M is the ratio between the

substrate temperature and the melting point of the film material, and the total pressure in the chamber. Among the four zones indicated in the figure, the T-zone (transitional zone between zone-1 and zone-2) is the most favorable micro-structure due to it is high density. That is because the grains are packed, the layer has low porosity and has a smooth surface. The idea is that the kinetic energy of the atoms arriving at the substrate surface influences the surface mobility. When the atoms have too high energy they bombard the surface and damage it. In contrast, if they do not have sufficient energy, they stick with poor order creating many voids. By projecting the idea of Thorton's zone model onto such compound material like WN_x, the total gas pressure in the chamber during the deposition plays a big role into defining the the micro-structure of the produced layers layers. Therefore the pressure needs to be optimized to produce dense layers with good micro structure.

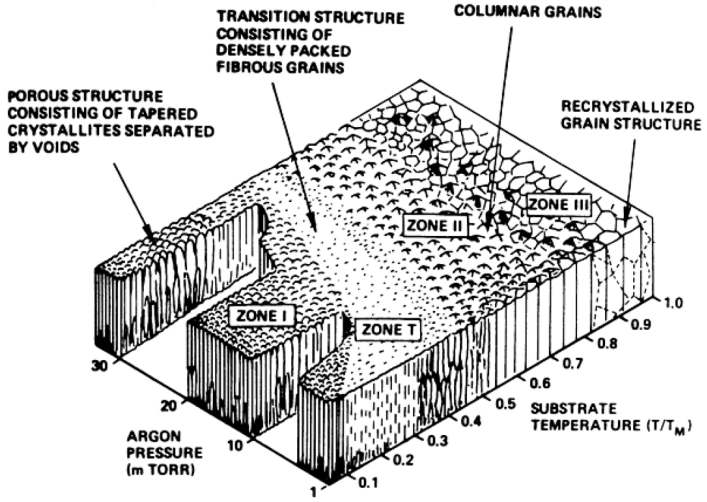

Fig. 2.2 Thorton's zone model as an example for the effect of the deposition conditions on the micro-structure of the deposited layers of pure elements. The typical micro-structures of deposited layers are the most favorable in the so-called T-zone. [34]

The used device is a Denton Vacuum Discovery®-18 Deposition System. It is a multi-cathode device and provides a wide range of control for the deposition parameters. Fig. 2.3 shows the device deposition chamber. It consists of a high vacuum chamber connected to a turbomolecular pump backed with a roughing bump and a cold trap filled with liquid nitrogen to reduce the background water vapor pressure. Furthermore, the device is equipped with two cathodes which can be operated with RF or DC power. The gas flow is controlled with two gas-flow controllers for argon up to 100 *sccm* (standard cubic centimeters per minute) and for nitrogen up to 50 *sccm*. In addition, a substrate heater for temperatures up to $700°C$ and PID (proportional-integral-derivative controller) temperature control with accuracy $\pm 2°$ at $700°C$ and substrate RF bias were used. The substrate holder can be rotated to get a homogeneous deposition. The rotation speed can be controlled in the range $0-30\ rpm$.

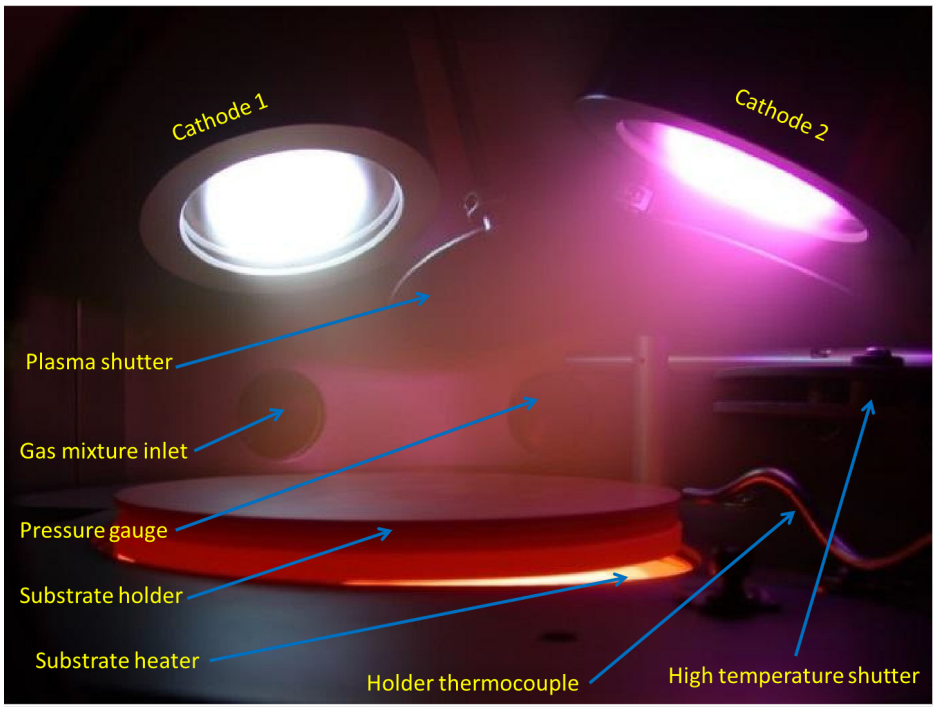

Fig. 2.3 Real picture of the Denton device deposition chamber. The image shows a plasma ignited on both cathodes (for mixed-metals layers deposition) and the main components are indicated.

After the substrates were cleaned as mentioned in Sec. 2.1, they were inserted in the chamber and placed on the substrate holder. In order to guarantee that the produced samples are identical, it is important to provide the same conditions for all samples in the same run. Since the holder rotation is used to produce homogeneous layers, the substrates were placed forming a circle around the center of the holder, and the rotation speed is adjusted to be 10 *rpm*. The chamber was left to pump down during the night to pressures $\sim 5 \times 10^{-5}$ *Pa*. Before starting the deposition, the substrates were sputter cleaned for 5 *mins* by applying 100 *W* RF power to the substrate holder with 30 *sccm Ar* resulting in a voltage 350 *V* and total pressure of ~ 1.0 *Pa*. Afterwards, RF or DC power in the range $100 - 600$ *W* was applied to the sputter target while the shutter in front of the target was closed to presputter the target for another 5 *min* to remove any oxide layers or impurities. Finally the shutter was opened and the deposition starts for the required time to produce the planned thickness. Fig 2.4 shows experimental results for the thickness calibration carried out in one hour of deposition, i.e. the deposition rate at different DC powers in the range $100 - 600$ *W* for gas mixtures 15 : 15 *sccm Ar* and N_2 and pure nitrogen atmosphere by applying a flow of 30 *sccm*. The thickness measurement was performed using Bruker's Dektak®stylus profilometer. The thickness was measured by masking a part of the substrate during the deposition forming a step, consequently, the layer thickness is obtained by measuring the step height between the clean substrate and the deposited layer.

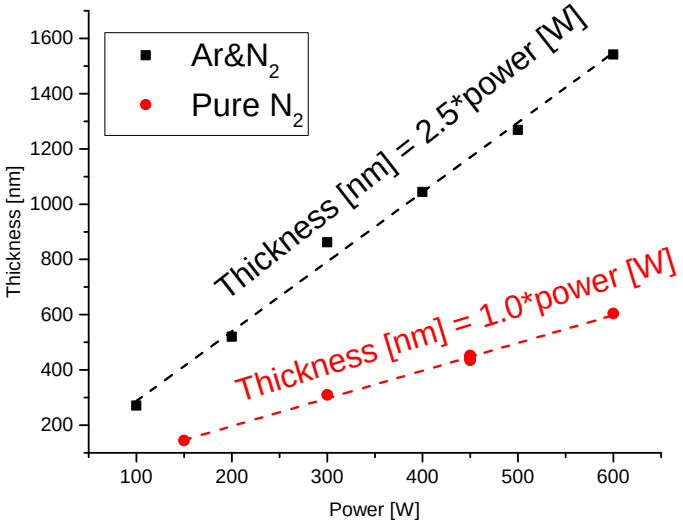

Fig. 2.4 Calibration curve based on experimental results to estimate the thickness of the deposited layers as a function of the applied power. All the depositions were carried out for 60 *min*. The total chamber pressure was ~ 1 *Pa*. The black line represents depositions carried out in a gas mixtures of 50% *Ar* and 50% N_2. The red line represents depositions carried out in pure nitrogen atmosphere. The equations on the lines are empirical equations to roughly estimate the layer thickness in 60 *min* as a function of power.

2.2 Characterization Techniques and Set-ups

In order to reliably identify the chemical composition, nitrogen content, stoichiometry and probable phase, multiple techniques where applied so that a high degree of certainty is achieved. In this work wide variety of methods were applied to characterize the properties and also the micro-structure of the produced layers, for better understanding of such layers. Following are short explanations of the used techniques and devices.

2.2.1 X-ray Diffraction (XRD)

X-Ray Diffraction is a very important technique for determining the crystal structure and the lattice constant [35] of crystalline materials. It is very robust, requires a relatively simple set-up and data interpretation is almost straightforward. It began when Max von Laue, in 1912, found out that the crystalline materials could act as a diffraction grating for such very short wavelength of the X-ray. That kind of diffraction grating is 3D, where a constructive interference of the monochromatic X-ray results in well defined bright spots related to the d-spacing between the crystal planes as a function of the incidence angle as sketched in Fig. 2.5. Such condition is represented by Bragg's law (eq. 2.1) [36].

$$n\lambda = 2d\sin(\theta) \tag{2.1}$$

where n is an integer number, λ is the wavelength, d is the inter-planar spacing and θ is the diffraction angle.

Solids are categorized with respect to their basic structure of atoms and there are two main categories either amorphous, where the the atoms have random positions, or crystalline where the atoms possess a repetitive pattern. Most of the metallic materials have some degree of crystallinity and the basic building block is called the unit cell. When the atoms sitting in fixed crystal planes are exposed to X-ray, a constructive interference will occur, when Bragg's condition is fulfilled, resulting in a high intensity reflection as shown in Fig.2.5.

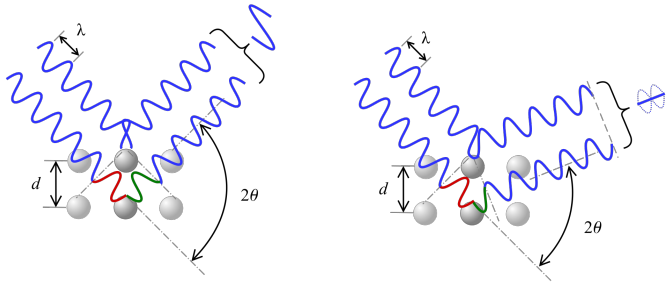

Fig. 2.5 Schematic view of the reflection of the waves form the crystallographic planes showing that the reflected waves will always have destructive interference except when the Bragg's condition is satisfied. At a certain 2θ angle a bright constructive interference occurs.[37]

The crystal planes are defined by what is called the Miller indices, which represent the intersection between the crystal plane and the main crystallographic axes and have the notation (hkl). To simply get the idea, let's use an example assuming a cubic lattice (same as $W-2N$) with dimensions $a\times a\times a$ as shown in Fig. 2.6a. To get the Miller indices of the shaded plane in Fig. 2.6a, we firstly identify the interceptions so we have (a,∞,∞), where ∞ means that the plane is parallel to the axis. Secondly, the intercepts are represented in the fractional coordinates by dividing the intercepts points by the respective dimensions so we get $(a/a,\infty/a,\infty/a)$ which is $(1,\infty,\infty)$. Lastly, Miller indices finally assigned by taking the reciprocals of the fractional intercepts, noting that the reciprocal of ∞ is 0, the Miller indices of that plane is (100).

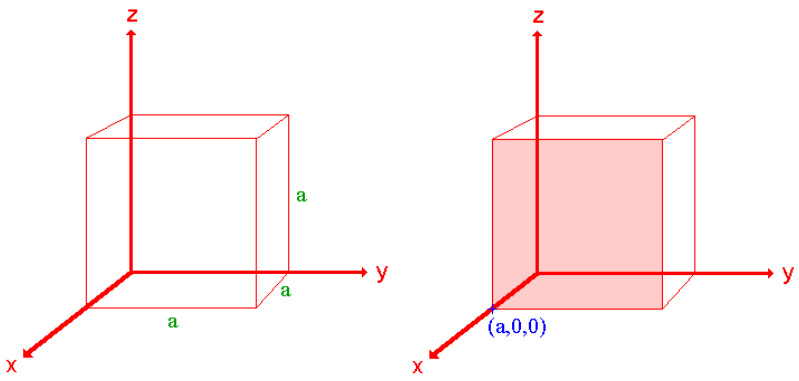

Fig. 2.6 Simple example of calculating the Miller indices and defining the lattice planes. (a) shows the dimensions of the cube relative to the crystal axis. (b) shows the plane intersects with *x*-axes at point a from the origin and is parallel to *y*- and *z*-axes [38].

Fig. 2.7 shows the XRD setup with the used geometry. The device consists of a X-ray tube where X-ray is generated using a cathode ray tube with copper cathode, and is filtered to ensure a single wave length, known as the characteristic X-ray. The sample is mounted on a high-precision sample holder positioned with μm accuracy to be exactly in the beam-focus. Further optics is used to filter the diffracted beam and guide it to the detector where the intensity I is recorded as a function of θ.

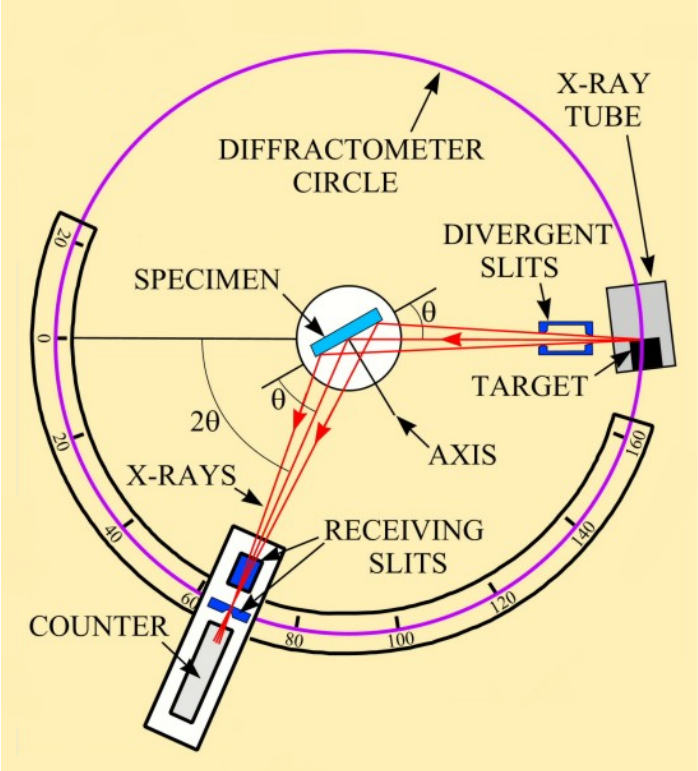

Fig. 2.7 Schematic shows the used Bragg Brentano $\theta : 2\theta$ setup, which is applied in the used device. In that case, the sample is moved by a step θ and the detector is moved by a step 2θ to fulfill the reflection law of which the incidence angle should equal the reflection angle. Since it is easier to move the specimen than moving the X-ray tube. Edited from [39]

After having the suitable layers, the samples are glued on a sample holder made of amorphous acrylic. The sample is positioned using a micrometer to the focus point by adjusting the computer-controlled stage with micrometer accuracy and recording the exact x, y and z values. Afterwards a software recipe is prepared where all experiment conditions are specified. For this work, the possible 2θ scan range is in $10° : 150°$ (shorter range is possible) with step $0.01°$ (depending on the needed resolution) and counting time of $10 - 30$ s to assure good statistics. A typical resulting scan representing intensity as a function of 2θ is shown in Fig. 2.8. The software uses a database from the International Centre for Diffraction Data (ICDD) and matches the characteristic set of peaks with all possible candidates in order to identify the phase.

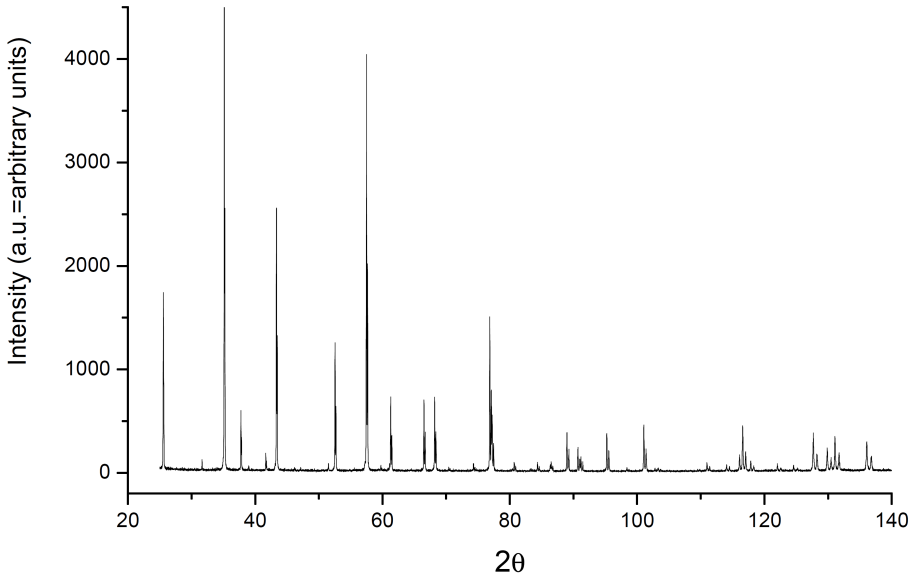

Fig. 2.8 Typical raw XRD spectrum for an unknown material where the intensity is plotted as a function of 2θ. After measurements this unique set of peaks is compared with the database to identify the material and define the crystal structure information.

Fig. 2.9 shows the database values for W_2N (PDF-2 card 25-1257) as an example showing the peak positions with the relative intensities corresponding to each crystallographic plane. After matching the peak positions and the corresponding crystallographic plane (characterized by it is (hkl) index), Bragg's law (eq.2.1) is used to calculate the interplanar spacing d for each peak position 2θ. By solving the standard formula of the corresponding crystal system as shown in eq. 2.2 the lattice parameter(s) is obtained. Since the three stable phases of the W-N system have cubic, hexagonal and rhombohedral lattice as shown in sec. 1.3, it is important to mention how to calculate their lattice parameters.

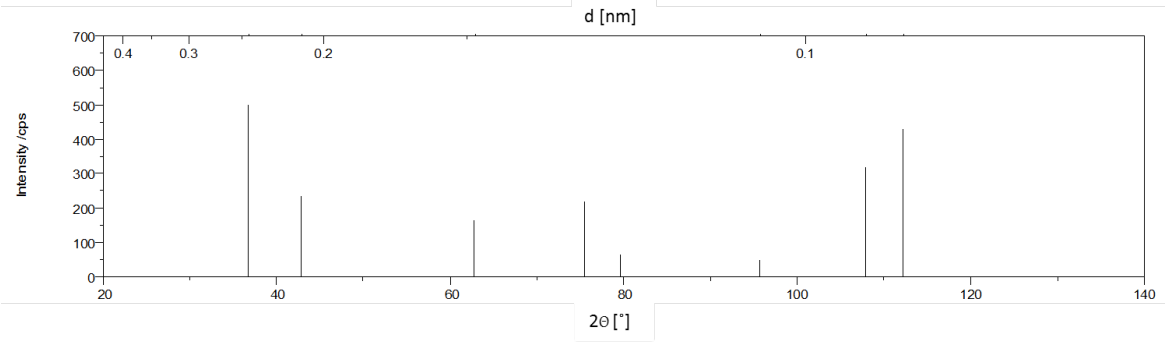

Fig. 2.9 Example of the crystallographic information database (PDF-2 card 25-1257) showing the exact peak positions and the relative intensities normalized to the highest peak intensity. The peaks are plotted versus 2θ on the x-axis(bottom) and versus interplanar spacing d on the x-axis(top)

$$\text{Cubic:} \qquad \frac{1}{d^2} = \frac{h^2+k^2+l^2}{a^2} \tag{2.2a}$$

$$\text{Hexagonal:} \qquad \frac{1}{d^2} = \frac{4}{3}\left(\frac{h^2+hk+k^2}{a^2}\right) + \frac{l^2}{c^2} \tag{2.2b}$$

$$\text{Rhombohedral:} \qquad \frac{1}{d^2} = \frac{(h^2+k^2+l^2)\sin^2\alpha + 2(hk+kl+hl)\cos^2\alpha - \cos\alpha}{a^2(1-3\cos^2\alpha+2\cos^3\alpha)} \tag{2.2c}$$

In the experimental results, the peaks might have a slightly different position or the relative intensities are not matching the database, hence, it is important to understand the possible reasons causing that. During the layers fabrication, some residual stress σ may arise in the materials which could be due to thermal, chemical or mechanical effects. Residual stress is defined by the stress which exists in the material without applying any force on it, and its unit is Mega Pascal (MPa). Residual stress has two types, either compressive i.e. the material tends to shrink and it has a negative sign ($\sigma < 0$) , or tensile where the material tends to expand and have a positive sign ($\sigma > 0$). Such residual stress affects the distance between the crystallographic planes d causing the peak position to be slightly shifted from it is proper position. So, d decreases in case of compression, i.e., the corresponding peak shifts to the right. On the other hand, d increases under tension resulting in a shift to the left.

Furthermore, the relative intensities are a key factor to successfully characterize the material with XRD. Under certain conditions the relative intensities are not as expected. Materials usually consist of different grains (polycrystalline) normally with random crystallographic orientations, however, sometimes materials tend to have preferred orientations and in that case the materials are said to have a texture. The degree of texture can vary from weak to strong. The micro-structure defines the texture and in turn determines the material properties. In case of thin films, one common texture is called fiber texture where a specific lattice plane is parallel to the substrate plane.

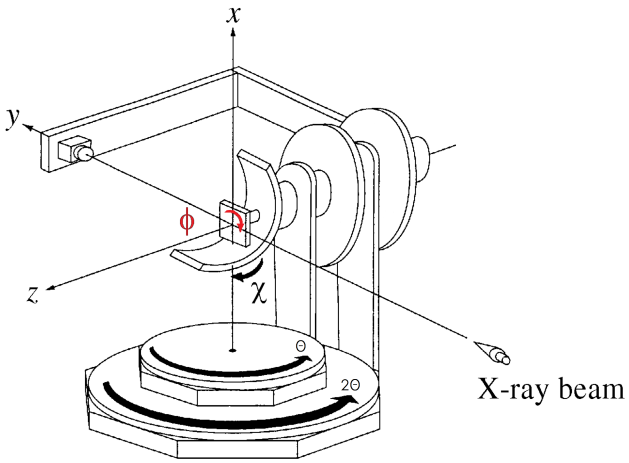

Fig. 2.10 Schematic drawings shows the degrees of freedom used to perform the texture measurements.

Texture measurements are carried out, through this work, to correctly interpret the XRD results and get the crystallographic information. Such measurements are performed for each peak at fixed 2θ (the degrees of freedom are shown in Fig. 2.10) and tilting the sample by a certain χ angle step in the range from $0-70^\circ$ and at each step a complete in ϕ angle in the range $0-360^\circ$ while at each point the intensity is recorded producing a map in the shape of a hemisphere. Afterwards those data are plotted in a 2D pole figure with a color map as shown in Fig. 2.11. From such figure the intensity distribution represents the orientation probability as a function of (χ,ϕ) angles relative to the substrate plane i.e. the preferential orientation if there is one and in that example, it is clear that the sample has a favorable (111)-orientation with a slight offset from the center.

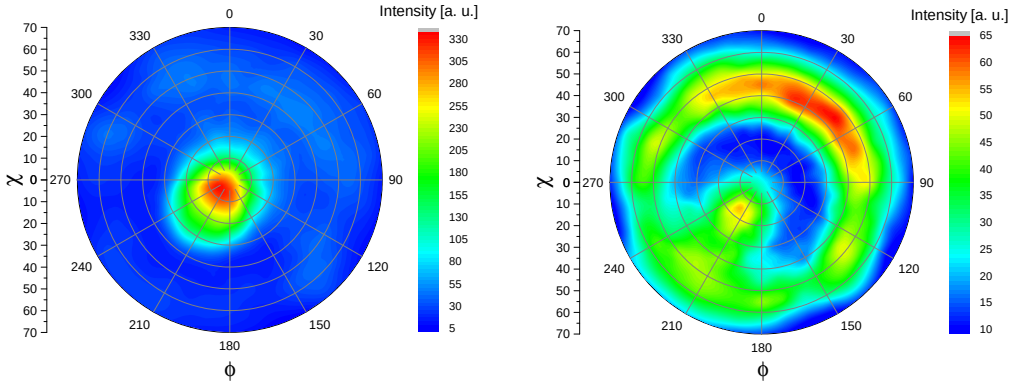

(a) (111) **(b)** (200)

Fig. 2.11 Pole figure representation of W_2N thin film for the first two XRD peaks shows the intensity variation of (111) reflex (a) and (200) reflex (b) as a function of (χ,ϕ). The figures shows a strong texture with preferred (111)-orientation as well as a slight inclination from the crystal plane to the substrate plane which could be due to the deposition angle.

All in all, XRD is a powerful technique to reliably identify the crystal structure, yet, a closer look to the sources of error is important. XRD can measure the lattice parameter with accuracy of 0.0001 *nm*, however, to attain such a accuracy sources of errors should be eliminated or at least minimized[40]. Examples of such errors are are following:

Sample positioning The sample should be flat and mounted precisely parallel to the surface of the sample holder with error less than 100 μm.

The 2θ offset it is crucial to calibrate the diffractometer in order to have the correct zero and provide the correct Bragg angle.

Sample displacement it is is the biggest source of error in XRD measurements, where it is the displacement in the sample during the measurements. The error in the interplanar distance Δd is estimated by

$$\frac{\Delta d}{d} = \frac{-D\cos^2\theta}{R\sin\theta} \tag{2.3}$$

where D is the displacement and R is the diffractometer radius.

Absorption When the X-ray gets absorbed in the material while measuring thick samples, results in what is called the transparency error

$$\frac{\Delta d}{d} = -\frac{1}{2\mu R}\cos^2\theta \tag{2.4}$$

where μ is the the absorption coefficient and R is the diffractometer radius.

In short, the high degree of precision was not much of interest as all the measured samples were compared with existing phases in the database. Moreover, the device was calibrated with silicon-powder reference sample every now and then.

2.2.2 Ion Beam Analysis (IBA)

When a depth profile of elements concentrations is needed with a few nanometres resolution (or even monolayers resolution with special equipment), ion beam analysis (IBA) is the suitable tool [41]. It utilizes high energy ions (MeV range) to probe the material surfaces or thin layers in the range of few tens nanometres up to few microns. The measurements in most cases are quantitative. Fig. 2.12 illustrates some possible interactions between energetic ions and the material.

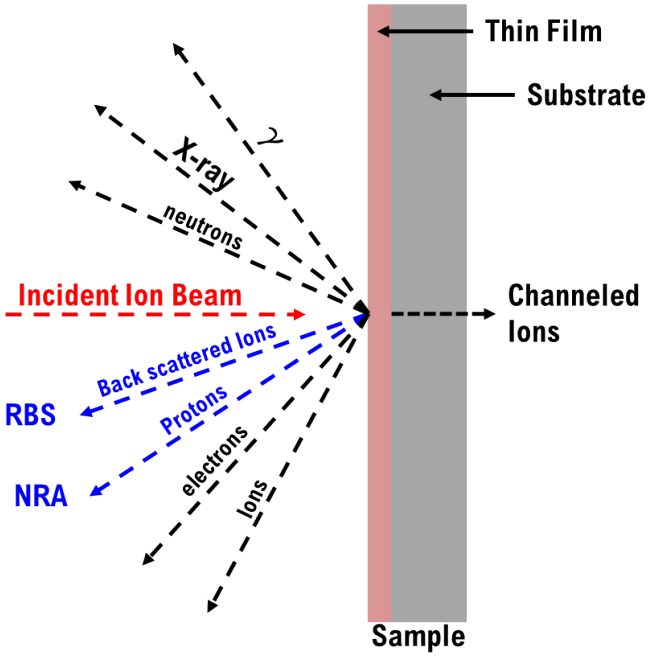

Fig. 2.12 Possible products resulting from the interaction between high energy ions and matter, blue dashed lines show the backscattering geometry of Rutherford backscattering spectrometry (RBS) and nuclear reaction analysis (NRA). Other techniques use different products for different measurements. In addition part of the beam could pass through the single crystal substrate.

IBA is a set of different techniques used depending on the aim of the measurements, whether the interest is in the concentration of elements or isotopes, heavy or light elements depth profiling of ultra thin layers or relatively thick layers etc. As the interest of this work is in thin films and the depth profiling of light elements, e.g., nitrogen and oxygen in a heavy matrix like tungsten, only a few techniques will be used.

The setup of such technique is big compared with normal lab experiments, due to the size of the high-voltage-accelerator and the integrated experiments as shown in Fig. 2.13. Except for few cases, IBA requires and is performed in ultra high vacuum chambers. IBA main parts are:

Ion source either from a plasma ion source for gaseous species or sputtering source for solid targets.

Injector magnet used to filter the ion beam to a single ion mass and guide it to the accelerator.

Magnetic lenses to shape the beam, control its optical shape and focus it.

High energy magnet used to switch the beam to one of the experiments chambers.

The experiment chamber is normally where the beam interacts with the sample, for that, special detectors are chosen and mounted in the suitable geometry corresponding to each performed technique

The sample is mounted on a manipulator for precise positioning, as well as controlling the angle of the incident beam on the sample. Detectors are the backbone of IBA, there are many different types of detectors designed for specific purposes, e.g., ionization chambers, scintillation detectors or semiconductor detectors. However, most of them share one feature which is counting nuclear particles and measure their energies.

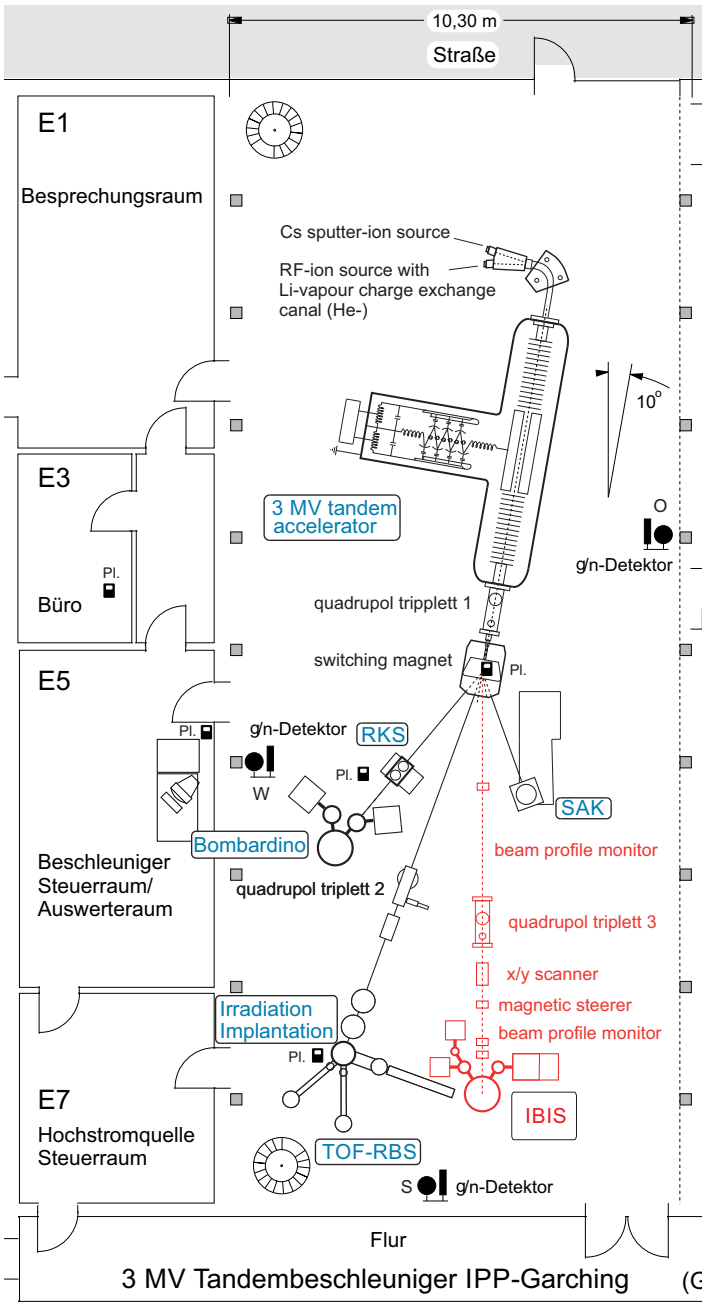

Fig. 2.13 Schematic illustration of the IBA setup showing the beam-lines for all experiments.

Among IBA techniques, Rutherford Backscattering Spectroscopy (RBS) and Nuclear Reaction Analysis (NRA) were used and will be discussed in more details. It is important to comprehend how such measurements work and how the data is collected and analyzed. Also, how accurate the interpretation of the results is, in order to minimize the uncertainty and perform reliable analysis. Following is an overview of how the techniques work and the theory behind each one.

2.2.2.1 Rutherford Backscattering Spectroscopy (RBS)

Rutherford backscattering spectroscopy (RBS) is a very classical technique dedicated to reveal the secrets of the atomic structure. When Rutherford, with his colleagues, bombarded a gold thin layer with energetic alpha particles, a back scattered signal along the line of incidence was recorded, which was interpreted as an explanation of the Coulomb interaction with a massive positive particle. That in return proved that the atom has the positive charge centered in the core not diffused as it was thought.

The basic idea of RBS is simply explained by the kinematics of binary collisions, where particles, normally ions, with mass M_1 and energy E_0 hit the sample atoms. Since the energy and momentum are conserved, it is then possible to determine the target mass M_2 by measuring the scattering angle θ and the energy of the scattered particles E_1. By taking the scattering geometry to be the so called IBM geometry [42], where the incident beam, exit beam and the normal on the surface, lie all in one plane as shown in Fig. 2.14. we have

$$\alpha + \beta + \theta = 180^\circ \tag{2.5}$$

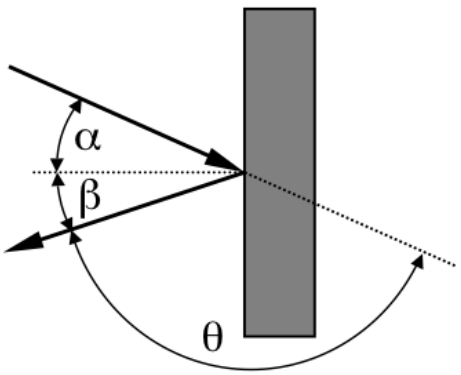

Fig. 2.14 The back scattering IBMgeometry where θ is the scattering angle [42].

In the laboratory system, the energy of the back scattered particles E_1 is calculated by

$$E_1 = KE_0 \tag{2.6}$$

where K is called the kinematic factor and equals

$$K = \frac{M_1^2}{(M_1+M_2)^2}\left\{\cos\theta \pm \left[\left(\frac{M_2}{M_1}\right)^2 - \sin^2\theta\right]^{1/2}\right\}^2 \tag{2.7}$$

where M_1 is the projectile mass, M_2 is the target atom mass, which is initially at rest, and θ is the scattering angle. In eq.2.7 the plus sign holds only if $M_1 < M_2$ [42].

Furthermore, in order to estimate the abundance of such mass, i.e. the elemental concentrations, the so-called Rutherford cross section gives the probability of scattering of particles as a function of scattering angle (eq. 2.8). By knowing the solid angle of the detector, counting the particles in the detector at each energy gives directly the elemental concentrations (see eq. 2.9 below). The Rutherford cross section σ_R depends on the charge and the mass of the projectile, the target atoms mass, the projectile energy and the scattering angle. For a certain projectile, σ_R scales with the square of the target material Z_2^2, i.e., signal from high Z material, like W, is much higher than low Z like N. It is valid for almost all element combinations at sufficiently low energy. Of course, the details depend on the specific projectile target combination. In this work, He ions were used for the analysis of W and N compounds. For these combinations the cross section is given by the Rutherford cross section up to energies $\sim 3\ MeV$, with cross sections at 1 MeV 28426, 222.47 mb/sr respectively and at 3 MeV 3226.48, 24.75 mb/sr respectively calculated using eq. 2.8.

$$\sigma_R\ [mb/sr] = 5.1837436\times 10^6\left(\frac{Z_1 Z_2}{E\ [keV]}\right)^2 \frac{\left\{(M_2^2 - M_1^2\sin^2\theta)^{1/2} + M_2\cos\theta\right\}^2}{M_2\sin^4\theta(M_2^2 - M_1^2\sin^2\theta)^{1/2}} \tag{2.8}$$

Since the beam energy E_0 itself is affected by traveling through the material due to electrons and nuclei collisions in a process called stopping, it is necessary to have an idea about the amount of the lost energy to accurately calculate the depth profile, i.e., the elemental concentration through the sample. The lost energy ΔE per distance Δx is called the stopping power dE/dx. Therefore, by knowing the the stopping power for each element, the lost energy per distance (depth) is estimated. Such effect is important, even more important at low energies $< 100\ keV$. The stopping power depends on energy and it increases with decreasing energy.

Fig. 2.15 shows a simple schematics of the RBS main components. High energy ions are provided from the accelerator guided by a strong switching magnet to RBS experiment chamber. The beam is then shaped and focussed to the sample using magnetic lenses. The total charge Q is collected by measuring the current through the sample and integrate it over the measurement time. Backscattered particles are collected in a silicon detector and the signal is then amplified and analysed using a multichannel analyser and finally recorded on data acquisition system.

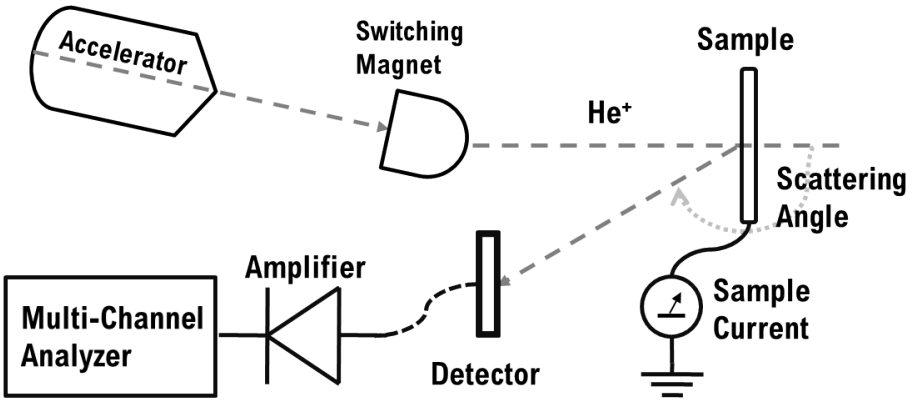

Fig. 2.15 Schematic drawing of RBS setup showing the main components. The gray dashed line shows the beam path.

In order to evaluate the acquired signal and estimate the elemental concentrations, the used unit is called areal density n which is the atomic concentration per unit area. In contrast to N which is the atomic concentration per unit Volume, when the thickness is d, $n = Nd$ and is evaluated simply using eq. 2.9 where A is the total integral counts of the peak, θ is the scattering angle, Q is collected charge (total ions), Ω is the detector solid angle and $\frac{d\sigma}{d\theta}(E)$ is the differential cross section.

$$n = \frac{A\cos\theta}{Q\Omega\frac{d\sigma}{d\theta}(E)} \tag{2.9}$$

Since in the work presented here, the analyzed layers are composed of tungsten and nitrogen, the estimated stoichiometry was taken to be the ratio between the areal densities of these two elements:

$$\frac{n_N}{n_W} = \frac{A_W\frac{d\sigma_N}{d\theta}(E)}{A_N\frac{d\sigma_W}{d\theta}(E)} \tag{2.10}$$

RBS is efficiently used to quantify heavy elements in light matrix within it is resolution limit. However, based on the Z^2 dependence of the cross section, the nitrogen signal is very low compared with the tungsten signal. Besides, the nitrogen signal overlaps with the silicon signal from the substrate. Therefore, an indirect measurements of nitrogen was performed by measuring the absence of tungsten in the films which will be explained later on. For these measurements, beams of α-particles with energies in the range $1.5-3\ MeV$ were used for RBS and and other experiments.

The measurements were performed in the RKS chamber which is shown in Fig. 2.13. The samples were mounted on a sample holder, tightly fixed as shown in Fig. 2.16a and each sample position was recorded. The holder then was mounted on the manipulator in a load-lock without breaking the vacuum of the measurement chamber as shown in Fig.2.16b. From the control-room, the manipulator was driven back to the main chamber and then the samples were positioned with accuracy of $0.1\ mm$

to be measured. The measurement geometry is taken to have the beam normal on the surface while the detector is fixed at a scattering angle of 165°. The beam energy and characteristics are adjusted by the responsible person. By the acquisition software, the value of charge to be collected, i.e. number of ions hit the sample, is set to 20 μC and the measurement stops automatically when the set charge is collected.

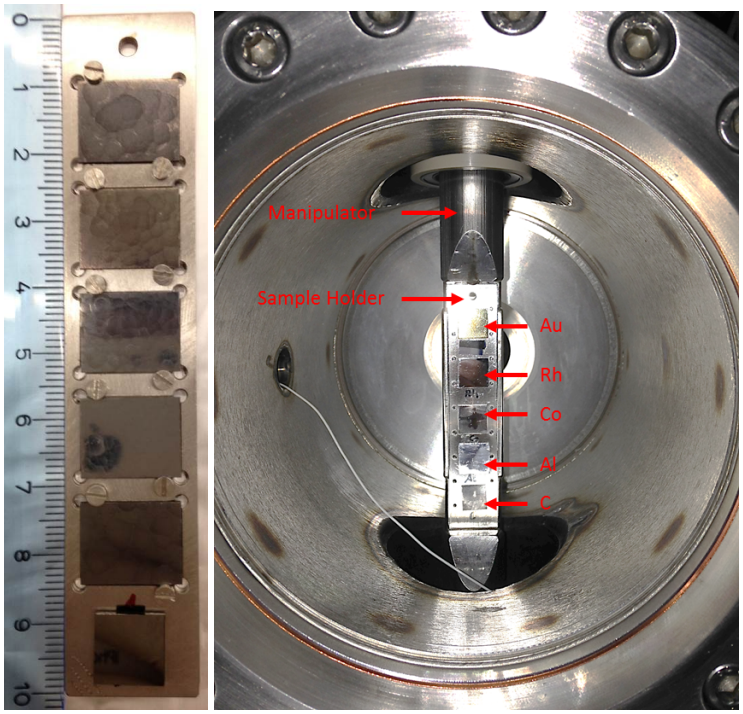

(a) **(b)**

Fig. 2.16 (a) The samples mounted on the sample holder. Next to the holder a a *cm*-scale for reference. (b) shows the load lock chamber with the calibration samples on the sample holder mounted on the manipulator.

Fig. 2.17 shows a typical RBS spectrum using He^+ ions at 3.4 MeV to measure a WN_x thin film on a silicon substrate. The signal consists of a separate peak corresponding to W at the high energy side of the graph, the signal from the Si substrate is given by a step starting at about 1300 keV and extending down to very low energies. The nitrogen signal overlaps with the Si substrate signal in the energy range 500 to 700 keV. It is hardly visible in Fig. 2.17. The position of the element peak depends on the energy of the recoiled particles which is calculated by the kinematics from eq.'s 2.6 and 2.7. The peak height is defined by the cross section and the stopping of the material. Therefore, the signal of nitrogen is so low compared with tungsten. Typically the raw data is simply the counts of the particles per energy channel. A simulation software is used to correctly extract the quantitative data from the measurements. The used software is SIMNRA© [43] and it is used to simulate the whole experiment. Some input parameters are needed for the simulation such as:

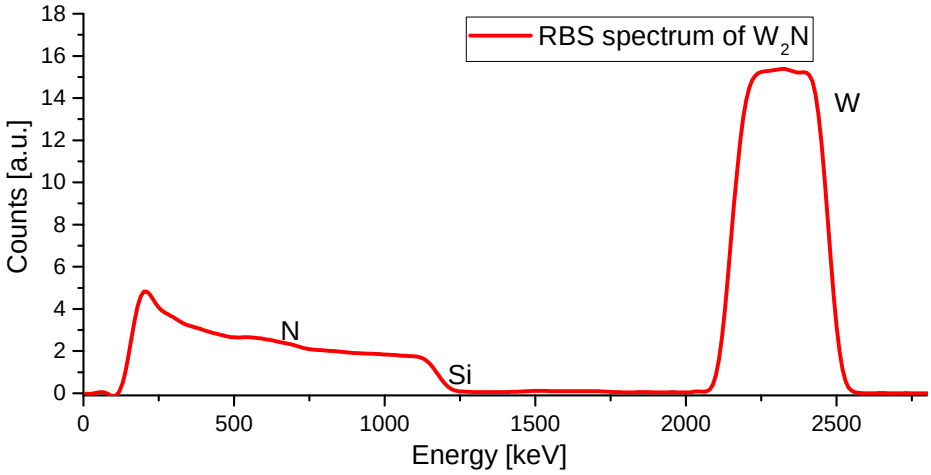

Fig. 2.17 Typical RBS spectrum of WN_x on *Si* substrate where the number of counts is plotted as a function of the backscattering energy. On the right hand-side the surface peak of tungsten followed by the substrate edge and the nitrogen peak overlapped with the *Si*-signal is on the left hand-side. The data is smoothed for better representation.

Energy calibration Which gives the energy per channel plus the offset. There are few methods to calibrate the energy, The used one is by measuring the energy of back scattered α-particles from the surface of specific materials covering almost the full range of energies as shown in Fig. 2.18. Besides, the kinematics of each interaction for each material using the beam energy is calculated. By knowing the channel number of each surface (step) from the spectrum, and the corresponding energy of that channel from the kinematics, the energy per channel can be assigned.

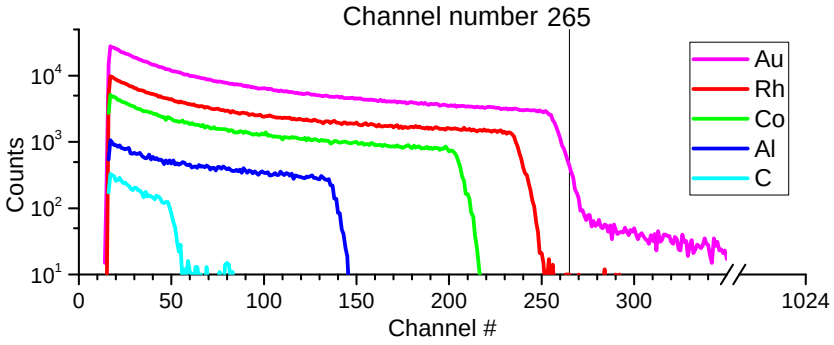

, the step-like shape of the graph is due to the stopping and is typical for bulk samples, the height of the step depends on the cross section (RBS cross section depends on Z^2) for each element at the given energy.

Fig. 2.18 Calibration spectrum from the five calibration samples from different materials. Showing that peak position depends on the element, i.e. used for element identification

Detector resolution and solid angle it is a characteristic value of the detector within the used geometry. The used detector is a silicon detector with 25 *mm* active area and thickness of $\sim 500\ \mu m$, resolution of 10 *keV* and a solid angle Ω of $1.108 \pm 0.038\ msr$.

Beam shape and current Current measurement is an essential factor for proper simulation, the current is integrated over the measurement time to estimate the total collected charge the current taken to be in the range $25-70\ nA$ and the collected charge in the range $10-100\ \mu C$. Moreover, to estimate the areal density it is necessary to provide the area of the beam spot which is chosen to be 1 *mm*.

Detector dead time Such value depends on the beam current as the detector is able to record a limited number of events within a certain period of time. Such value is recorded by the system based on the detector type.

Thin film material(s) and the rough composition In order to reduce the simulation time and the uncertainties, it is useful to provide an initial description of the sample i.e. elements in the film, number of layers, thickness range and substrate material.

After performing the simulation, the software calculates the areal density of the elemental concentrations in the units ($10^{15}\ atom/cm^2$). By using the density, the thickness in *nm* is calculated as

$$t(nm) = \frac{n}{N} = \frac{n}{\frac{\rho}{A} \times 6.022 * 10^{23}\ mol^{-1}} \tag{2.11}$$

where n is the areal density (eq. 2.9), N is the number density, t is the thickness ρ is the bulk density and A is the atomic mass, once N (or ρ) are known (see Sec. 4.2).

Since RBS has a complex setup, although each source of error is somehow taken into account to be minimized, a collective uncertainty is found to be $\sim 5-10\%$ of the measured values. Among those uncertainties, few examples can be mentioned such as, energy, solid angle, beam spot area, electronic gain, detector resolution, scattering angle, stopping power in the material and multiple scattering.The largest source of uncertainty is current measurement and 5% is an optimistic assumption.

2.2.2.2 Nuclear Reaction Analysis (NRA)

Another important technique from IBA is nuclear reaction analysis (NRA). It is used to provide, up to a high degree of accuracy, the concentrations of specific isotopes in certain thin samples with high depth resolution. Specific projectiles (ion species) are selected with certain kinetic energy where a nuclear reaction could occur (with certain probability known as cross section). In most cases, the reaction happens within a very narrow energy window known as the resonance. The products of such

reaction are nuclear particles or radiation which are measured by special detectors and provide a specific quantitative information after careful calibration [44].

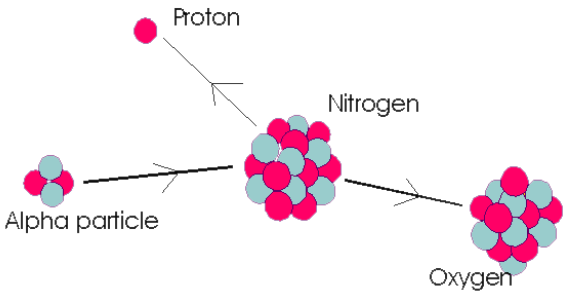

Fig. 2.19 Schematic drawing of the $^{14}N(\alpha, p_0)^{17}O$ reaction resulting in a backscattered proton and oxygen-17, the proton detector is placed at a scattering angle of 135° such reaction happens usually in a narrow resonance which could provide good depth resolution of thin sampls. [45]

The used reaction is $^{14}N(\alpha, p_0)^{17}O$ with the proton detector at angle of 135° Fig. 2.19 illustrates the reaction. The drawback of this specific nuclear reaction is that cross section has a series of sharp resonances as shown in Appx. A. A single sharp resonance would be preferable for analysis of thicker layers, however, the series of the existing resonance peaks close to each other makes the interpretation difficult. Because of the energy loss in the material (stopping), only thin samples (up to $\sim 200\ nm$) can be measured quantitatively. This method was applied during this work for thin layers only to measure the total nitrogen amount in the layers.

2.2.3 Thermal Desorption Spectroscopy (TDS)

Thermal desorption spectroscopy (TDS) also called temperature programmed desorption (TPD) is a robust method to investigate the desorption behavior of retained atoms and molecules from the surface as a function of the temperature. It is also used as a quantitative measurement of the nitrogen amount when a proper calibration is performed. It uses a quadrupole mass spectrometer (QMS) to detect the mass of the desorbed atoms and molecules. By integrating the spectrum, quantitative information can be obtained.

Fig. 2.20 shows a schematic drawing of the used device. A detailed explanation can be found in [46]. In short, the setup works in ultra high vacuum (UHV) in the $10^{-9}\ Pa$ range. While the temperature is ramped up with a fixed rate, the QMS measures the specified masses of the desorbed species and is the data is recorded via computer interface.

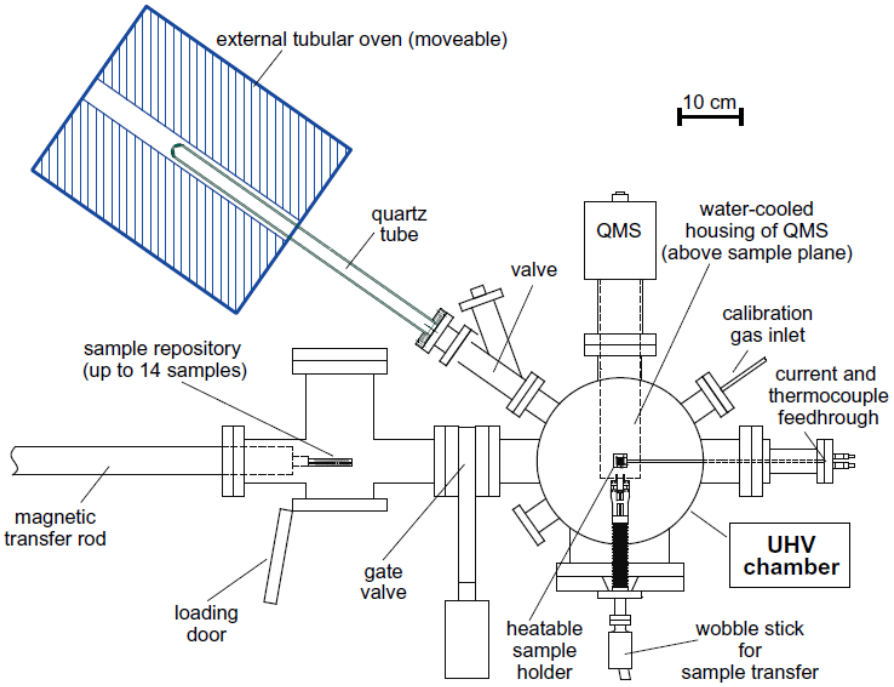

Fig. 2.20 Schematic drawing of TDS setup showing the used external oven in light blue as well as the quartz tube connected to the UHV chamber with a valve. The QMS is also connected to the chamber. [46]

The experiment is carried out by placing the sample in the quartz tube and then the system is let to pump down overnight. Once a good vacuum is achieved, the temperature is ramped up with an adjustable rate, the used one is 15 K/min up to $\sim$ 1300 K. Meanwhile, the QMS is recording the atomic masses: $2, 3, 4, 12, 14, 15, 16, 17, 18, 19, 20, 28, 32, 40$ and 44 u as a function of time. Fig. 2.21 shows a typical spectrum as a function of QMS cycle (corresponding to time) together with the temperature measurements.

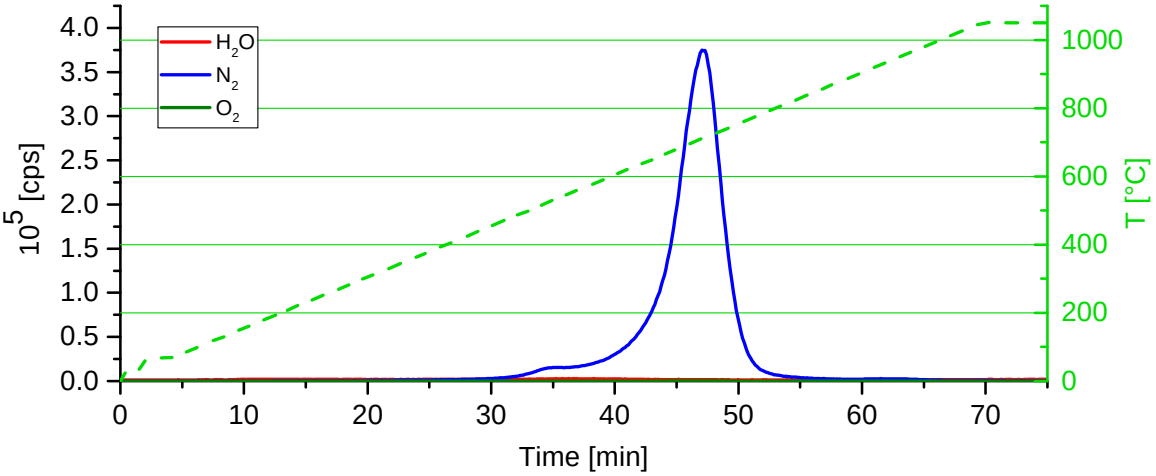

Fig. 2.21 Typical QMS raw signals plotted versus the QMS cycle, corresponding to time, and on the right *y*-axis is the temperature (black solid line) ramped up with a fixed rate of 15 k/min. The evolution of some signals is clear like N_2 mass 28 and Ar mass 40.

In order to extract the absolute desorbed amounts of each gas species, QMS calibration is critical. For that purpose a helium leak bottle is used to calibrate the detector sensitivity. By calibrating the detector for helium, and by knowing the ionization probability for each gas the calibration factors can be obtained and the desorption rate can be estimated.

After evaluating the data and calculating the desorbtion rate of each species, the total desorbed species is calculated by integrating over the heating time after background subtraction. Since both QMS signal and temperature measurements are functions of time, the QMS signal is interpolated as a function of temperature for better illustration of the thermal behavior of the material.

2.2.4 Scanning Electron Microscope (SEM)

During the optimization process, it is important to get a quick overview of the surface morphology and the micro-structure of the fabricated layers and to understand how the deposition parameters affect the layers growth. Since optical microscopes have a resolution limit of $\sim 0.2\ \mu m$, it is necessary to go beyond that limit to probe the micro-details of the produced samples and that is done using SEM with resolution $\sim 1.0\ nm$.

SEM is a very common technique used to get high resolution images with high magnification [47]. Since electrons have the wave nature, as proved by de Broglie, a much shorter wavelength than visible light can be obtained which is the key for the high resolution. It utilizes an electron beam focused to $\sim 1.0\ nm$-spot to raster the surface of the specimen line by line forming a matrix, while measuring the intensity of the interaction signals (products) between the electron beam and the material at each point. As shown in Fig. 2.22, when an electron-beam hits the surface, many signals are produced

and recorded by different detectors. Those signals carry many information about the material surface-morphology, however, secondary electrons signal is more frequently used. Afterwards, the collected signals are mapped in images as brightness variation stored digitally on long storage memory.

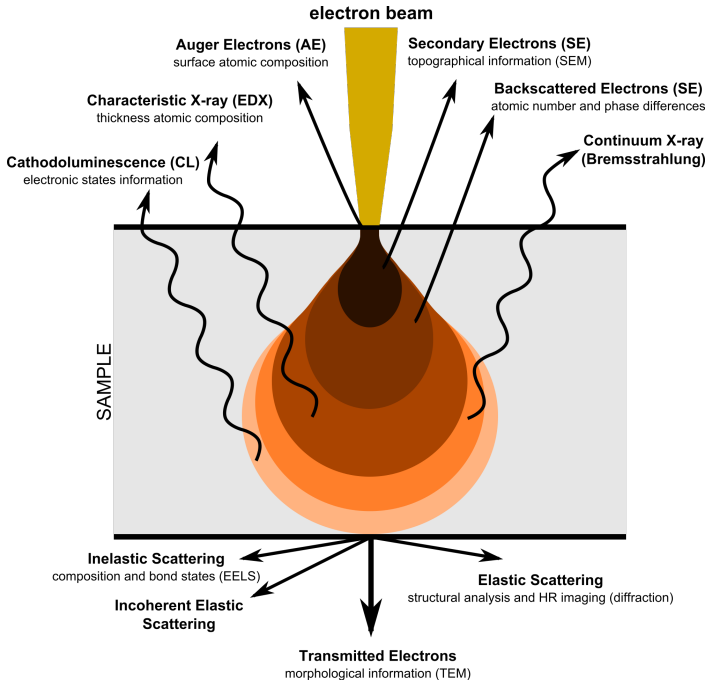

Fig. 2.22 Schematic drawing of electron-material interaction showing all possible products, the relative depth of each interaction and the possible scattering and transmission. Each product of interaction could be measured with a specific detector and provide characteristic information about the material of the sample and the micro-structure. [48]

The samples must have a clean surface or they have to be cleaned with ultra-pure products to prevent any hydrocarbon layers on the surface. In addition, the surface must be conductive as in the case of WN_x otherwise a special coating with a thin-layer of gold has to be made. The specimens are then glued on the sample holder with conductive carbon-tab to eliminate the vibration during the measurements and ensure good conductivity. Finally, the sample holder is mounted on the device, closed and pumped down. The acceleration voltage is normally 5 keV up to 30 keV in some cases. Beside measuring the surface morphology, a cross-section imaging is possible using FIB, as explained in Sec. 2.2.5.1.

2.2.5 Transmission Electron Microscopy (TEM)

Transmission electron microscopy (TEM) is another technique of imaging using electron beam, however, in this case, the sample is thin enough to be transparent for electrons (< 200 nm). Through different interactions within the specimen, very detailed information are obtained. Depending on the scope of interest, TEM can provide e.g. high resolution morphology images, crystal structure

information using electron diffraction, material identification via characteristic X-rays generation and sample composition determination using energy-dispersive x-ray spectroscopy or electron energy loss spectroscopy etc. More detailed information can be found in [49].

It is important to mention, in short, the idea behind electron diffraction as it is been used through this work, however, for more details see [50]. Since electrons are treated as waves, their diffraction is not different from what has been shown for XRD in sec. 2.2.1, but in contrast to XRD, the diffraction happens after transmission not reflection. Fig. 2.23 shows the scattering of electron beam in a crystal, where part of the beam is transmitted without deviation, another part is diffracted by the atomic planes and a small part is scattered in other directions. By projecting the 3D-diffraction on a 2D-screen, different patterns can be formed depending on the crystallinity as shown in Fig. 2.24.

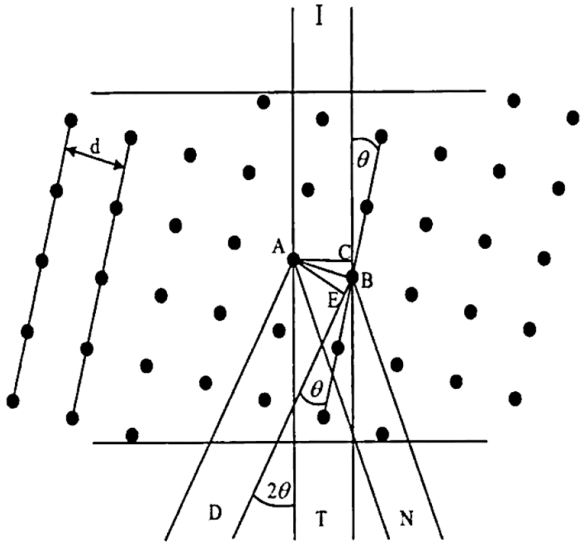

Fig. 2.23 Schematic drawing of the possible trajectories of a high energy ion-beam with intensity I within a crystalline specimen. The beam might transmit with intensity T forming a contrast image, scatter randomly N without intense spots or get diffracted by the crystal planes of spacing d forming diffraction patterns.[50]

In order to interpret such patterns to get information about the crystal structure and lattice constant as shown in Fig. 2.25 (for simplicity the focus will be on a cubic lattice) the procedure is as following:

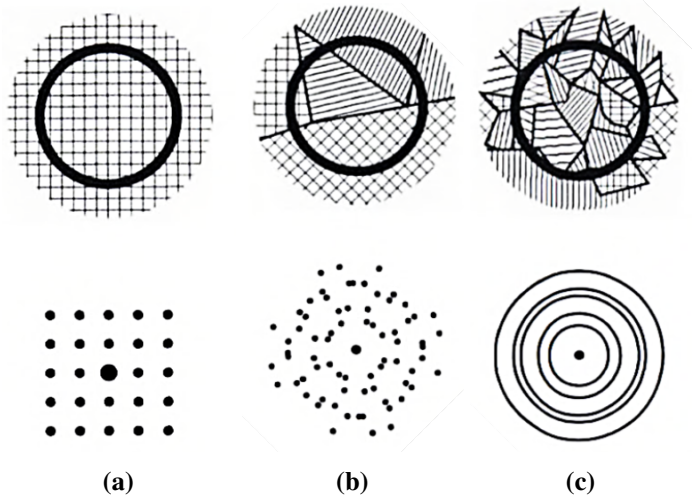

Fig. 2.24 Schematic illustration of the typical diffraction patterns (lower part) as a function of the material crystallinity (upper side), i.e., the grain size and their orientation. (a) shows the typical diffraction pattern of a single crystal cubic lattice with (100) orientation. (b) shows the typical diffraction pattern of few grains with different orientation which somehow can be recognized. (c) shows the typical diffraction rings of a poly crystalline material where the grains are oriented in all possible directions.[50]

1. The image is calibrated using the existing scale
2. Two spots close to the central spot of the diffraction pattern are taken and the r values are measured i.e. the distance (radius) from the center.
3. The angle between the two spots α is measured as the center is a connecting point.
4. The interplanar spacing d_1 and d_2 are calculated as the reciprocal $\frac{1}{r}$ where r is calibrated.
5. The indices are calculated as explained in [50] however, table 2.1 summarize the first eight possible reflections for a cubic lattice.

Table 2.1 The first eigh allowed reflections in the fcc crystal structure and their interplanar spacings to easily interpret W_2N rings, i.e., by comparing the order of appearance with the table order.[50]

Indices	111	200	220	311	222	331	422	333
$h^2+k^2+l^2$	3	4	8	11	12	19	24	27
d/a	$1/\sqrt{(3)}$	$1/2$	$1/2\sqrt{(2)}$	$1/\sqrt{(11)}$	$1/3\sqrt{(2)}$	$1/\sqrt{(19)}$	$1/2\sqrt{(6)}$	$1/3\sqrt{(3)}$

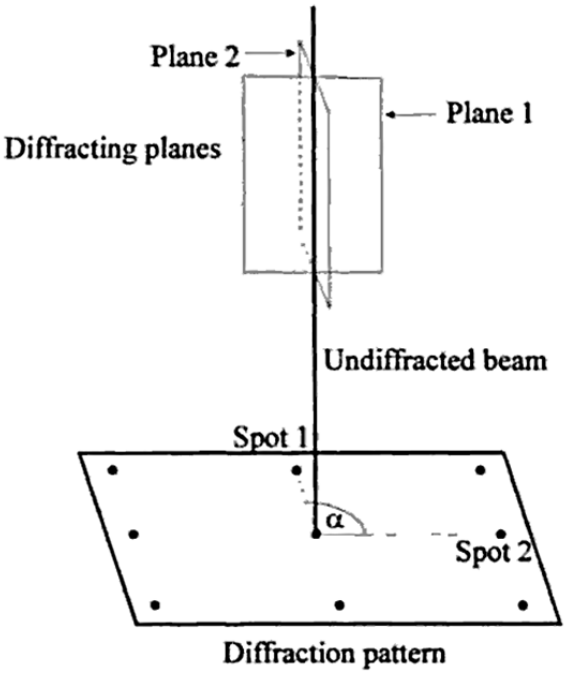

Fig. 2.25 Schematic drawing of a diffraction pattern from one crystal showing the crystallographic planes, the diffraction spots and the angle between the spots α. [50]

2.2.5.1 Focused Ion Beam (FIB)

Focused ion beam (FIB) is a high-tech technique used in many scientific and industrial fields [51], where an ultra-thin specimen is needed to be scanned with TEM (Sec. 2.2.5) or EDX (Sec. 2.2.5.2). FIB is a very powerful tool to fabricate thin specimen with high precision. In contrast to conventional SEM, which usually is incorporated with FIB, it uses an ion beam and by focusing the beam, the energy is sufficient to cut and sputter the material. It is commonly attached to SEM devices. The working principle of FIB, is simply Ga^+ ions gets accelerated in high electric field to bombard the material surface with *nm*-beam-width to knock out the material atoms. Fig. 2.26 shows a fabricated specimen (lamella) for TEM measurements with thickness $\sim 50\ nm$. The used device is HITACHI nanoDUE'T NB5000 with Ga liquid metal ion source, with accelerating voltage of $1-40\ kV$ and a beam current $\sim\ 50nA$. A detailed explanation of lamella fabrication process with FIB is given in Appx. B.

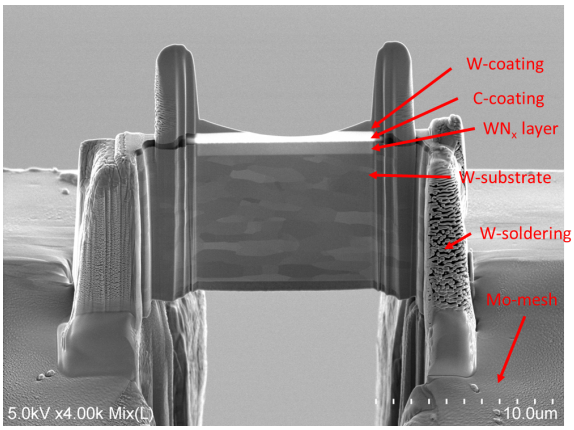

Fig. 2.26 SEM image of a lamella which was fabricated using FIB showing the C- and W-coatings to preserve the surface during cutting and the supporting Mo-structure.

2.2.5.2 Energy-Dispersive X-ray Spectroscopy (EDX)

Energy-dispersive X-ray spectroscopy (EDX) is also used for chemical composition analysis [52]. The basic idea of such measurements is the characteristic X-ray radiation of each element, where a specific set of peaks is obtained matched with a database. In EDX, a high energy-beam of particles (electrons or ions) is used to excite the atoms allowing a relaxation by X-ray emission. Fig. 2.27 shows a schematic of the EDX measurements.

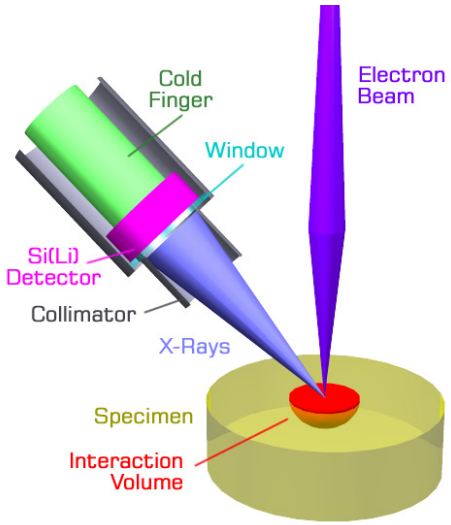

Fig. 2.27 Schematic drawing of EDX showing the working principle where an electron-beam scans the surface and at each point the interaction leads to the emission of characteristic x-ray which is then collected and detected using a Si(Li) detector. That detector needs to be working at low temperature normally cooled down by liquid nitrogen.[53]

Normally, EDX is performed along with SEM or TEM using a special detector, using the SEM electron-beam to scan the speciment surface and recording the X-ray intensities at each point mapping an image with elements concentrations. The beam spot size of the impinging electron beam is comparable in SEM and TEM. The main difference for EDX is the interaction volume (see e.g. Fig. 2.22). In bulk material it is up to 1 μm diameter, however, for thin lamellas it is mostly determined be the beam diameter. Moreover, TEM can be used in the so-called scanning transmission microscopy (STEM) mode, where even a much smaller electron-beam-spot size scans the surface as a conventional SEM. Since the sample thickness and the beam spot in STEM have very low dimensions, the resolution is much higher than that of SEM.

2.2.5.3 Electron Backscattered Diffraction (EBSD)

Another type of detectors which is attached normally with TEM or SEM to measure the diffraction of the backscattered electrons from the material surface. It provides information, most of the time quantitative, about the microstructure and the crystallography of most of the inorganic materials e.g. grain size, grain orientations phase, and texture etc. The angular resolution is $\sim 0.5^{\circ}$ and the special resolution, depending on the electron microscope, is ~ 20 *nm*.

2.2.6 X-ray Photoelectron Spectroscopy (XPS)

X-ray photoelectron spectroscopy (XPS) is a semi-quantitative method which is very sensitive for the surface [54]. It provides information about the elemental composition, chemical bonding and electronic state for the samples. When a beam of monochromatic X-ray (or energetic photons source) irradiates the surface as shown in Figure 2.28, photoelectrons are released with different kinetic energy depending on their bond energy. Those electrons are analyzed as they are characteristic for each element and electron configuration. In order to perform such measurements, ultra high vacuum (UHV) is required $P < 10^{-9} mbar$

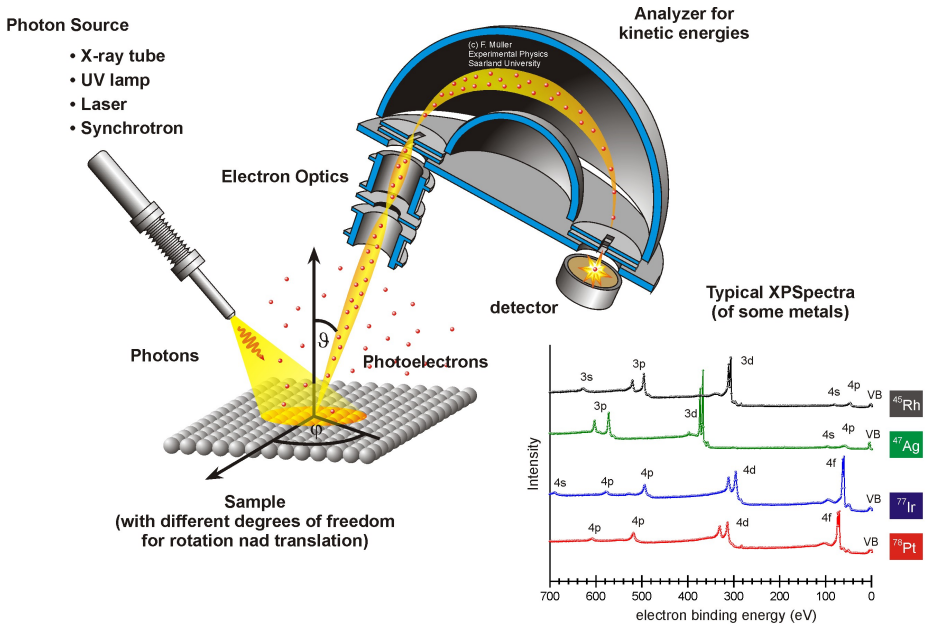

Fig. 2.28 Schematic drawing of XPS setup showing the working principle where the material surface is illuminated with a photon source resulting in an emission of photoelectrons. Such photoelectrons are then focused and guided to an analyzer which separate the electrons based on their kinetic energies. In the lower right side some typical spectrum of pure elements where the electron intensity is plotted versus the electron kinetic energy. [55]

2.2.7 Glow Discharge Optical Emission Spectrometry (GDOES)

Glow Discharge Optical Emission Spectrometry (GDOES) is used to perform surface analysis and depth profiling for elemental composition on materials surfaces [56]. It uses the sample as a cathode and when a voltage is applied between the sample and an anode, a discharge occur resulting in physical sputtering to the material. Sputtered atoms then enter the plasma and become excited by collisions with the plasma electrons. The excited atoms in the plasma, normally argon plasma, emit characteristic line radiation. The emitted radiation has to be filtered out and amplified as its intensity is very low compared with the background. As the line radiation is characteristic to each material, it is important to separate different wavelengths and that is done using polychromators which measure the intensity of each wavelength using spectrometers providing accurate information about the abundancy of the elements. Although it is not easy to provide quantitative information, it is very sensitive for impurities and elemental detection.

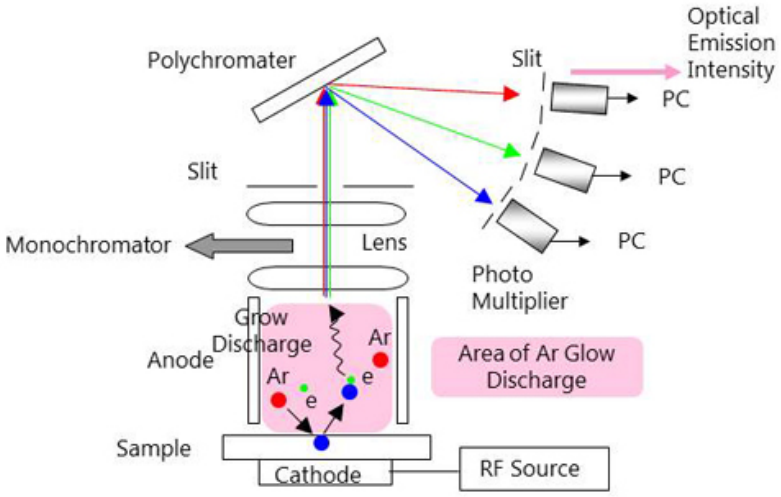

Fig. 2.29 Schematic illustration of the working principle of GDOES, where the material of the sample is sputtered via a glow discharge, ionized and the emitted photons are collected with optical lenses. The collected photons are separated based on their different wavelengths and the intensity of each wavelength is then measured and matched to the elements line radiation. [57]

Fig. 2.29 shows the a schematic drawings of GDOES, where the emitted photons is collected and focused using lenses. They are then guided to the polychromator where each wave length is separated and its intensity is measured using an array of detectors.

2.2.8 Nano Indenter

Nanoindentation is normally the same concept as macro or micro indentation test and it's is used to measure the mechanical properties (especially the hardness) of thin films. In the measurements, an ultra hard tip with known mechanical properties (commonly diamond) with a pyramidal shape (see Fig. fig:33) is applied normal to the surface of a material with unknown mechanical properties with a linear increase of the applied load. [58]. As a result, the surface of the material is deformed due to the applied load, with depth depending mainly on the material mechanical properties. By plotting the tip displacement h (the depth see Fig. 2.30a) as a function of the applied load P in a graph, we can estimate the hardness as

$$H = \frac{P_{max}}{A}$$

Where H is the hardness, P_{max} is the maximum applied load and A is the indentation area.

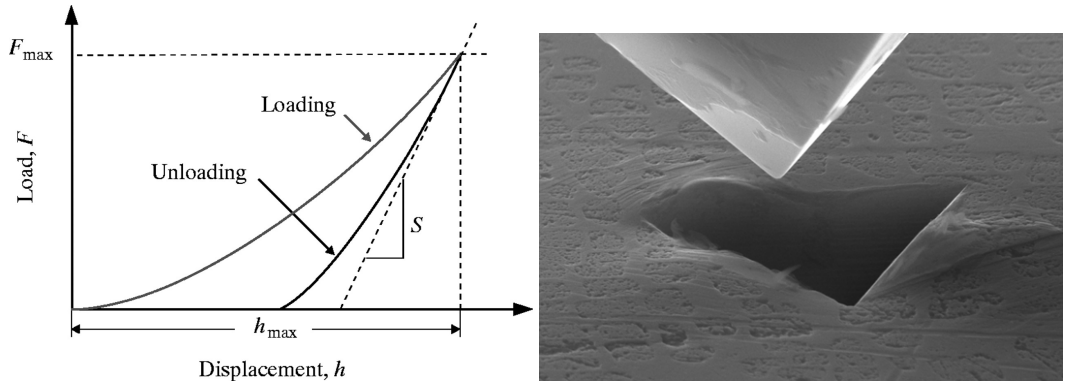

Fig. 2.30 (a) Typical load-displacement curve where the applied load is plotted versus the tip depth or the displacement from the surface [59]. (b) Image of the pyramidal tip and the indent on the surface after the load was applied [60].

Fig.2.30a, shows a typical load-displacement curve, from which most of the mechanical properties can be extracted e.g. hardness, elasticity plastic and viscous parameters. Fig. 2.30b shows the pyramidal tip and the indentation footprint where Vickers hardness could also estimated from the indent dimensions as a function of the applied load.

2.3 Chapter Summary

In this chapter the fabrication process of tungsten nitride thin films were explained. Furthermore, most of the characterization techniques were explained in terms of the working principles, the measurements procedures and data analysis. More emphasis was put on ion beam analysis and X-ray diffraction as they were considered the main techniques.

Chapter 3

Progress in WN_x Fabrication

A major obstacle in fabricating WN_x layers with few μm thickness was the high residual stress which leads to a damage (delamination) of the deposited layers once they are exposed to the atmosphere as shown in Fig.3.1a. For that reason, an optimization process had to be carried out to determine the best deposition conditions for each deposited layer. This optimization process aims at low residual stress, good crystallinity, acceptable density and suitable thickness. Almost all the deposition parameters were investigated to get an idea about how big the effect of each parameter on the layer is. That process required keeping all the parameters fixed since investigating the influence of one specific parameter. A closer look was taken at the total pressure, the deposition power, RF power vs. DC power, the applied current, the distance between the target and the substrate, the deposition angle, the rotation speed vs. fixed substrate holder, the deposition time, the layer thickness and finally the distance between the anode and cathode of the sputtering target.

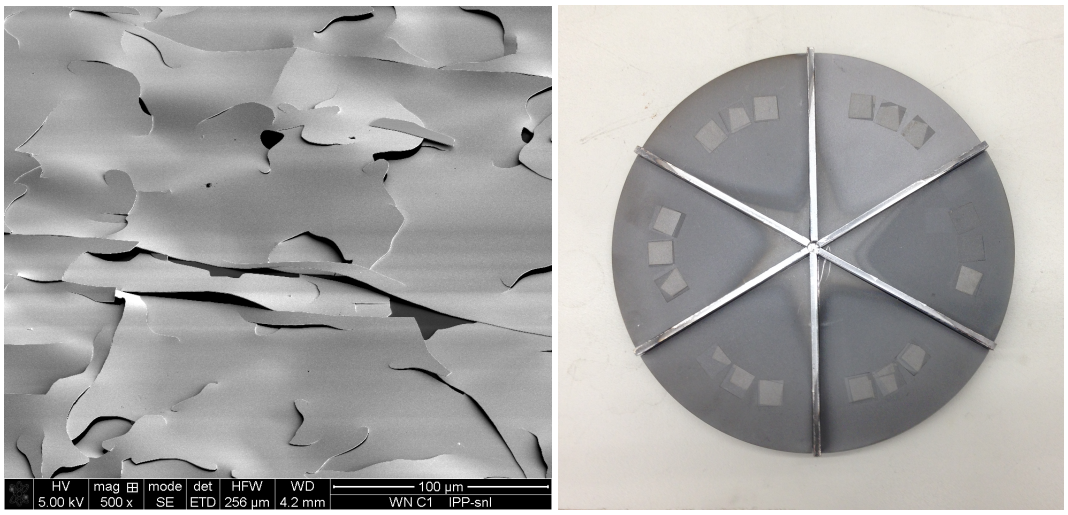

(a) **(b)**

Fig. 3.1 (a) SEM image of a delaminated WN_x layer, once it was exposed to the atmospheric pressure, due to the residual stress. (b) An image of a simple substrate holder used during the optimization process in order to study the effect of each deposition parameter, while ensuring all the other parameters remain constant, i.e., not even switching off the plasma. It uses a movable shutter to cover all the substrates, after the etching process, during the deposition except for one-sixth. No substrate-rotation was used during the application of this method.

In order to assure no other parameter could contribute to that study and to precisely investigate one parameter at a time within the shortest time window and without breaking the vacuum or doing a lot of mechanical movements, a simple substrate holder was designed for that purpose. Prior investigations showed that stationary substrate showed better layers micro-structure in comparison to rotating substrate. In addition, the sample size was either 10×10 mm^2 or 12×15 mm^2 which showed a negligible thickness variation across the sample and no noticeable differences to the neighboring samples. Careful positioning was applied to eliminate any non linearity due to sample position.

Fig. 3.1b shows the substrate holder designed to perform up to six depositions while fixing all the conditions and investigate only one parameter. During the deposition, only one-sixth of the holder was exposed to the sputtered particles, while the rest was masked out. In addition, a horizontal mask, a 10 mm-height wall between the samples formed a closed box to fully isolate the rest of the samples from the ongoing deposition. No substrate-rotation was used during the application of this method.

Applying this method allowed to scan a wide range of parameters and to successfully fabricate crystalline tungsten nitride thin films. In addition to that, a valve was installed in front of the turbomolecular pump to control the pressure in the chamber. Depositions on silicon, tungsten and graphite substrates with layers thickness in the range between 100 nm to 5 μm were successfully made. Using the gained knowledge of the effect of each parameter on the produced layers, helped to produce stable layers with different properties. Among those properties was the stoichiometry, i. e., the nitrogen-tungsten ratio in the layer. The resulting phase was, mainly, dependent on the nitrogen partial pressure in the deposition chamber which ranged from 5% up to 100%. The interesting observation

was that no phases mixture was ever observed, which makes the transition point from one phase to another, if there is any, ambiguous.

Another interesting observation is that no target poisoning was observed under the applied deposition conditions when a *DC* power was used, even though depositions in pure N_2 (i. e.100% N_2 and 0% Ar) atmosphere were performed. No plasma failure has ever been recorded and that can be ascribed to the electrical conductivity of WN_x or the sputtering-ions energy at powers grater than 150 W.

3.1 Main Characterization Techniques

3.1.1 XRD Measurements

XRD gives direct information about the chemical phase, and it has the advantage of a relatively easy interpretation. It can also provide an estimate of the grain size, residual stress and the texture of the layer. That made it a reliable method for primary characterization. Fig. 3.2 shows a typical XRD pattern (blue curve) indexed with β-W_2N reference positions [61]. Those peaks infer some interesting information, first of all, a strong texture in the orientation of [111]. In addition, some residual stress can be observed as the measured peaks are shifted from the database values. Table 3.1 shows all measured peaks with the corresponding shift to the database peaks. The shown figure is one of the clearest obtained XRD patterns, after adjustment of the deposition conditions. Other deposited layers showed much more residual stress which led, in some cases, to film delamination.

Table 3.1 XRD diffraction peaks comparison between the measured values and the database.

(hkl)	2θ measured [°]	2θ database [°]	shift [°]
111	37.15	37.74	0.59
200	42.91	43.85	0.94
220	62.53	63.74	1.21
311	74.82	76.52	1.7
222	79.16	80.60	1.44
400	94.35	96.69	2.34
331	106.37	108.86	2.49
420	110.11	113.14	3.03

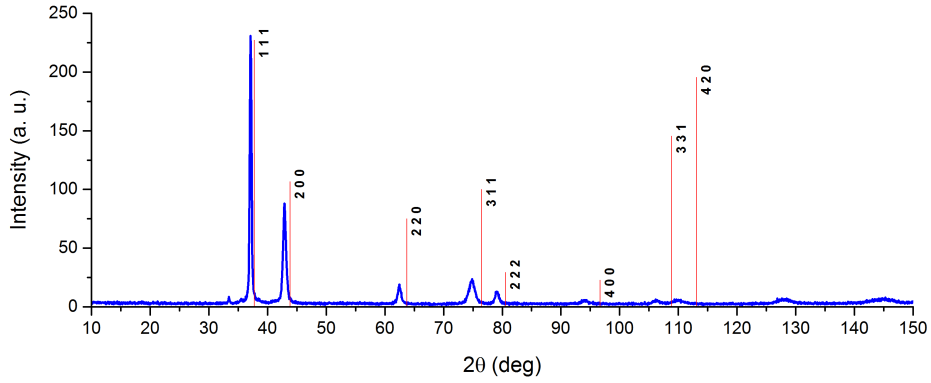

Fig. 3.2 XRD patterns of tungsten nitride W_2N (blue line) compared with the database peak positions(red lines).

As mentioned before, XRD was used as a quick tool to characterize the deposited layer, which in turn gives a direct feedback in order to adjust the deposition parameters. The total pressure showed an important role in managing the stress in the layers. Fig 3.3 shows the effect of the total pressure in terms of the crystallinity (the peak width and height) and the residual stress (the peak shift). That can be assigned to the energy-change of the impinging particles on the surface of the substrate during the deposition.

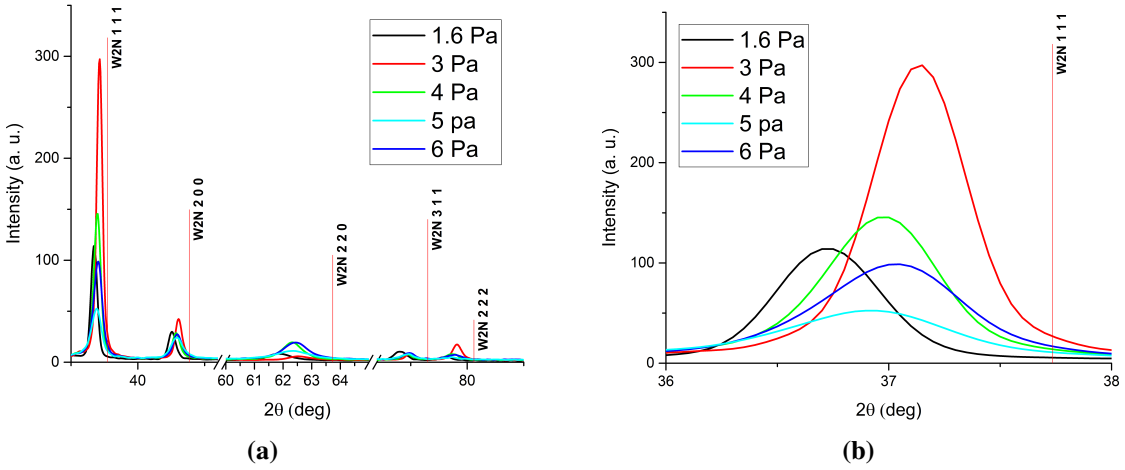

Fig. 3.3 XRD patterns of WN_x shows the effect of the chamber total pressure. (a) Only the peaks are shown with axis breaks. (b) A zoom-in to the most intense peak ([111]) shows the peak shift as a function of the chamber total pressure. No monotonic behavior can be seen.

3.1.2 More Accurate RBS Measurements

The RBS current measurements are very crucial for accurate data interpretation. Since nitrogen has a low RBS signal, as its cross section is much lower than tungsten, the nitrogen concentration in the layer had to be estimated from the difference in tungsten areal density of the WN_x to the bulk-W areal density. Therefore, it was very useful to cover the samples with an identical thin W coating, i. e., all

the measured samples were coated with tungsten via sputtering in the same deposition run. In that case, a fitting to the W-layer peak can provide an accurate calibration which in turn will be a universal reference to compare all the measured samples as shown in Fig. 3.4.

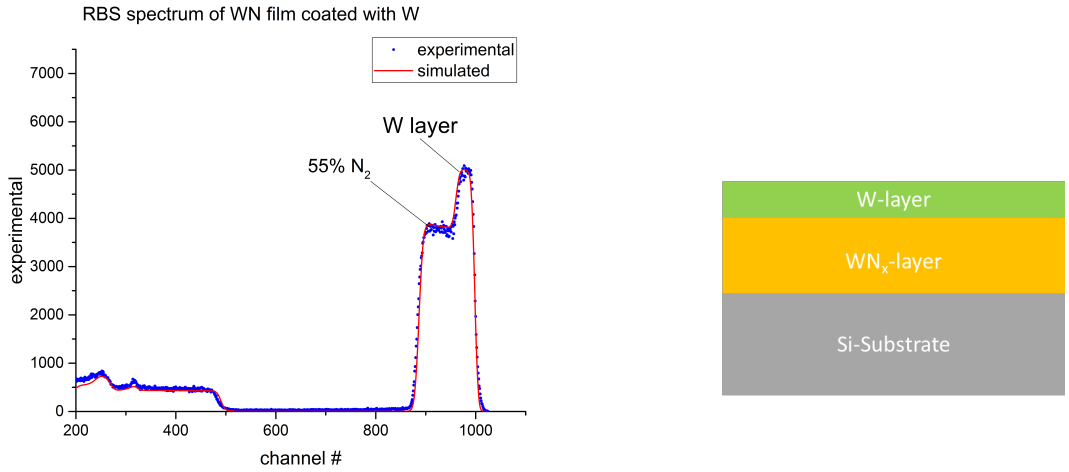

Fig. 3.4 The used method to reduce the uncertainty in the RBS measurements, namely, the current measurements. (a) A typical RBS spectrum measured by 3815 keV $^4He^+$ shows the first W-peak followed by the WN_x peak simulated using SIMNRA. In that case an in-situ current calibration is made. (b) A schematic drawing of the layers system used for that method.

3.2 Nitrogen Content vs. N_2-Partial Pressure

The nitrogen partial pressure or the nitrogen-argon flow rate ratio is a key parameter to determine the nitrogen content in the produced layers. That was also reported by other researchers [62]. In order to study that closely, depositions with different Ar/N_2 ratios were performed. The Ar flow rate was in the range of $0-60$ $sccm$ and the nitrogen was in the range $5-120$ $sccm$ while keeping the total pressure constant. Measuring the partial pressure was not possible with the available setup, but a feeling about the partial pressure can be obtained by measuring the corresponding pressure for a certain flow rate for each gas as shown in Fig. 3.5 where "$sccm$" refers to a standard cubic centimeter per minute.

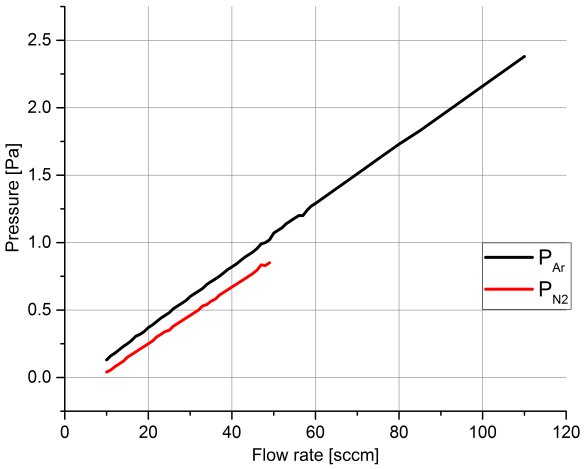

Fig. 3.5 A graph representation shows the measured conversion relation from *sccm* to *Pa* for both *Ar* (black line) and N_2 (red line).

It is believed that the resulting WN_x phase is a function of the nitrogen partial pressure in the argon-nitrogen sputtering gas mixture. Some researchers reported a phase transformation from W_2N to WN by increasing the nitrogen partial pressure but with a poor crystallinity [62]. A closer look to the XRD patterns of layers which were produced at different nitrogen partial pressures are shown in Fig. 3.6b. The nitrogen flow rate, which is directly correlated to the nitrogen partial pressure, was changed from 10 *sccm* to 25 *sccm* while keeping the argon flow rate constant at 60 *sccm*. The effect of the nitrogen partial pressure on the phase formation is not clear. However, a slight shift of the peaks positions was observed. Fig. 3.6b shows that the highest peak (111) has different shifts, in comparison with the reference position, as the nitrogen flow rate changes, however, the shift is not monotonic.

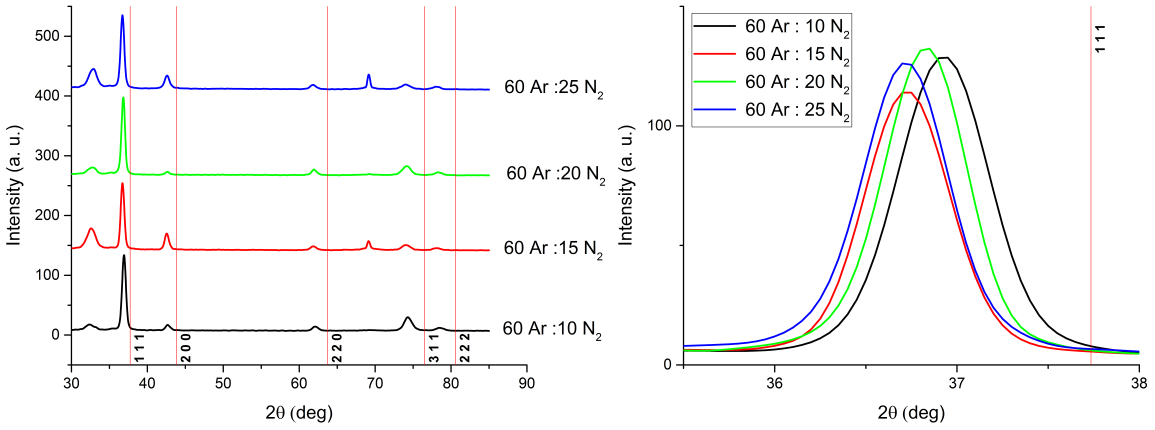

Fig. 3.6 XRD patterns of different W_2N layers shows the effect of the $Ar : N_2$ relative flow rate (partial pressures). (a) A comparison of four samples with a constant *Ar* flow rate of 60 *sccm* while the N_2 is set to 10, 15, 20 and 25. (b) a zoom-in to the comparison of the most intense peak ([111]) shows the peak shift as a function of the N_2 flow.

On the other hand, further increase of the N_2 partial pressure led to different observations. When the gas mixture was 50% Ar and 50% N_2 no W_2N XRD pattern was observed, however, small peaks appeared in the position of WN phase indicating a formation of a different phase as shown in Fig. 3.7a. The intensity of the peak is very low due to the poor crystallinity, however, it is similar to what was reported in [62].

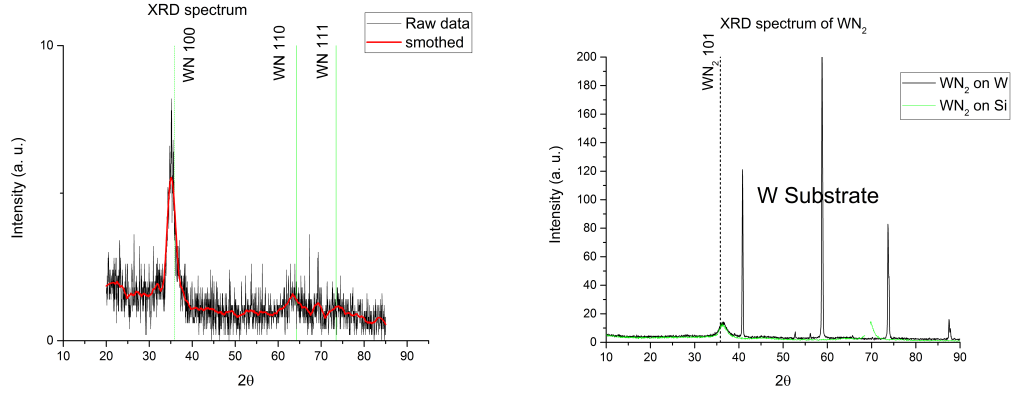

Fig. 3.7 XRD patterns of layers deposited with higher N_2 percentage in the gas mixture. (a) Deposited at $Ar : N_2$ flow rate ratio of 50 : 50 resulted in a transition from W_2N to, most likely, WN, however the peaks intensity are very low. (b) Deposited in pure N_2 atmosphere as a sputtering gas. As only one peak (broad) was observed at $\sim 35.0°$, deposition on W (black line) and on Si (green line) substrates were made to exclude any substrate contribution.

Performing deposition in pure N_2 atmosphere for the sputtering process showed a different XRD pattern as shown in Fig. 3.7b. To eliminate any possible doubt that this small peak is a contribution from the substrate (e. g. double reflection in the substrate material [63]), the deposition was made on silicon substrate and tungsten substrate simultaneously. Both spectra showed this peak in the exact position which corresponds to a WN_2 [101] peak. As the XRD data is not conclusive that this phase is WN_2, further investigations are necessary, e.g., RBS.

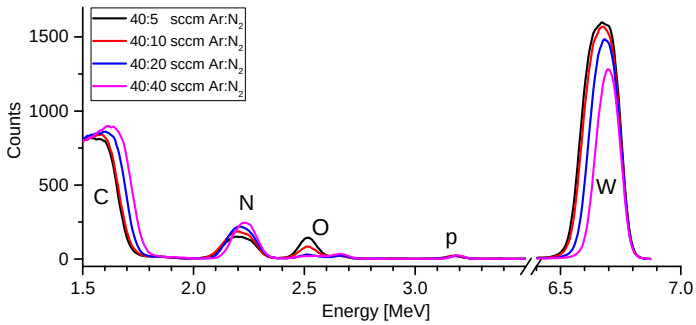

Fig. 3.8 Typical RBS spectra of WN_x layers deposited at different $Ar : N_2$ ratios on graphite substrates. These samples were measured using 7414 keV^4He^{++}. Different peaks can be seen from the right hand side: a tungsten peak, a proton peak from $^{14}N(\alpha, p_0)^{17}O$ reaction, an oxygen peak which is relatively big since it has a much higher cross section than nitrogen, the nitrogen peak and finally the carbon substrate. It can be seen that the nitrogen and the tungsten content in the layers varies by varying the nitrogen flow rate from 10% up to 100%

Fig. 3.8 shows RBS spectra of layers deposited at different N_2-partial pressure. It is clear that the W-peak integral changes by changing the N_2 flow rate. Fig. 3.9 shows the nitrogen-NRA signal of the same samples as Fig. 3.8. A clear change of the proton-peak integral can be seen. That was just the raw-data, however. It is important to take into account that the peak integral should be normalized to the sample thickness to get the total amount, since the samples in most cases have different thicknesses.

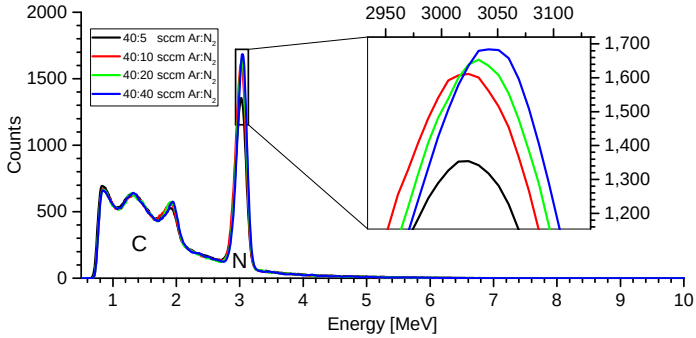

Fig. 3.9 The proton signal for the Nitrogen-NRA measured simultaneously with RBS for the same samples shown in Fig. 3.8. It shows the same trend, i.e., the peak integral which represents the nitrogen amount changes as a function of the nitrogen flow rate. The peak integral is a function of the sample thickness as well, therefore it must be normalized for a correct interpretation.

Fig. 3.10a shows the RBS spectrum of a W_2N sample and the estimated nitrogen concentration is $\sim 38\%$ which is in agreement with the literature value $(33\% - 50\%)$ [30]. The thickness of the sample was $\sim 4\ \mu m$ and in this case the silicon substrate is not seen. In case of the WN sample Fig.3.10b, the nitrogen concentration is $\sim 55\%$ which is in a good agreement with the chemical stoichiometry. This sample was deposited on Si substrate with thickness of the layer $\sim 0.7\ \mu m$ and also the nitrogen peak can be seen around channel no. 250. The last phase is WN_2 where it is deposited on W-substrate with

thickness $\sim 1.0\ \mu m$. The nitrogen concentration in this layer from the simulation is $\sim 67\%$ which is the exact stoichiometric value of this phase as shown in Fig. 3.10c.

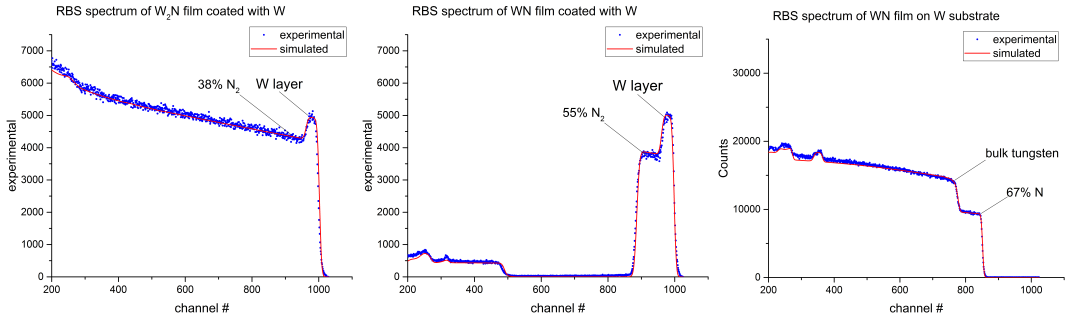

(a) **(b)** **(c)**

Fig. 3.10 Typical RBS spectra measured at 3.8 MeV $^4He^+$ of three samples with different stoichiometries. (a) WN_x layer deposited on Si substrate, has a thickness $\sim 4.0\ \mu m$ and is covered with a thin pure-W layer. This layer contains $\sim 38.0\ at.\%\ N$ which is close to W_2N phase. (b) WN_x layer deposited on Si substrate, has a thickness $\sim 0.7\ \mu m$ and is covered with a thin pure-W layer. This layer contains $\sim 55.0\ at.\%\ N$ which is close to WN phase. (c) WN_x layer deposited on W substrate, has a thickness $\sim 1.0\ \mu m$. This layer contains $\sim 67.0\ at.\%\ N$ which is close to WN_2 phase.

3.3 Bias Effect

The negative substrate bias is an effective parameter on the thin films micro-structure in general. It was also shown that it affects the properties of WN_x [64]. To study the effect of the bias on the nitrogen content, layers deposited at identical conditions and only changing the bias power namely: 0, 10, 20 and 50 W RF, were used. That resulted in self-bias voltages of 0, 92, 176 and 325 V respectively. Fig. 3.11 shows typical RBS spectra of the samples where it can be seen that no change in the W amount in the layer, i. e., no change in the nitrogen content is detected. A slight change in the peak width, which is correlated to the sample thickness, can be due to an effect on the cathode bias or a re-sputtering of the deposited film.

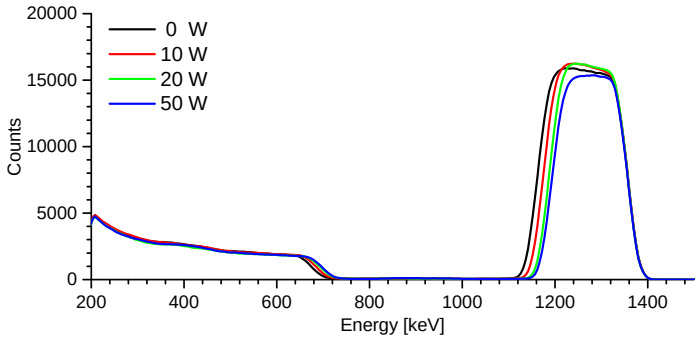

Fig. 3.11 Different layers deposited at the same $Ar : N_2$ gas flow ratio of 15 : 15 *sccm*. All the conditions were kept constant except for the substrate bias was set to different values of $0, 10, 20$ and 50 W of RF power resulting in self biasing voltages of $0,\ 92,\ 176$ and 325 V, respectively. It can be seen that the layer thickness decreases by increasing the bias power. That can be due to a re-sputtering of the deposited-layers by the energetic ions, or a change in the plasma parameters.

3.4 Layers Micro-Structure Using SEM and TEM

The micro-structure of the deposited layers is essential for the quality of WN_x layers and it was necessary to get a closer look into the deposited layers. The analysis included the surface morphology, cross section scanning, high resolution TEM, STEM and TEM diffraction. In the following, these results are explained in some details and the relative analysis is performed.

SEM measurements were performed to image the sample surface at different magnifications up to $X100,000$ which is around the limits of traditional SEM, and from that the surface morphology is identified. The SEM images showed a strong dependence on the deposition conditions, the substrate type, the nitrogen amount in the layers and the annealing temperature. Fig. 3.12 shows the surface morphology of the three discussed stoichiometries, deposited on *Si*, where the deposition parameters are summarized in Table 3.2.

Table 3.2 Summary of the deposition parameters of the three probable stoichiometries.

Parameter	W_2N	WN	WN_2
Ar gas flow	60 *sccm*	30 *sccm*	0 *sccm*
N_2 gas flow	15 *sccm*	40 *sccm*	50 *sccm*
Chamber pressure	3 *Pa*	2 *Pa*	3 *Pa*
Sputtering Power	300 *W*	300 *W*	300 *W*

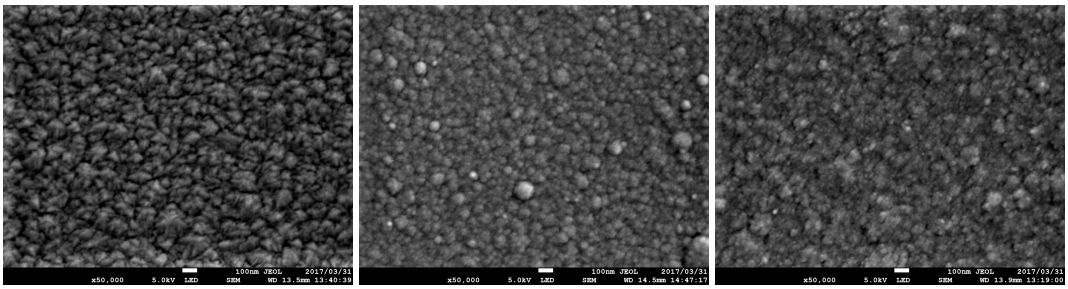

(a) **(b)** **(c)**

Fig. 3.12 SEM images of the surface morphology of three WN_x layers have different stoichiometries as discussed earlier. (a) W_2N, (b) WN and (c) WN_2.

With TEM, two types of imaging were performed, namely, high resolution transmission electron microscopy (HRTEM) and transmission electron diffraction TED. The fabrication process of a thin-enough specimen (lamella) of ~ 50 *nm* using FIB is explained in Appendix B. The TEM was used to investigate the micro structure of some layers, estimate the grain size and obtain the electron diffraction patterns when it was used in the diffraction mode. Fig. 3.13 shows the porous-like structure of a W_2N sample by changing the focus point of the beam, pores show a change in the contrast from black to white.

(a) **(b)** **(c)**

Fig. 3.13 HRTEM images (scale bare of 100 *nm*) show the micro structure of a W_2N specimen at different focusing points: (a) over focus, (b) just focus and (c) under focus. That can show the porous structure (the black points in Fig. (a) turn white in Fig. (c)). The change can only be seen on the small dot-like spots not on the big scale black areas.

3.5 Annealing Effect

XRD was used to investigate the effect of annealing on the produced layers. Fig. 3.14 shows the effect of annealing at $500°C$ for 10 *hrs*. Annealing at these conditions showed a small effect on the stress release and on the texture; [111] peak showed an increase in the intensity while[200] peak had a

decrease in the intensity. However the crystallinity, which is correlated to the FWHM of the main peak [111], almost remained the same before and after annealing.

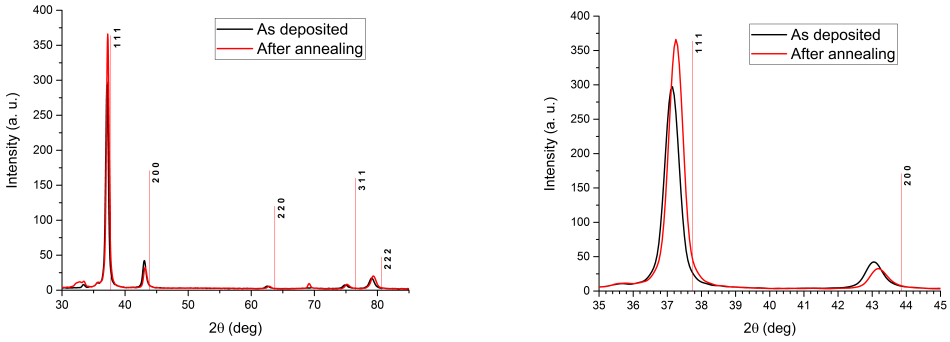

(a) **(b)**

Fig. 3.14 XRD patterns of a W_2N sample before and after annealing at 500 $°C$ for 10 *hrs*. (a) Performing annealing at these conditions had a minor effect on the layer. However no big change on the grain size (peak width) or on the residual stress (peak) shift can be seen. (b) a zoom-in to the most intense two peaks shows a slight change on the layer texture (the relative peak heights).

Annealing a W_2N layer at 800$°C$ for 30 *min* and quick cooling by just turning off the power led to an obvious stress relief (Fig. 3.15) but the intensity of the main peak was decreased and there was no effect on the HWFM of the peak, which means that the layer decomposes before the recrystallization can take place. Adjusting the cooling rate to be 1$°C/min$ led to a severe damage to the W_2N phase, in addition, a formation of pure α-W. It is interesting that at such conditions the shift in the W_2N peaks seemed to decrease to its ever-observed minimum.

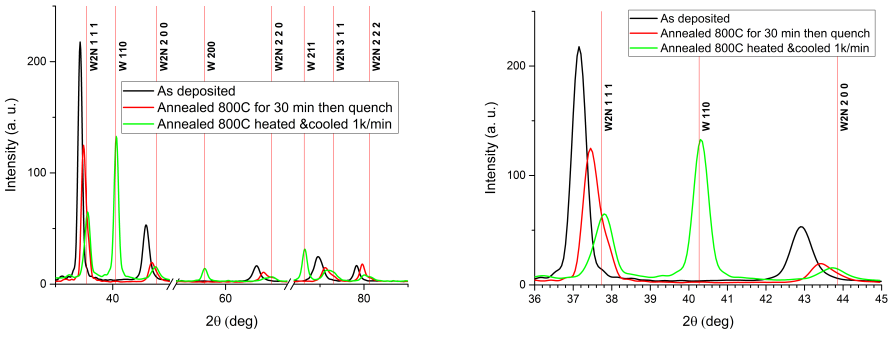

(a) **(b)**

Fig. 3.15 (a) XRD patterns of three identical W_2N samples before and after annealing at 800 $°C$ by the same heat ramp up of 15 K/min for two different holding times. First, for 30 *min* then cooled quickly by turning off the heating (red line). Second, for 10 *hrs* then cooled down slowly by a rate of 1 K/min. The latter led to a transformation from W_2N to pure-W. The slow cooling (longer annealing time) led to a decrease in the peaks intensity, however, no pure-W peaks observed. (b) A Zoom in to the most intense peaks show clearly the peak shifts and the intensity changes.

Not only the temperature seemed to be critical, also the annealing time seemed to play an important role. The mechanism of the decomposition of WN_x and the formation of pure W phase is still not clear as the recrystallization temperture of W is between $1300-1500°C$ [65]. Fig. 3.16b shows a comparison between the electron diffraction patterns of pre- and post-annealing. It can be seen that the diffused rings (right-hand side) were transformed to scattered spots which indicates a change in the micro-structure, i.e. grain growth. In addition, appearance of bright spots (green rings in the left-hand side) correspond to a formation of pure tungsten phase.

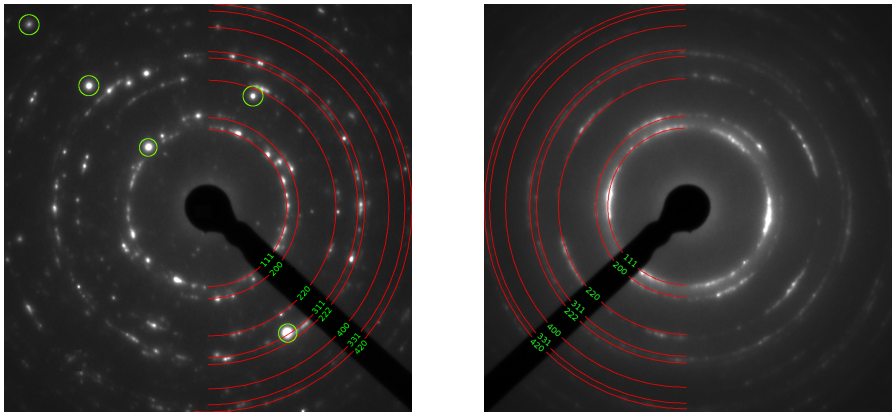

(a) **(b)**

Fig. 3.16 TEM images show the diffraction patterns of a W_2N sample after annealing (a) compared with before annealing (b). The images are indexed by the reference rings positions (red half-circles) of W_2N and the spots correspond to pure-W are marked (green circles). The effect of annealing can be seen by the discontinuity of the rings to form scattered spots.

3.6 Thermal Stability and Impurities Retention

Heat treatment of the layers, as discussed earlier in Sec. 3.5, led to nitrogen loss from the layers and partial formation of pure W. Such effect can, also, be seen as volume loss from the total layer volume. Fig. 3.17c shows confocal laser microscope images of the three discussed phases after heat treatment. These layers were heated, all together, up to $700°C$ for 3 *hrs* three times to ensure a total release of the nitrogen. The different layers show different cracking behavior. In addition, the size of the cracks network increases as a function of the existing N_2 content.

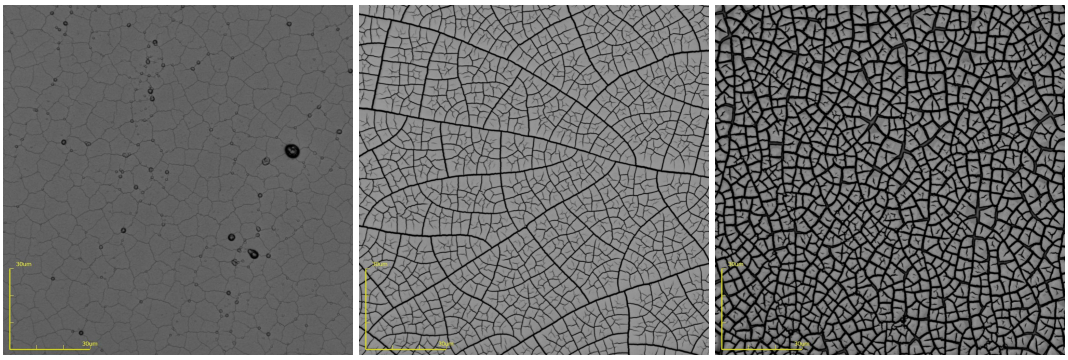

(a) **(b)** **(c)**

Fig. 3.17 Confocal laser microscope (CLM) images show the cracking network of the three different stoichiometries samples (a) W_2N, (b) WN and (c) WN_2. after annealing at 700 $^{\circ}C$ for 3 *hrs* three times. The image scale is 30 μm and is the same for all images.

Another approach to estimate the elemental composition with a quantitative method is EDX. By performing the measurements, a small peak around 3 keV corresponds to $Ar\ K_\alpha$ line which support the idea of argon retention in the layers. Fig. 3.18a shows the full spectrum of a W_2N sample deposited on *Si*. Fig. 3.18b is a zoom-in to show the Ar peak as well as N_2 and O_2.

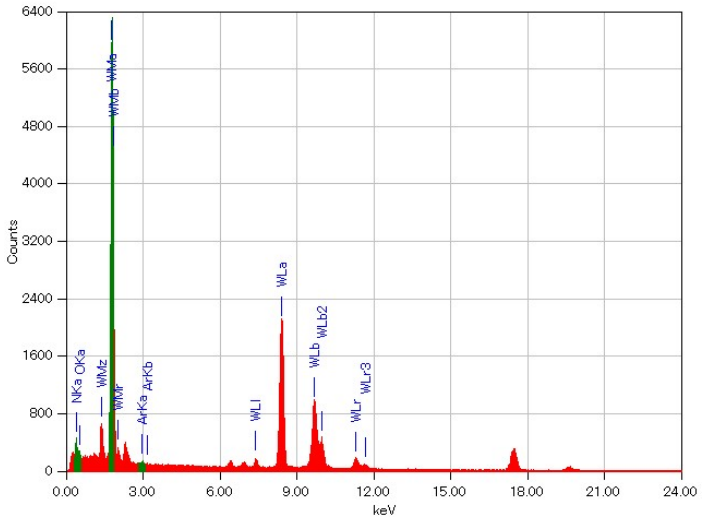

(a) bbb

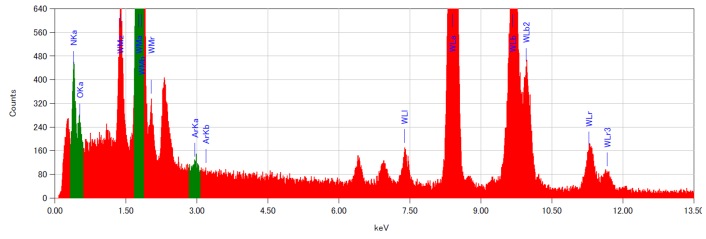

(b) bbb

Fig. 3.18 EDX spectrum of a W_2N (a) shows the peaks related to W and N. (b) a zoom-in shows an Ar-related peak with a measurable amount.

It is still not clear how the excess nitrogen is retained in the layer, although no mixed phases are observed. Different routes were taken to investigate other possibilities for retention. Fig.3.19d shows the nitrogen desorption behavior as a function of temperature up to 1300°C. First sample is W_2N and was annealed three times at 700°C, that is the reason why the nitrogen release starts around 700°C with a release peak around 950°C. Another interesting observation is the existence of a non-negligible amount of argon in comparison with WN_2 where no argon was recorded (EDX signals of light gasses are not accurate for quantification). It still is not clear how that big amount of Ar can be retained. Another open question is whether the nitrogen can be retained the same way as argon, i.e. without chemical bonding, or not. It is very important to understand the chemical properties of the layer to be able to fully characterize it.

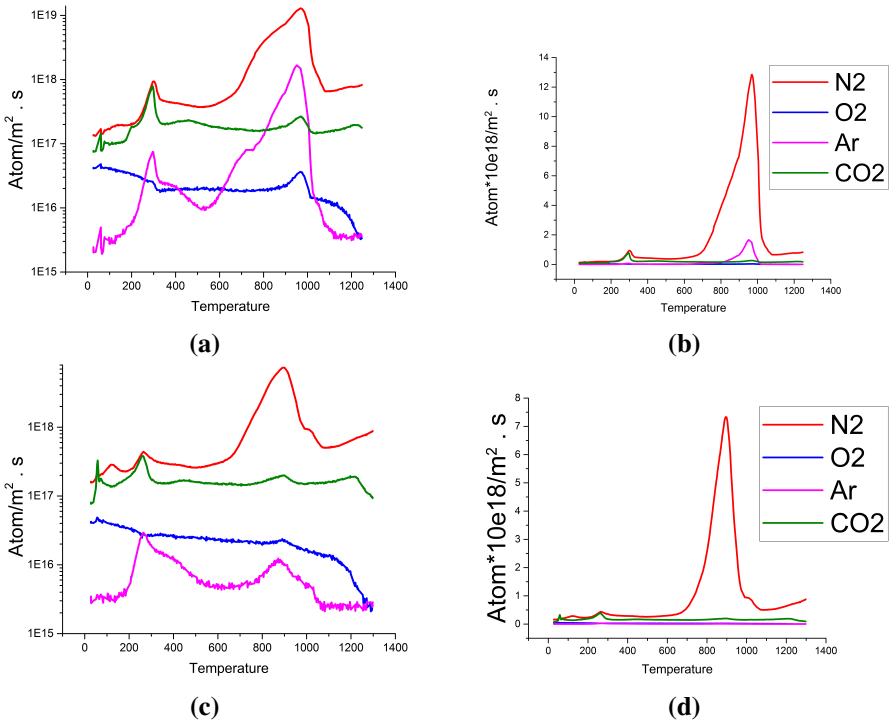

Fig. 3.19 TDS desorption spectra of a W_2N on a log-scale (a) and on a linear scale (b) and a WN_2 sample on a log-scale (c) and a on a linear- scale (d). The images show a comparison between a W_2N which is deposited in a gas mixture of Ar and N_2 vs. a WN_2 sample which was deposited in a pure N_2 atmosphere. The plots on the log scale show a release of Ar compared with the other which is a sign of gas retention. However, that can not explain where exactly that gas is retained.

Impurities in the deposited layers can be a major problem unless a careful consideration is taken into account. In order to recognize the main impurities species in the layers, GDOES was performed. Although it cannot give a quantitative information, it can give information on the depth distribution with high spatial resolution. From the measured samples, it can be seen that the main impurity species are hydrogen, carbon and oxygen, but they are detected only at the surface and at the interface with the substrate. This can be easily attributed to the adsorption of water vapor and carbon monoxide on the sample surface after being exposed to the air and also in the interface due to the adsorption on the substrate surface. Fig. 3.20 shows a depth profile of H_2, C and O_2 in a WN_2 sample in addition to W and N_2. The depth profile is made during sputtering out the material material surface. Since the the sputtering rate is almost constant, the time can linearly be correlated with the depth. Two signals of the mentioned impurities can be recognized correspond to the surface of the sample and the substrate. The measurements show that the profile of N_2 and W is homogeneous through out the whole layer.

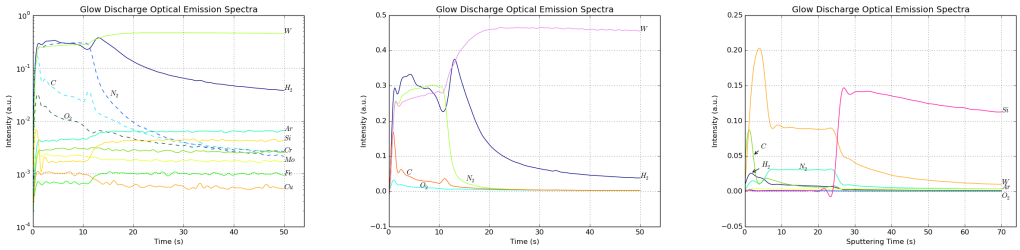

(a) **(b)** **(c)**

Fig. 3.20 GDOES spectra of: (a) WN_2 deposited on W plotted on a log-scale. (b) the same as the latter but on a linear scale. (c) W_2N deposited on Si substrate and covered with a thin pure W layer. The main impurities in the layers are identified as well as to the homogeneity of the layers is verified.

Fig. 3.20c shows an identical layer as the one shown in Fig. 3.20b, however, deposited on a silicon substrate and covered with a W-layer on top of the WN_2 layer. From that figure, it can be seen that hydrogen (or water vapor) adsorption on W is much more than on Si, however, that observation is not conclusive while the micro structure of the deposited tungsten is a key to explain such behavior. As the intensities of the signals need a proper calibration to be used as a quantitative analysis, they do not give a correct value of the absolute amounts.

To comprehend the mechanism of WN_x layers decomposition, EBSD was used to give an insight of how the nitrogen could get released from the layers and how the transition from WN_x to pure W could occur. By observing an annealed W_2N-layer at $800^{\circ}C$ with heating and cooling rate $2\ K/min$ one can see relatively large grains of pure W as shown in Fig. 3.21. That can be explained by the difference in size between the two cubic lattices W_2N and W where the lattice constants are $4.12 - 4.14\ \mathring{A}$ and $3.1648\ \mathring{A}$ respectively. That can lead to $\sim 45\%$ shrinking of the of the grains volume which in turn leads to cracking. In addition, the thermal expansion mismatch between the film and the substrate could also lead to such cracking, however, what happens first is still under investigation.

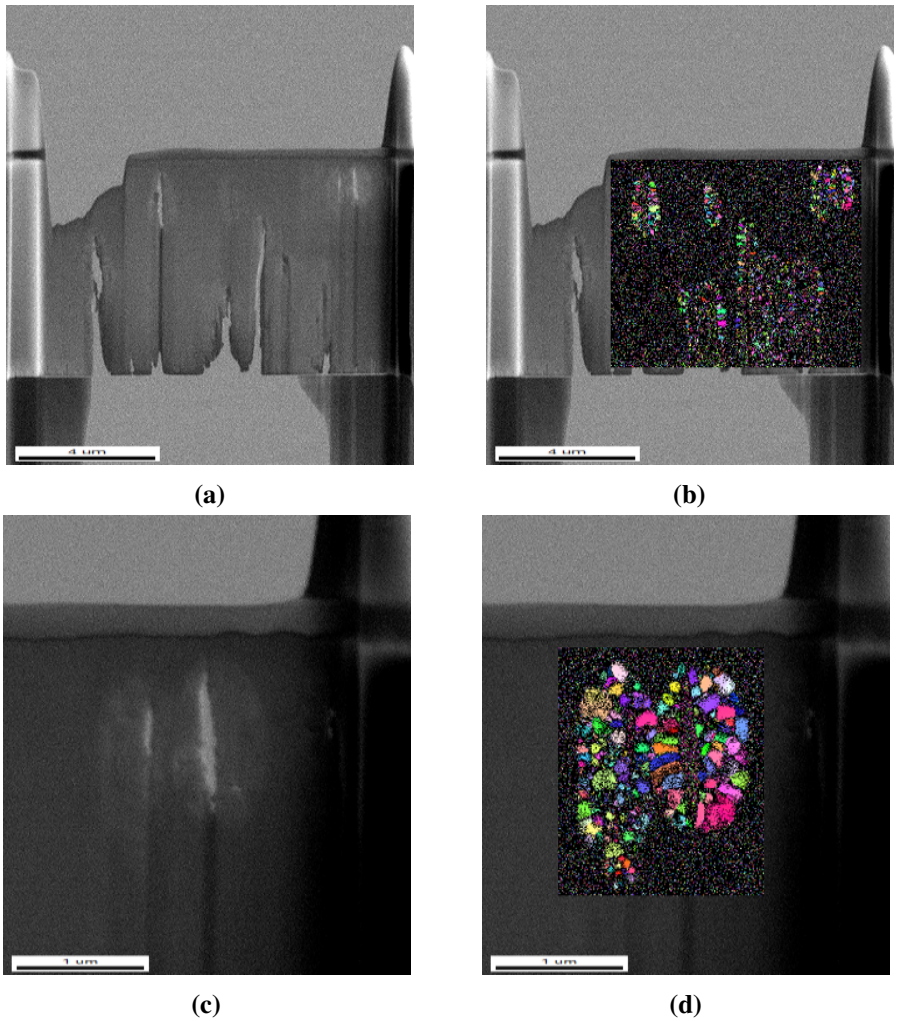

(a) **(b)**

(c) **(d)**

Fig. 3.21 EBSD measurements of a W_2N sample after annealing at 800 $°C$ for 10 hrs(b) and (d) overlaid on the SEM images (a) and (c). The annealing led to cracking of the layer. Relatively big pure-W grains can be seen only around the cracks.

Fig. 3.21 shows the location of the W grains concentrated around the cracks which could explain that cracking in this case.

3.7 Mechanical Properties of WN_x

As an approach to investigate the mechanical properties of the deposited layers, a nanoindentation test is performed, in which the depth-sensing technique is used. Two main mechanical properties can be measured from that technique; the hardness and the elastic modulus. In addition and estimation of the Vikers hardness (HV) is obtained by measuring the indentation size on the surface as shown in Fig.

3.22b. Typical load-displacement curves of W_2N is shown in Fig.3.22a, different indentation loads 50 mN, 100 mN , 150 mN , 200 mN, 250 mN and 500 mN were used.

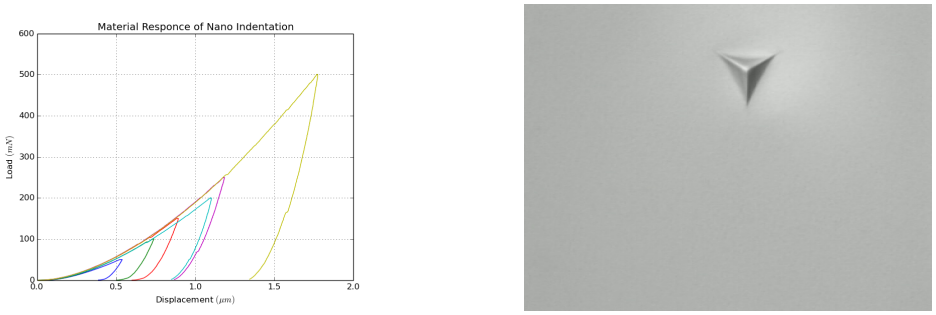

(a) **(b)**

Fig. 3.22 (a) Typical load-displacement curves resulted from measuring the mechanical properties of a W_2N at varying loads. (b) Image of the measurements indent.

To get an idea about the mechanical properties of the WN_x system, three samples (W_2N, WN and WN_2) were measured and compared as a function of their nitrogen concentration. A summary of the mechanical properties is shown in table 3.3.

Table 3.3 A summary of the mechanical properties of WN_x layers with different stoichiometries.

sample	N_2 $\sim at.\%$	HMT115 N/mm^2	HMs N/mm^2	Hit N/mm^2	Eit N/mm^2	HV* N/mm^2
W_2N	33.00	5187.26	5657.66	8245.36	167416.67	761.87
WN	50.00	5349.91	4410.94	7452.78	265100.00	688.64
WN_2	67.00	4473.22	3594.72	7028.07	117698.00	649.39

In the previous table,

HMT115 Martens hardness by Berkovich indenter (115 triangular pyramid indenter)

HMs Martens hardness

Hit Indentation hardness

Eit Indentation modulus (Elastic Modulus or Young's modulus)

HV* Vickers hardness

3.8 Chapter Conclusion

All in all, three different stoichiometric layers, W_2N, WN and WN_2, were found and characterized using different techniques. However for future work, further investigations are needed to optimize

WN and WN_2 layers and produce them with better crystallinity. Many questions are still open, but most importantly how the excess nitrogen can be retained without forming a phase? What are the amorphous structure properties?

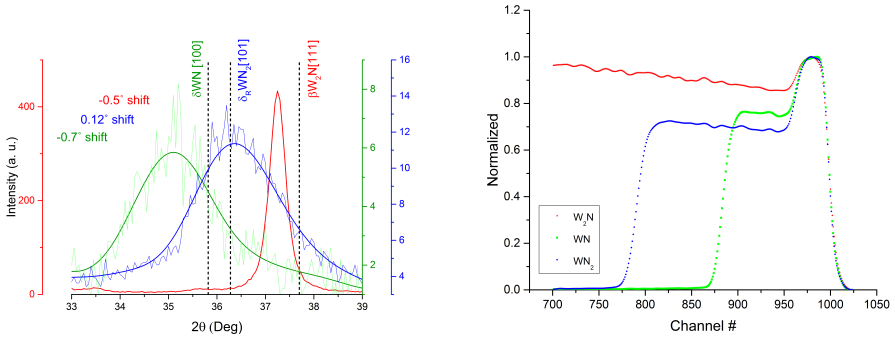

(a) **(b)**

Fig. 3.23 (a) XRD comparison of the three observed stoichiometries shows only the most intense peak. The relative peak shift to the reference values are shown as well as the original spectrum and the smoothed spectrum. (b) RBS spectra (raw data) comparison of the three observed stoichiometries smoothed and normalized to the the identical pure tungsten peak.

In Fig. 3.23a, a comparison of the most intense peaks of three different layers W_2N, WN and WN_2. As it has been mentioned before, the reason of naming the layers after the stoichiometric phases is the closest XRD pattern as well as the nitrogen concentration as measured by RBS. Fig. 3.23b shows the RBS spectra of the three different layers coated with same thin W-coating. A comparison between the raw data, normalized to the pure-W peak, directly shows the significant variation of W amount in the layers which is attributed to the different concentration of nitrogen in the layers. However, in order to confirm that naming, better crystalline layers have to be produced first.

Alongside with fabricating better layers, the investigation of the of existence of the excess N_2 in the layers continues, many hints of retention of Ar in the layers were seen using TDS, EDX and GDOES. Having a look at a high resolution SEM image of a cross section of W_2N sample as shown in Fig. 3.24 can explain the micro-structure of the layer. The grain growth mechanism is still not fully understood, as the grain size is too small, and annealing is not very effective as the layers decompose before the recrystallization temperature. But it is clear from the SEM cross section images and from the TEM results that some porous structure is dominant besides the defects in the films. As the Ar has been seen to be retained without any chemical bonding, that could support the idea of an excess N_2 retention in the layers without chemical bonding as well.

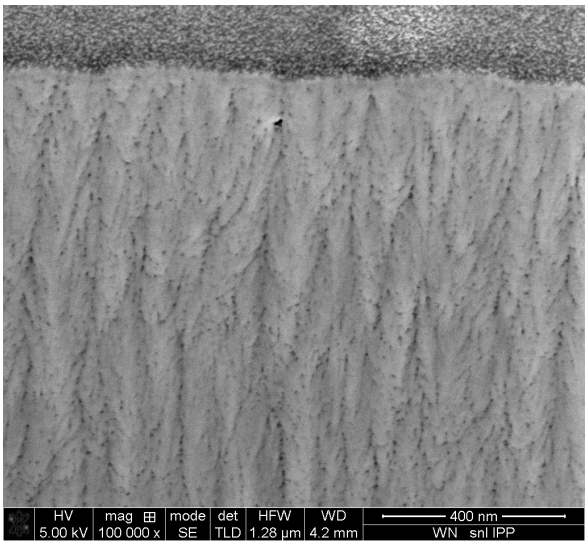

Fig. 3.24 SEM image of a FIB cross section of a W_2N layer which has the best obtained crystallinity, however the porous structure (black dots) is dominating the micro-structure of the layer.

Chapter 4

Optimized and Thermally-Stable Tungsten Nitride

In this chapter there is a discussion about the observations on the layers produced at the optimized conditions obtained through the work which is explained in chapter 3. However, in the work explained in chapter 3, there was no additional substrate heating applied during the deposition and the sample temperature could only rise, due to the sputtering plasma radiation and ion bombardment, to temperatures in the range $\sim 100\ ^{\circ}C$-$200\ ^{\circ}C$. Therefore, this chapter will discuss fabrication of W_2N thin films at temperatures higher than the release temperature, $\gtrsim 450\ ^{\circ}C$, of the nitrogen which is believed to be retained with weak chemical bonding. That's to produce dense, less porous and homogeneous layers.

4.1 Substrate Heating

It has been shown in different areas of thin film fabrication that the temperature of the substrate strongly affects the micro-structure of the growing layers as explained in Sec. 2.1.1. After selecting the best set of deposition parameters based on the results from chapter 3, some depositions were repeated using substrate heating to obtain the optimum deposition temperature. It is assumed that two types of nitrogen exist in the sample, one which is, chemically bonded in a crystal structure and another which is retained or weakly bonded in an amorphous structure. Therefore, a substrate temperature range was chosen to be slightly above the retained N_2 release-temperature as learned from the TDS measurements to be $\sim$ 500-800 $^{\circ}C$. An example of a W_2N-layer deposited at 500 $^{\circ}C$ substrate temperature (optimized) will be discussed and compared with the previous results of the non-optimized layers. Throughout this chapter the produced layers at any conditions except for what is stated in table 4.1 will be referred to as "common layers".

Table 4.1 List of the optimized deposition parameters

Parameter	Value
Ar gas flow	60 *sccm*
N_2 gas flow	15 *sccm*
Chamber pressure	2 *Pa*
Sputtering voltage	420 *V*
Sputtering current	0.82 *A*
Substrate temperature	500 $^{\circ}C$

4.1.1 Micro-Structure Improvement

The layers deposited at temperatures starting from 500 $^{\circ}C$ showed completely different properties compared to without additional heating. In contrast to the common nano-crystalline structure, the so-called needle-structure became dominant. Such grainy structure has an average particle size $\sim$ 150 *nm* which is around 15 times bigger than the 10 *nm* obtained before. Fig 4.1 shows SEM images of the surface morphology of a layer deposited with substrate heating vs. an analogous layer deposited without additional heating.

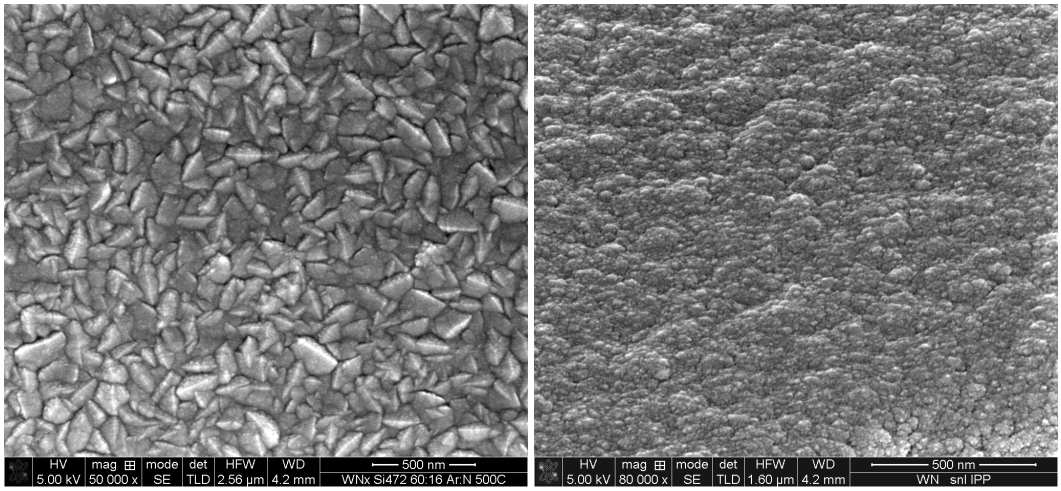

(a) **(b)**

Fig. 4.1 SEM images show a comparison of the surface morphology of (a) an optimized layer shows a grainy structure observed for the first time. (b) The surface morphology of a common layer.

Moreover, FIB cross-section images showed that the layers deposited at elevated temperature had higher density and much lower porosity. Fig. 4.2 shows cross-section images for the same samples as presented in Fig. 4.1. The grain size is much bigger and, most importantly, the porosity and the void structure is dramatically reduced.

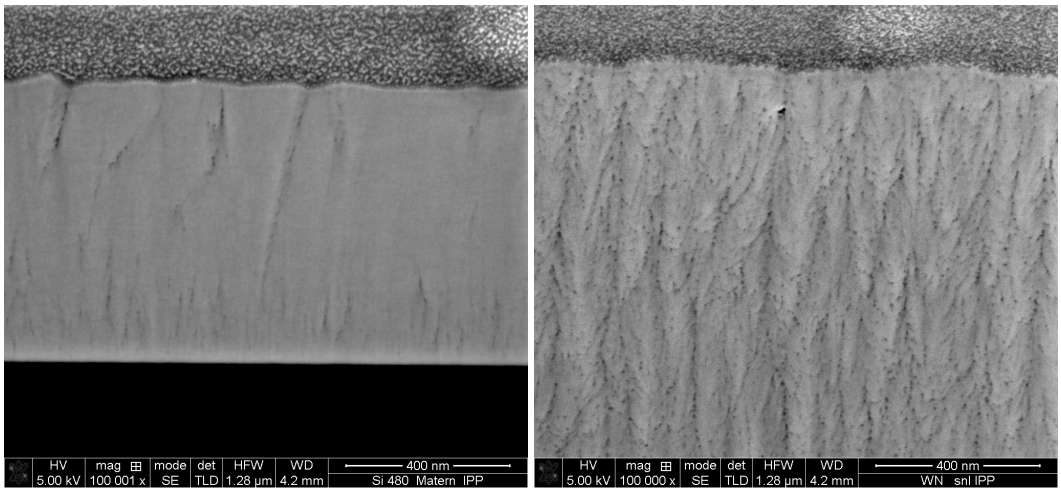

(a) **(b)**

Fig. 4.2 SEM images show a FIB cross-section of the same samples in Fig. 4.1 (a) an optimized layer, (b) a common layer.

4.1.2 Crystal Structure and Orientation

The XRD diffraction measurements showed a strong change in the texture with a major orientation of [200]. In contrast, the common layers had mainly a [111] orientation as shown in Fig. 4.3. In addition, the peaks HWFM of the layer deposited at high temperature is smaller, which maybe due to the increase in the grain size. Furthermore, the peak positions are slightly shifted which can be due to some residual (tensile) stress or some other reasons, like different phase formation, which still need further investigations. The shift corresponds to an increase of $\sim 0.074\ \mathring{A}$ of the lattice parameter, i. e., 1.8 %.

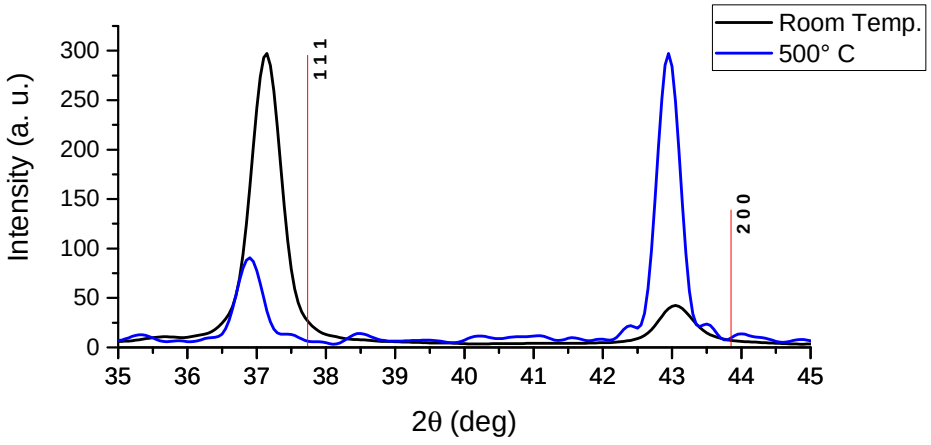

Fig. 4.3 Comparison of XRD patterns showing the most intense peaks (normalized) of an optimized layer (blue line) and a common layer (black line)

4.2 Calculation of WN_x Phases Density

In order to convert the RBS measured thickness in the units of $10^{15}\ Atom/cm^2$ to nm, it is necessary to know the density. Very little is known about the WN_x system and no enough, and reliable, information can be found in the databases. The theoretical values of the stable phases of WN_x are calculated. That is done by calculating the density of the lattice using eq. 4.1.

$$d = \frac{Z \times M}{V \times N_A} \tag{4.1}$$

where d $[g/cm^3]$ is the density, Z is the number of atoms per unit cell, M the atomic mass, V $[cm^3]$ is the lattice volume and N_A is Avogadro's number ($6.0221409 \times 10^{23}\ mol^{-1}$). Additionally, three different compounds of known densities having similar crystal structures as the three stable WN_x phases were calculated for comparison. Table 4.2 shows a summary of the density values for all the calculated materials. The main reason for calculating additional materials density is to estimate the error between the theoretical and experimental density values. The results showed a very good agreement and that means that it is possible to use the calculated values.

Table 4.2 A summary of the calculated densities of the possible WN_x phases compared with calculations of known materials to estimate the error between the theoretical and the estimated experimental values

Name	d Calc. g/cm^3	d Ref. g/cm^3	Lattice str.	a A	c A	Z	M g/mol	V Calc. A^3
W	19.262	19.3	bcc	3.1585	-	2	183.86	31.51
W_2N	18.048	17.8	fcc	4.126	-	2	381.71	70.24
$NaCl$	2.163	2.165	fcc	5.6402	-	4	58.44	179.43
WN	16.043	-	hexagonal	2.893	2.826	1	197.86	20.48
Alunite	2.824	2.74	hexagonal	6.98	17.32	3	414.21	730.76
WN_2	8.897	-	rhombohedral	2.89	16.4	3	211.86	118.62
Calcite	2.711	2.71	rhombohedral	4.9896	17.061	6	100.086	367.84

4.3 Analysis Using RBS

RBS was used to cross-check the W_2N stoichiometry and estimate the porosity in the produced layers and to compare the results to layers deposited without additional heating. As the temperature was chosen above the reported values for the nitrogen-release starting point, it was also important to quantify the nitrogen amounts in these layers and compare their thermal stability to the common layers. The layers were covered with a thin tungsten layer, as explained in Sec. 3.1.2, and measured with 4070 keV $^4He^+$ beam. Fig. 4.10 shows the RBS spectrum of an optimized layer plotted alongside

with the simulation results. The nitrogen content was in the range 37 $atomic\% - 42\ at.\%$ which corresponds to W_2N stoichiometry range 33 $atomic\% - 50\ at.\%$ as reported in [30].

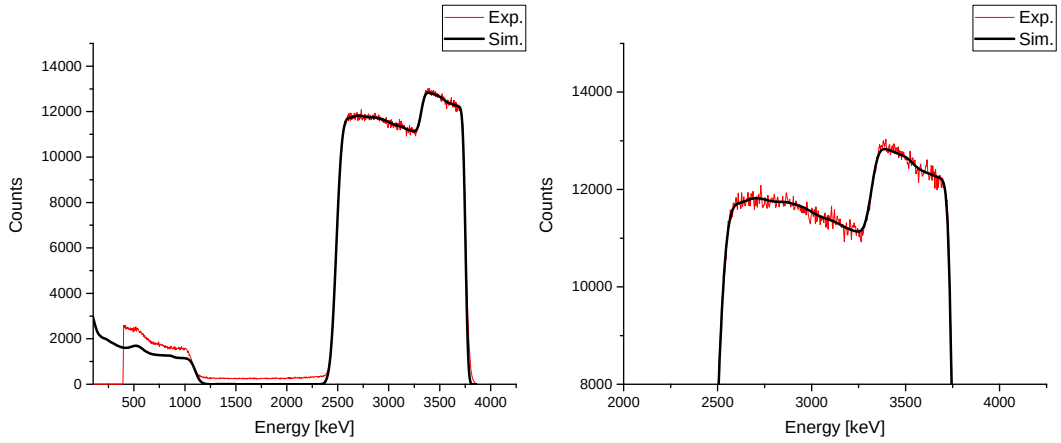

Fig. 4.4 Typical RBS spectra measured using 4070 keV $^4He^+$ of the optimized layer coated with a pure tungsten layer. (a) The simulation (black line) is in a very good agreement with the experimental spectrum (red line) (b) a zoom-in shows some wiggling in the spectrum which can be correlated to a minor inhomogeneity of the layer

4.3.1 Nitrogen Depth Profile

The measured elemental concentrations were not homogeneous through the layers thickness as shown in Fig. 4.4b. Such variation can be due to a temperature increase during the deposition time or a change in the micro structure during the growing of the grains. A nitrogen depth profile was carefully produced and plotted against a the cross-section image of the layer. Regions with a possible higher porosity and voids seemed to retain more nitrogen compared with the denser regions. Fig. 4.5 shows a plot of the depth profile overlaid onto the corresponding cross-section image of the layer.

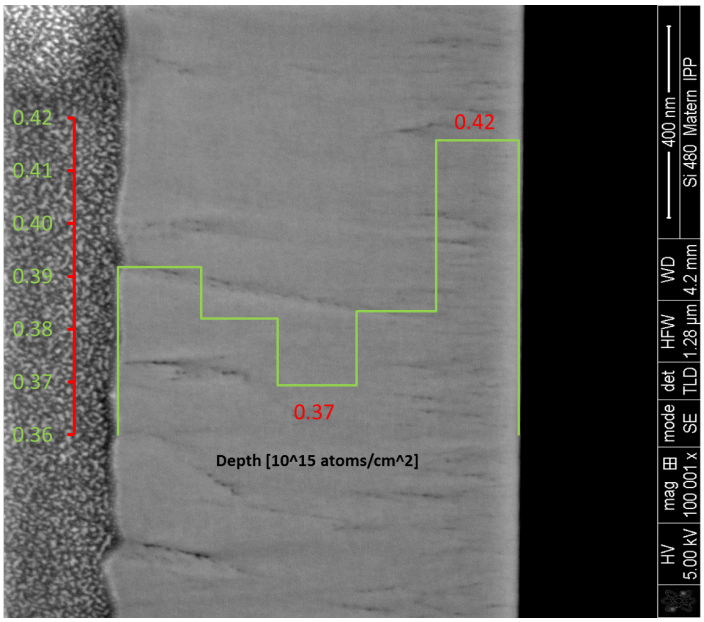

Fig. 4.5 Nitrogen depth profile of an optimized layer overlaid onto a SEM image of a FIB cross-section image of the sample to show the the correlation between visible micro-structure and measured nitrogen content.

4.3.2 N_2 Quantification Using RBS

To accurately determine the total amount of nitrogen in the layer, the depth profile has to be estimated as shown in the previous section. The total nitrogen amount is then calculated by integrating over the whole layer. The obtained value of the areal density of the layer being discussed (optimized layers) was $2.51 \pm 0.17 \times 10^{18}\ Atom/cm^2$

4.4 Porosity Estimation

The porosity is an important parameter to define the quality of the deposited layers, as well as is a key factor for the further deuterium retention experiments. Therefore, an estimation of the porosity of the optimized layers deposited with substrate heating and without heating are compared with an estimation of a pure tungsten film porosity. The porosity is calculated, firstly, by converting the areal density measured by RBS to thickness in *nm* using eq. 4.2 below [44] which is analogous to eq. 2.11. Then, the porosity is estimated as the ratio $(1 - \frac{d_{SEM}}{d_{RBS}}) \times 100\ \%$.

$$D\ [nm] = \frac{1.661 \times 10^{-2} M\ [amu]}{\rho\ [g/cm^3]} \times d\ [10^{15}\ atoms/cm^2] \tag{4.2}$$

Table 4.3 A summary of the calculated porosity using the theoretical density values showing the effect of the substrate temperature during the deposition to reduce the layers porosity

d	M	ρ	D	d_{SEM}	Porosity	Sample
10^{15} atoms$/cm^2$	amu	g/cm^3	nm	nm	%	
8942.00	183.84	19.30	1414	1490	5.0	Pure W
17600.00	127.23	18.00	2066	2700	23.5	W_2N without additional heating
6350.00	127.23	18.00	745	850	12.3	W_2N deposited at 500 $^\circ C$
8150.00	127.23	18.00	956	1010	5.3	W_2N deposited at 700 $^\circ C$

where

d $[10^{15}\ atoms/cm^2]$ is the number of monolayers calculated from the simulations of RBS Measurements.

M is the atomic mass of the layer species or the average atomic mass of compounds such as W_2N is calculated by

$$M_{W_2N} = (2M_W + M_N)/3 = (2 * 183.84 + 14)/3 = 127.23$$

ρ the layer material density for W_2N which is taken from [66].

D is the converted areal density to nm.

d_{SEM} is the thickness of the layer-FIB-cross-section measured by SEM.

Table 4.3 shows a summary of some measured values and the corresponding estimated porosity. However, the stopping power for the $^4He^+$ ions is a function of the deposited layer itself and calculating the absolute value it is not straight forward. Despite that fact, it can be seen that the optimized layers have much less porosity which is comparable with deposited pure tungsten.

4.5 Thermal Stability of the Layers

One of the most important goals of this thesis was to produce thermally more-stable layers. Such optimized layers do successfully fulfill that goal. Fig. 4.6 shows the desorption behavior of several gas species, mainly nitrogen, from an optimized layer as a function of time and temperature. In the nitrogen release signal (blue line) a sharp peak can be seen around 1050 $^\circ C$ which is related to the surface damage and a sudden release of the weakly-bound-nitrogen. Another possibility is, it can be due to a change in the heating ramp which the layer can be very sensitive to.

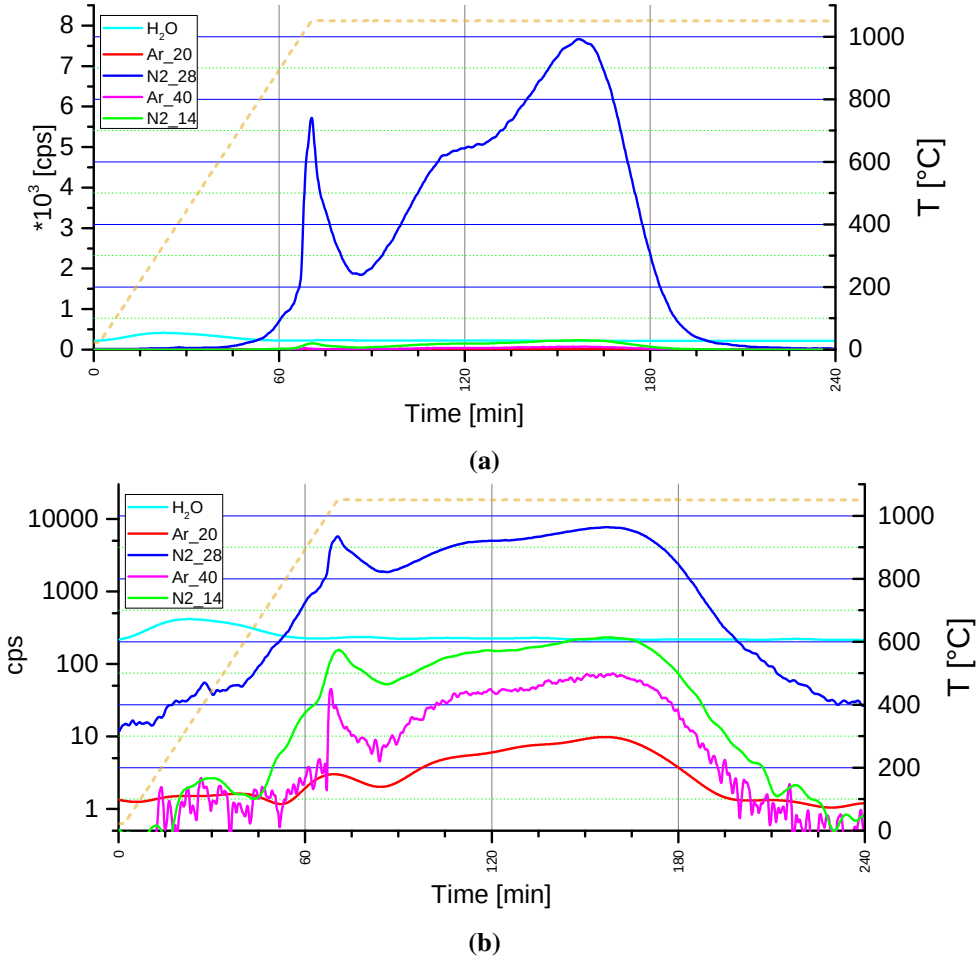

Fig. 4.6 Thermal desorption spectra (TDS) of the recorded masses to mainly show the thermal behavior of the nitrogen release (blue line) as a function of the oven temperature (yellow dashed-line). (a) On a linear scale. (b) On a log scale to show the other existing masses with trace amounts.

Furthermore, two desorption peaks appear while the temperature was constant at 1050 $^{\circ}C$ which requires further investigations to be properly interpreted. Fig. 4.7 shows a four-Gaussian-fitting to the curve to easily recognize the peaks.

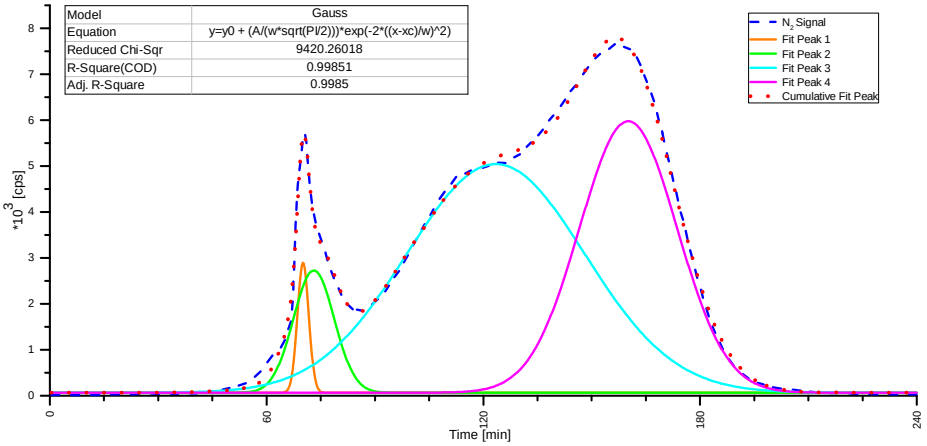

Fig. 4.7 The N_2- QMS signal as a function of time as shown in Fig. 4.6a. A four-Gaussian-peaks fit is applied to present the possible peak-shapes and position, however, further investigations are needed to comprehend the reason behind such slow decomposition process.

In contrast to the layers which are commonly deposited, the optimized layers showed higher thermal stability up to 1000 $°C$. Fig. 4.8 shows a comparison between an optimized layer and a common layer.

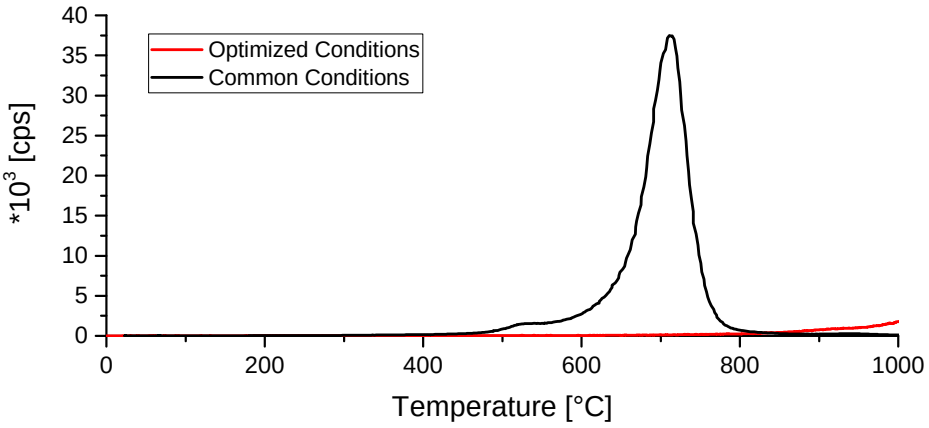

Fig. 4.8 TDS N_2 release signal as a function of temperature for a comparison between an optimized layer (red line) and a common layer (black line).

4.5.1 N_2 Quantification Using TDS

As the cutting of the substrates in most cases results in specimens with slightly bigger dimensions than the estimated ones, the average surface area is estimated by weighing eight samples which gives a value of $1.0511 \pm 0.0121\ cm^2$. Furthermore, the cathode has an inclination angle of 25° to the substrate, the deposition rate on the edges should be taken into account. The substrate has estimated dimensions of $10 \times 10\ mm^2$ and a thickness of $400 \pm 25\ \mu m$. The edge effective area could

be estimated by

$$\frac{\cos(25^\circ)}{\sin(25^\circ)} \times (400\ \mu m \times 10^{-4} \times \sqrt{1.0511}) \times 4 \approx 0.0343 \pm 0.0007 cm^2$$

the total desorption area is then $1.08511 \pm 0.0133\ cm^2$.

The Integral of the N_2 signal (shown in Fig. 4.6a) is $3.45 \times 10^7\ counts$. Converting this value to the number of released N atoms is done using the calibration factor of the QMS which is $4.0 \pm 0.37 \times 10^{10}\ [N/count]$ for 0.01 mA emission current. The total number of desorbed N atoms is then

$$N_{TDS} \approx 3.45 \times 10^7 \times 4.0 * 10^{10} \times 2 \approx 2.5 \pm 0.27 \times 10^{18}\ N\text{-Atom} \tag{4.3}$$

4.6 An Approach to Understand the Desorption Behavior

It is still not clear how WN_x layers decompose, as well as, why annealing doesn't have a significant effect on such layers. Therefore, producing thermally more-stable layers will allow deeper understanding of the decomposition behavior of such layers. The nitrogen release was slow and lasted for $\sim 4\ hrs$. Therefore, it will be easier to deconvolute the multiple possible factors, that is to have a closer look and try to comprehend how those layers decompose. An experiment was performed in order to correlate the effects on the layer micro-structure and the first part of the desorption signal (first desorption peak). An identical sample was heated until the first peak is obtained (before the red dashed line in Fig. 4.9) then the temperature was slowly set back to 900 $^\circ C$ by a rate of 15 $^\circ C/min$ and was held for 30 min at 900 $^\circ C$, then it was ramped down to avoid the layer damage due to a sudden cooling.

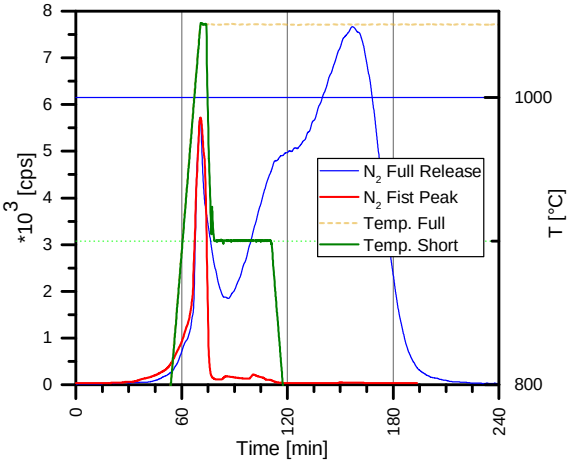

Fig. 4.9 Two TDS signals of nitrogen release of the optimized correspond to two heating profiles; full desorption heating profile (yellow line) and the other is heating until the first peak is obtained then the temperature was slowly set back to 900 $^\circ C$ by a rate of 15 $^\circ C/min$ and was held for 30 min at 900 $^\circ C$, then it was ramped down. The nitrogen signal shows a sudden drop when the temperature was decreased.

There are multiple factors that can contribute to such decomposition behavior, e.g., the expansion coefficient mismatch between the layer and the substrate, the thickness of the layer and also the retained gas in the defects and between the grains. Furthermore, the interaction between the substrate (silicon) and the tungsten in the layers to form tungsten silicide. Such interaction has a formation temperature in the range 850 $°C$-1100 $°C$ [67].

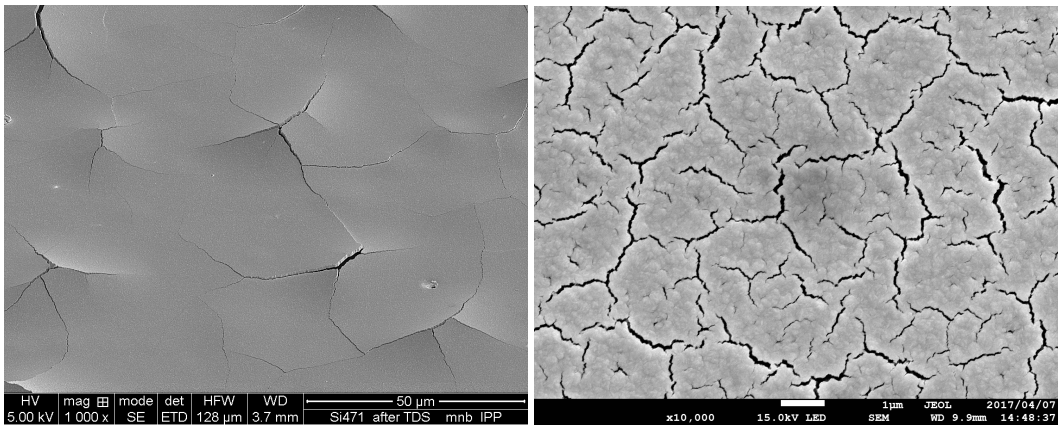

(a) **(b)**

Fig. 4.10 SEM images of the surface morphology after heat treatment as a comparison between an optimized and a common layer. (a) an optimized layer heated up to 1050 $°C$ with scale 10x smaller to show the overall effect which showed expansion. (b) a common layer annealed at 800 $°C$ which showed contraction.

A brief discussion will cover the main aspects of the decomposition. The completely different behavior of the optimized layers can simplify the problem. As mention earlier, to get an idea about the first peak, Fig. 4.10a shows the effect on the micro structure. Such heat treatment led to surface cracking due to compression. However such cracking is more likely to be due to the mismatch between the WN_x layer and the substrate. Fig. 4.10 shows SEM images for a comparison between the mentioned optimized layer and the common layer which was annealed in vacuum just at 800 $°C$ for 8 hours. The common layer showed a loss in the volume due to the nitrogen release which has been shown earlier in sec. 3.6. In contrast, in case of the optimized layer, the main contribution seems to be due to the thermal expansion coefficient mismatch until the sample reaches 1050 $°C$ which will be shown in the next section.

4.6.1 Thermal Expansion Coefficient of WN_x

An idea about the thermal expansion coefficients of W, $\alpha(t)_W$, and WN_x, $\alpha(t)_{WN_x}$, can be taken from Fig. 4.11a [68]. The average value of the thermal coefficient of Si, $\alpha(t)_{Si}$, up to 1050 $°C$ is 3.92×10^{-6} $°C^{-1}$ [69]. In addition, from the interpolation of the curves in Fig. 4.11a, after a reconstruction of the image, up to 1050 $°C$ as shown by the doted lines in Fig. 4.11b, the average value of $\alpha(t)_{WN_x}$ will be $\sim 7.6 \times 10^{-6}$ $°C^{-1}$ which makes a big mismatch with Si and can result in a

delamination of the layer. Moreover, the average value of $\alpha(t)_W$ is $\sim 4.98 \times 10^{-6}\ ^{\circ}C^{-1}$. In addition, $\alpha(t)_{graphite}$ is $\sim 1.0 \times 10^{-6}\ ^{\circ}C^{-1}$ [70]. It is necessary to choose suitable substrate to investigate such behavior; therefore more investigation is needed to choose a proper substrate and exclude the effect of the thermal expansion coefficients mismatch.

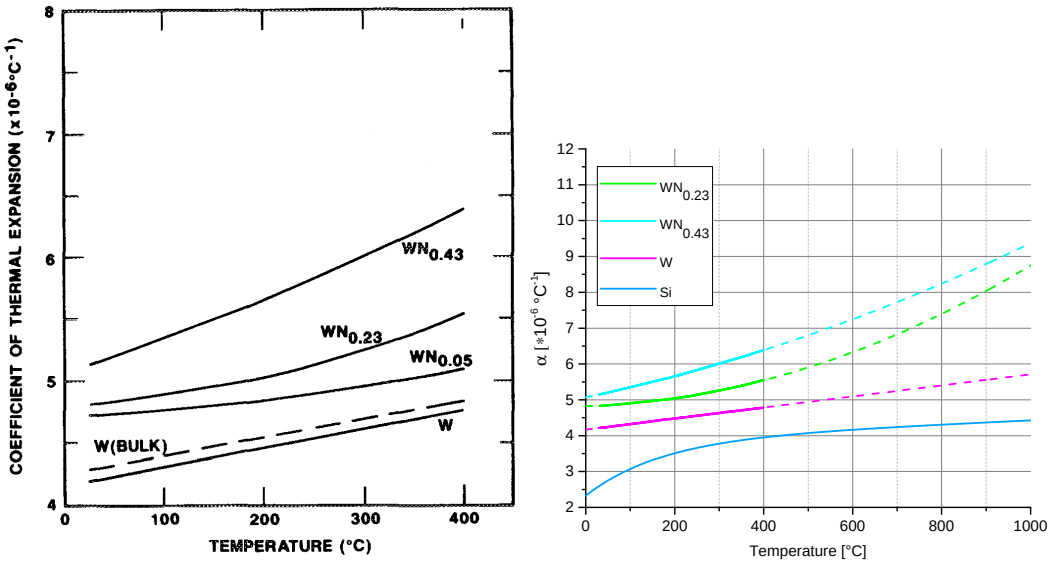

(a) **(b)**

Fig. 4.11 Thermal linear expansion coefficients (a) WN_x and W up to 400 $^{\circ}C$ from [68] the closest stoichiometry to the produced layer is $WN_{0.43}$. (b) A reconstruction of the the first graph with extrapolation up to 1000 $^{\circ}C$ with comparison to the *Si* substrate. The reconstruction was done digitally using then the lines were fitted by polynomial functions then were extrapolated.

Using these values in addition to the mechanical properties values obtained in Sec.3.7, an estimation of the thermal stress σ_{th} can be made using eq. 4.4 [71].

$$\begin{aligned} \sigma_{th}\ [GPa] &= \Delta\alpha\Delta T \frac{E}{1-\nu} \times 10^{-6} \\ &= 3.15 \times 10^{-6} \times 500 \times \frac{167.42 \times 10^{6}}{1-0.29} \times 10^{-6} = 0.37\ GPa \end{aligned} \tag{4.4}$$

where $\Delta\alpha$ is the difference between W_2N and *Si* linear thermal expansion coefficients, E is Young's modulus of the layer and ν is its Poisson's ratio. Calculating the changes in area compared to original area $\frac{\Delta A}{A_0}$ due to thermal expansion using eq. 4.5 gives a ratio of

$$\frac{\Delta A}{A_0} = 2\Delta\alpha\Delta T = 0.006611 \tag{4.5}$$

Fig. 4.12 shows 3D-measurements by confocal laser microscope. Fig. 4.12a shows the optimized layer surface after heating it up to 1050 $°C$ then the temperature was slowly set back to 900 $°C$ by a rate of 15 $°C/min$ and was held for 30 min at 900 $°C$, then it was ramped down a rate of 15 $°C/min$. The evaluation is done using the Gwyddion software [72]. To get an idea about the dimensions of the topology a line-profile (Fig. 4.12c) is taken as shown in Fig.4.12b.

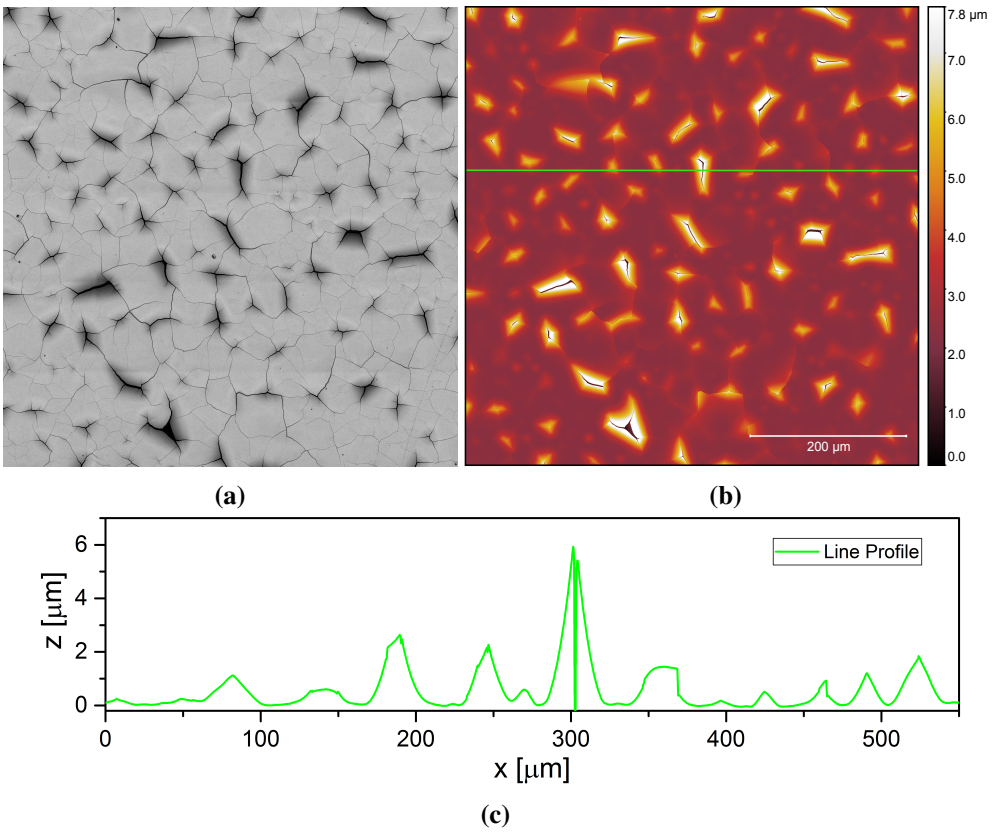

Fig. 4.12 Confocal laser microscope image constructed by stitching and merging of multiple images. (a) Intensity image reconstructed from multiple focus levels showing, with high resolution, the damage due to thermal stresses. (b) Height image (elevation image) shows the surface topology in a color map. (c) Line profile as shown in Fig. 4.12b (green line). This figure can show that the damage of the layers was mainly due to thermal expansion of the layer and no volume loss (shrinking) as it has been believed.

4.6.2 Substrate Material Effect

Once the sample reaches the temperature of 1050 $°C$, it is still not clear what happens exactly. At this temperature, as mentioned earlier the *Si-W* interaction can dominate, however, further investigations are needed. Fig. 4.13 shows the phase diagram of *W-N* and *W-Si* systems. From the graph of *W-N* system a huge disagreement can be seen between the phase diagram thermal stability and reported value of the thermal stability. The thermal stability of W_2N (γ) is thermodynamically predicted to be up to 1874 $°C$, while the reported value for the decomposition is $\sim$ 800 $°C$ [73].

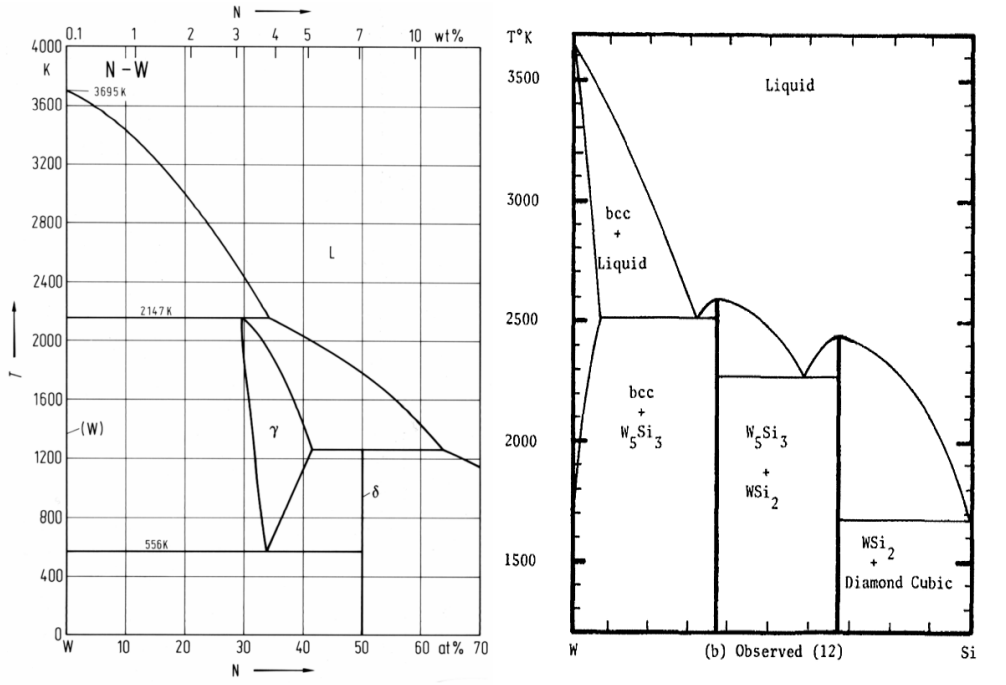

(a) **(b)**

Fig. 4.13 Phase diagram of (a) *W*-*N* system showing the γ phase (W_2N) stability region. (b) The *W*-*Si* system showing the possible phases which can exist $\sim 950\ ^{\circ}C$.

Fig. 4.14 shows the effect of the substrate material on the decomposition behavior measured by TDS. This figure shows the optimized layer deposited on both *Si* and *C* in the same deposition run. That can assure that both layers were deposited at identical conditions. The layer on *Si* was annealed at 1050 $^{\circ}C$ for 3 *hrs*. The layer on carbon was annealed at 950 $^{\circ}C$ for 40 *hrs*. From the graph it can be seen that the layer which is deposited on *C* has a sharp release-peak of *N* compared with the other layer. Such observation can support the assumption that the layers do not decompose, however, the substrate material diffuses into the film and substitutes the nitrogen which, in turn, leads to nitrogen release. The quick release of N_2 can be due to the fact that *C* has higher diffusivity than *Si*.

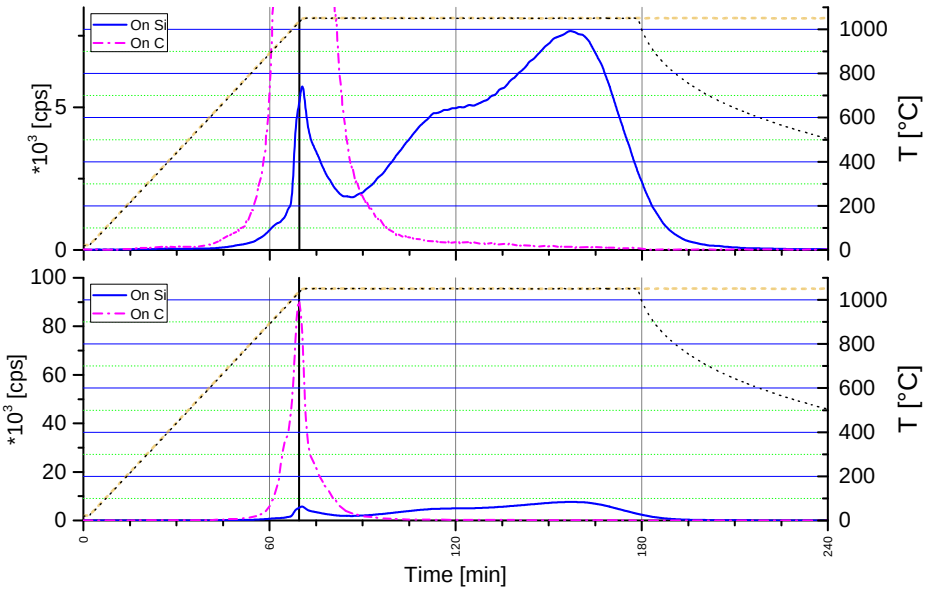

Fig. 4.14 TDS comparison of the optimized layer deposited on *Si* and on *C*. The graph shows the N_2 signal as a function of time, as well as, the oven temperature as a function of time. It can be seen that the layer which is deposited on *C* has a sharp release peak in comparison with the release peak from the layer which is deposited on *Si*.

For more understanding of the effect of heat treatment on the layers, further experiments were performed and were followed by RBS measurements to investigate the changes in layers composition. Fig. 4.15 shows the effect of the substrate material, after heat treatment, measured by RBS. It can be seen that in the case of *Si* interdiffusion between *W* and *Si* occurred. That can be inferred from the appearance of *Si* in the whole layer up to the surface and, consequently, the total disappearance of the *N* from the layer. Although an increase in the peak-width of the *W* peak and a change in the peak height can be seen, the integral of both peaks remains almost the same. That is due to the formation of WSi_2 based on the simulations (not shown here) of the spectrum after annealing. On the other hand, after heat treatment, the layer which is deposited on *C* showed a full substitution of *N* with *C*. That can be seen from the shift on the *C*-peak position which corresponds to the existence of *C* in the whole *W* layer up to the surface.

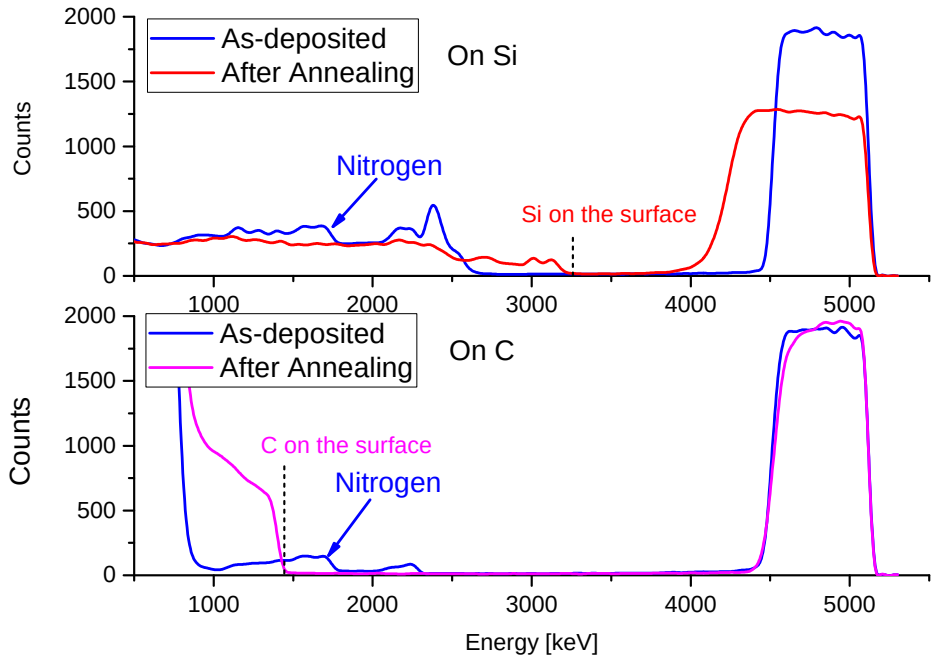

Fig. 4.15 RBS spectra (smoothed) of the optimized layer deposited on *Si* and *C* substrates. Annealing above 900 $^{\circ}C$ showed diffusion of the substrate elements into the film. The layer on *Si* was annealed at 1050 $^{\circ}C$ for 3 *hrs*. the layer on carbon was annealed at 950 $^{\circ}C$ for 40 *hrs*.

4.6.3 Heat Treatment Effects on the Micro-Structure

A closer look to the micro-structure after such experiment (4.6) is shown in Fig. 4.16a. It is interesting to see the micro scale loss in volume (black dots) due to the slightly excess nitrogen. However, no big change in the overall micro-structure is seen. Therefore, the idea about the thermal stability of such layers should be reconsidered. It has been reported in multiple literature that, W_2N, starts to decompose $\sim$ 500 $^{\circ}C$ [25] and it is fully decomposed by $\sim$ 900 $^{\circ}C$ [73]. However, for the optimized layers which are discussed in this chapter, the decomposition temperature is $\sim$ 950 $^{\circ}C$.

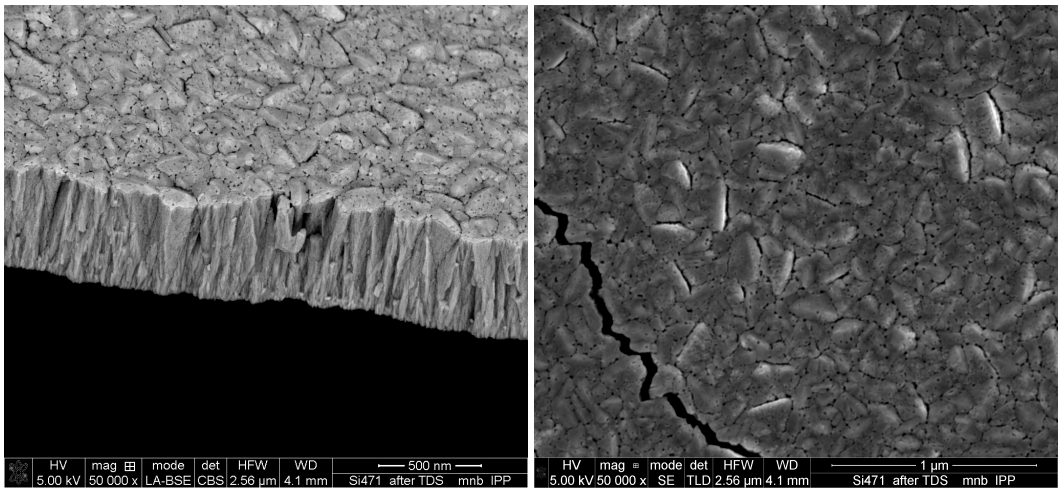

(a) **(b)**

Fig. 4.16 High resolution SEM tilted-image (digitally sharpened) of a broken edge to show the micro voids (black dots) appeared on the surface after heating it up to 1050 $^{\circ}C$ then the temperature was slowly set back to 900 $^{\circ}C$ by a rate of 15 $^{\circ}C/min$ and was held for 30 min at 900 $^{\circ}C$, then it was ramped down a rate of 15 $^{\circ}C/min$. (b) SEM image (normal view) to get a closer look to the changes on the surface morphology (crack and volume loss).

4.7 Residual Stress Evaluation

The residual stress in the deposited layers was a major problem at the beginning of this work. A final assessment of the residual stress in the optimized layers is needed. The used method is to measure the change of the specimen curvature pre- and post deposition. The surface curvature was measured using Bruker Dektak Stylus Profilometer. Fig 4.17b shows the curvatures (leveled) of the silicon and W_2N. In this case the substrate curvature is not negligible. A 5th order polynomial fit is performed followed by obtaining the first and second order derivatives y' and y''. The radius of curvature $R(x)$ at any point can be calculated using as

$$R(x) = \frac{(1+y'^2)^{\frac{3}{2}}}{y''} \tag{4.6}$$

To calculate the residual stress in the film Stoney's equation was used [74].

$$\sigma_R = \frac{1}{6}\left(\frac{1}{R_{W_2N} - \frac{1}{R}_{Si}}\right)\frac{Y}{1-\nu}\frac{d_{Si}^2}{d_{W_2N}} \tag{4.7}$$

where R_{Si} is the substrate radius of curvature, R_{W_2N} is the specimen radius of curvature, Y is the substrate Young's modulus, ν is Poisson ratio, d_{Si} is the substrate thickness and d_{W_2N} is the film

thickness. For this measurements $\left(\frac{Y}{1-\nu}\right)$ is taken to be 181 *GPa* and the substrate thickness is $400 \pm 25\ \mu m$.

Fig.4.17a shows the residual stress as a function of the horizontal distance. The measurements was performed in two perpendicular directions x and y on the surface. The average value of the residual stress in the layer is $\approx\ 0.35 \pm 0.04$ *GPa* which is a tensile stress. This value is considered a low value for a PVD-fabricated thin film.

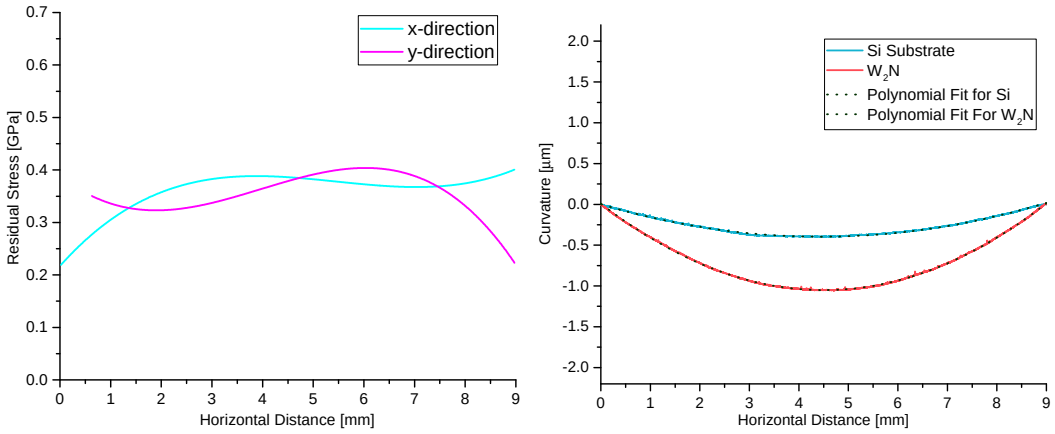

(a) **(b)**

Fig. 4.17 (a) The residual stress in the optimized layer as a function of the horizontal distance of the substrate measured in two perpendicular directions. (b) The curvature of the substrate as a function of the horizontal distance of both the silicon substrate before deposition (light blue) and with the film after deposition (red line).

Since the layers were deposited at elevated temperatures, a possible source of the residual stress is again the difference between the expansion coefficients $\Delta\alpha$, as discussed in sec. 4.6.1. However in this case, the temperature difference ΔT is taken to be the difference during and after deposition which is 500 $^{\circ}C$. Substituting in eq. 4.8 gives $\sigma_{th} \approx 0.29 \pm 0.014$ *GPa* which is considerd a low value in comparison with the reported values of the common layers [75]. This value is also a tensile stress, which means a big portion of the residual stress is due to the thermal expansion coefficients mismatch [71].

$$\sigma_{th} = \Delta\alpha\Delta T\left(\frac{Y}{1-\nu}\right) \tag{4.8}$$

4.8 Annealing Effect

In order to take the investigations of the thermal stability of the optimized layers a step further, annealing this layer at 900 $^{\circ}C$ for 50 *hr* was performed. At this temperature it is believed that no W-Si interaction takes place. As mentioned, at before this temperature it was claimed in multiple literature that WN_x is fully decomposed [25, 73]. Fig. 4.18 show the RBS spectra of the optimized layer after

two different heat treatments; two samples after annealing at 900 $^{\circ}C$ for 50 hr, one sample after heating it up to 1050 $^{\circ}C$ then the temperature was slowly set back to 900 $^{\circ}C$ by a rate of 15 $^{\circ}C/min$ and was held for 30 min at 900 $^{\circ}C$, then it was ramped down a rate of 15 $^{\circ}C/min$. The spectra in the figure where smoothed to reduce the noise somehow. The change in width of the W-peak, can also be attributed to some micro-structure changes, although a slight change can be noticed, it cannot be evaluated as it beyond the resolution limit.

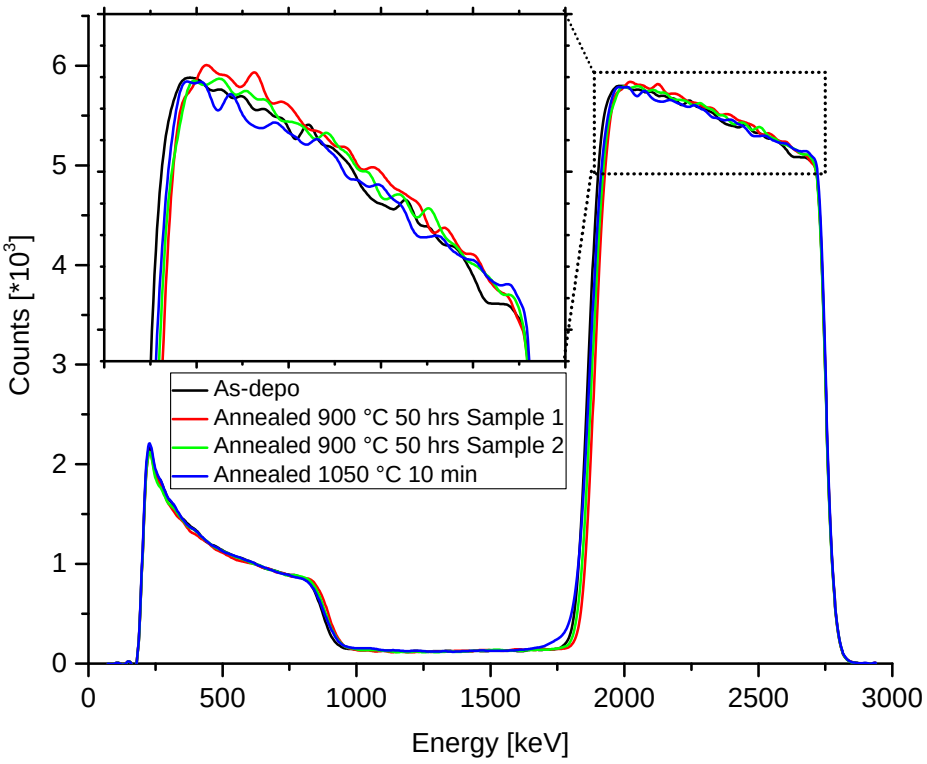

Fig. 4.18 RBS spectra (smoothed) of the optimized layer as-deposited, after annealing at 900 $^{\circ}C$ for 50 hr and after annealing at 1050 $^{\circ}C$ for 5 min. It can be seen that no detectable loss of nitrogen has been recorded.

To have a closer look to the effect of annealing at 900 $^{\circ}C$ for 50 hr on the residual stress and also on the texture, Fig. 4.19 shows the change in the peak positions after annealing compared with the as-deposited layer. As it has been mentioned before (Sec. 4.1.2) the texture ([200]) was dominating and has not been reported in previous literature. The heat treatment did not show any change on the texture back to [111]-texture, however, a further increase of [200]-texture as shown in Fig.4.20.

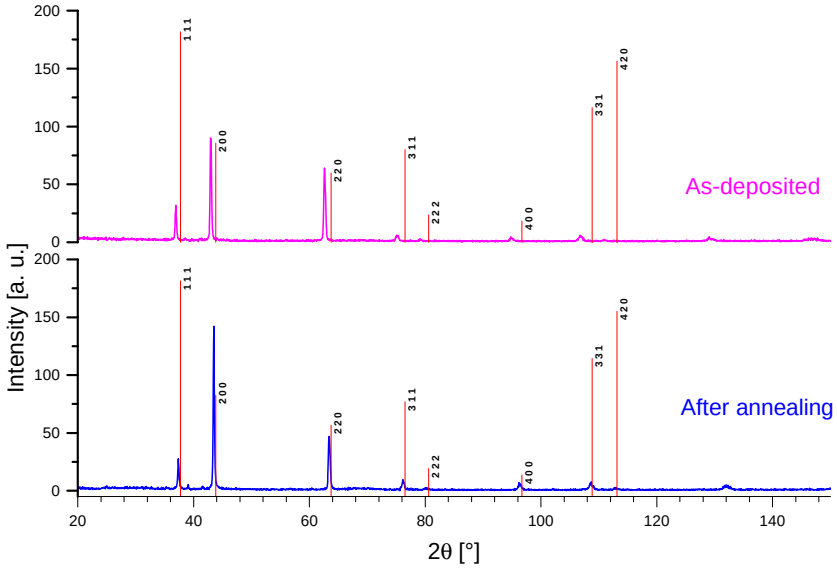

(a)

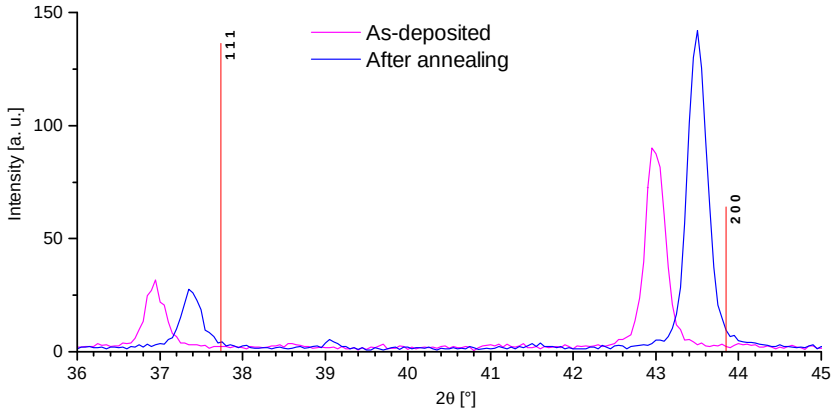

(b)

Fig. 4.19 (a) The effect of annealing at 900 $^{\circ}C$ for 50 *hr* on the micro-structure showed a shift in the peak positions towards the reference value. That means that a big portion of the residual stress has been relieved. (b) a zoom-in to the two main peaks.

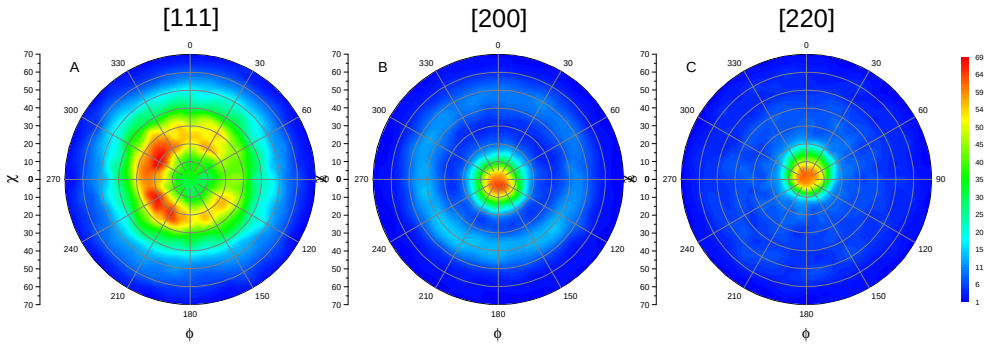

(a) As-deposited

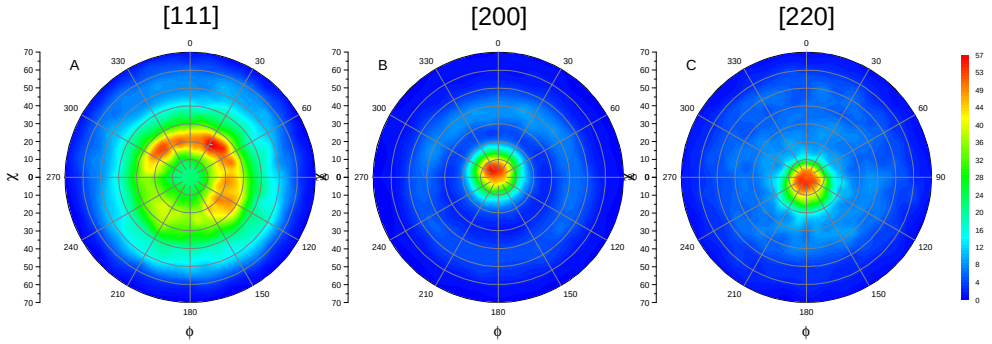

(b) Annealed

Fig. 4.20 Annealing at 900 °*C* for 50 *hr* did not show a noticeable effect on the texture of the optimized layer. (a) as deposited (b) after annealing.

4.8.1 Heating Ramp Effect

Fig. 4.21 shows the effect of the heating ramp on the macro structure of the layers. It can be seen that heating the optimized layer up to 1050 °*C* then the temperature was slowly set back to 900 °*C* by a rate of 15 °C/min and was held for 30 *min* at 900 °*C*, then it was ramped down a rate of 15 °C/min showed a lot of cracks. However, heating it up to 900 °*C* for 50 *hrs* with heating and cooling rate of 1 °C/min showed much less cracks. Therefore an optimum heating ramp has to be found and used to prevent the cracking due to the rapid heating and cooling.

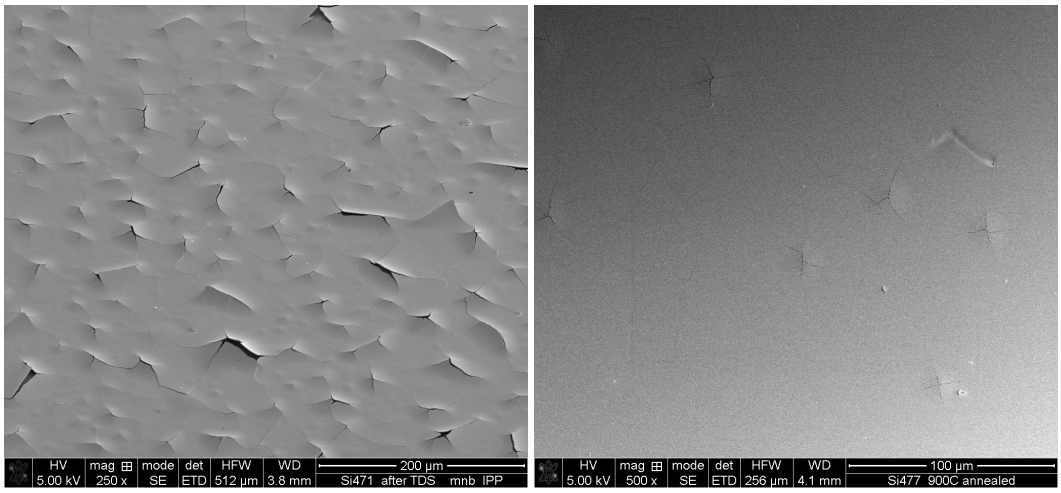

(a) **(b)**

Fig. 4.21 SEM images the optimized layer after two different heat treatments. (a)The optimized layer after heating it up to 1050 $^{\circ}C$ then the temperature was slowly set back to 900 $^{\circ}C$ by a rate of 15 $^{\circ}C/min$ and was held for 30 *min* at 900 $^{\circ}C$, then it was ramped down a rate of 15 $^{\circ}C/min$. This shows much more cracks which can be attributed to the heating ramp. (b) Annealed at 900 $^{\circ}C$ for 50 *hrs* with heating and cooling rate of 1 $^{\circ}C/min$. The scale of this image is two times bigger to show more details. This show minor cracks which can support the idea that the slow ramp can help release the stress without causing a big damage to the layers.

4.9 Chapter Summary

In this chapter it was shown that it is possible to produce thermally stable tungsten nitride (W_2N) thin films by optimizing the deposition conditions. The properties of the novel layers were shown and examined mainly by XRD, RBS and TDS. The optimized layers showed thermal stability up to 1000 $^{\circ}C$ and survived annealing at 900 $^{\circ}C$ for 50 *hr* without any noticeable nitrogen loss. The release of nitrogen at further temperature was shown to be due to diffusion of the substrate material into the film and chemical reaction results in formation of compounds like WSi_2 and WC.

Chapter 5

Deuterium Retention in Tungsten Nitride

In this chapter an investigation of the hydrogen isotopes (deuterium) retention in WN_x will be carried out. Since in a fusion reactor the fuel is composed of hydrogen isotopes, it is necessary to investigate the behavior of WN_x layers in such environment. A short background regarding the loading device as well as the used nuclear reaction method will be briefly presented. The diffusion depth in the layers and the release behavior of D from WN_x as a function of temperature will be discussed. Afterwards, the quantification using NRA and TDS will be showed and compared. Moreover a short overview on the effects induced on micro-structure will also be shown.

5.1 Deuterium Implantation via Plasma Exposure

In the scope of this thesis, it is important to probe the behavior of WN_x layers in response to hydrogen isotopes. Moreover, it is interesting to compare in this respect the optimized layers, which showed remarkable enhancements on the thermal stability and the micro-structure, to the commonly produced layers. For that purpose, deuterium loading is carried out for WN_x samples via plasma exposure. The used device is called "PlaQ", a detailed describtion is found here [76]. The device uses a microwave source to heat a deuterium plasma via electron cyclotron resonance (ECR), Fig. 5.1 shows a sketch of the device.

The plasma parameters were tuned to provide the desired ion energy and fluence. For this particular experiment, the samples exposure was performed at elevated substrate temperature of 600 K, as it was shown by [77] that deuterium diffusion in WN_x layers at room temperature is negligible. The used parameters are: 1 Pa D_2 pressure, -200 V DC substrate bias, corresponding ion energy of 72 eV/D, implantation time of 18 hr and that results in a fluence of 6.0×10^{24} D/m^2.

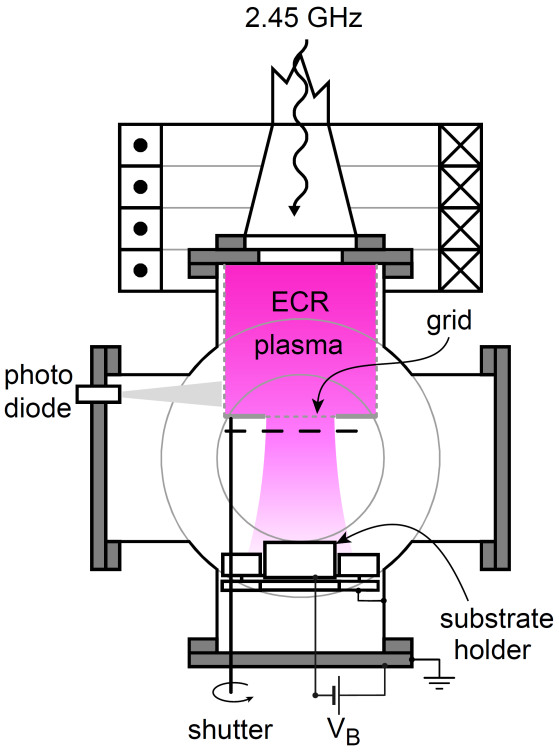

Fig. 5.1 Sketch of the plasma loading device "PlaQ" [76]

5.2 Deuterium Analysis Using NRA

In order to investigate the deuterium diffusion and retention in the loaded WN_x layers, the NRA method was used. In such measurements, a $^3He^+$ ion beam was used to probe the specimen resulting in the nuclear reactions shown in eq. 5.1.

$$D(^3He, p)^4He \tag{5.1a}$$

and

$$D(^3He, \alpha)p \tag{5.1b}$$

This reaction has a cross section as shown in Fig. 5.2 with a resonance peak at 690 keV. Unfortunately, this resonance is too wide to provide good depth resolution in the nm range which is the case of deuterium diffusion in WN_x.

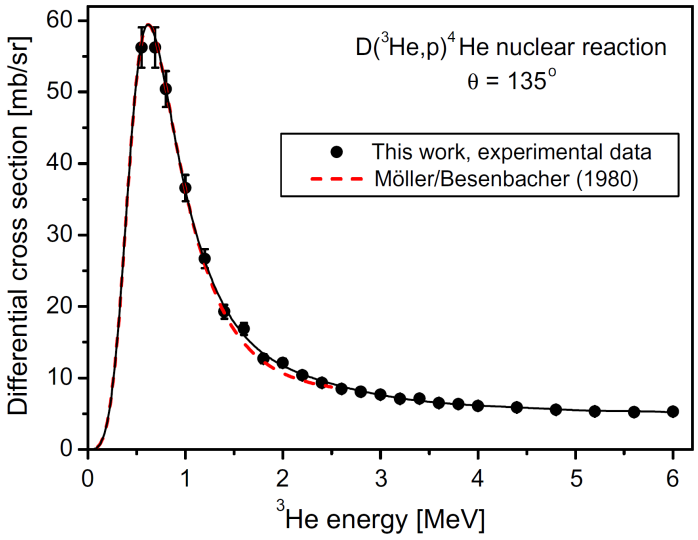

Fig. 5.2 the differential cross section of the used nuclear reaction ($D(^3He,p)^4He$) [78]

The produced protons are collected with a detector at scattering angle of 135° with a solid angle of 77.5 ± 3.0 *msr*. The alpha particles are collected by another detector at angle of 102° which has a solid angle of 7.65 ± 0.26 *msr*. The resulting spectrum is then simulated using SIMNRA software as explained earlier in Sec.2.2.2.1. As an example for the proton spectrum and the simulation, Fig. 5.3 shows the experimental data and the simulation of the proton (a) and alpha (b) signals of two different W_2N layers. The first W_2N layer was deposited at elevated substrate temperature of $700°C$ and the other was deposited without additional substrate heating (common layers).

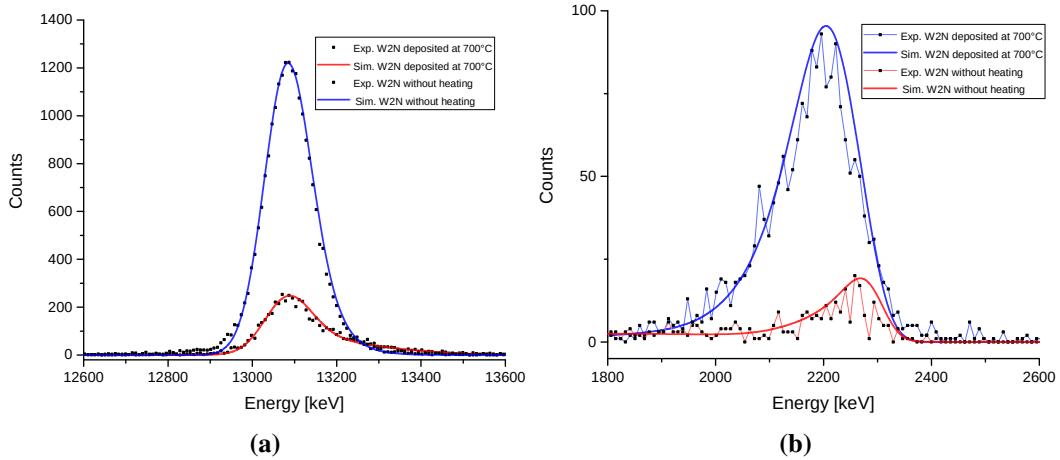

Fig. 5.3 A comparison between the deuterium amount (the peak integral) in the optimized layer (red line) and the common layer (blue line) measured by the NRA products. (a) The proton signal. (b) the alpha particle signal.

The corresponding depth profile from the previous two signals was done separately. The alpha particles signal has a better depth resolution, however, down to a very shallow depth. The stopping of the alpha particles in the layers if very high compared with the protons. On the other hand, the proton signal carries information about the total deuterium amount in the layer. Therefore, a more detailed information can be obtained by combining both spectra.

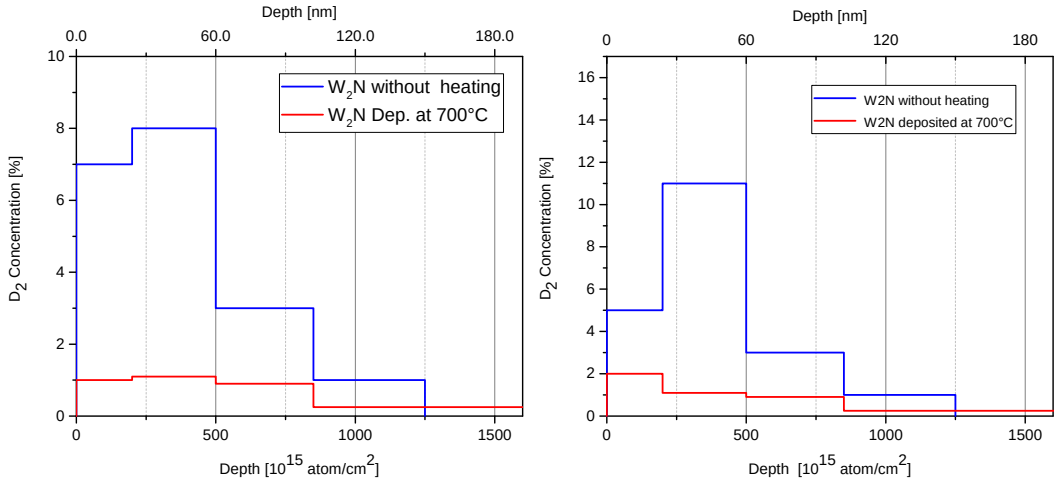

Fig. 5.4 The D_2 depth profile as a comparison between the optimized layer (red line) and the common layer (blue line) up to 180 *nm*. (a) Measured by the proton signal. (b) Deduced from the alpha-particle signal which has better a resolution, however, much less probing depth.

Fig. 5.4 summarizes the depth profiles of both layers. The two depth profiles are calculated based on proton as well as the alpha particles. From that, it can be seen that the deuterium is mainly concentrated in the near-surface region. The diffusion depth is ~ 100 *nm*. Furthermore, the absolute deuterium amount is much less in the layer deposited at elevated temperature compared with the other one deposited without additional heating.

5.3 Deuterium Quantification Using NRA

In this section an example of quantification of the deuterium amount in one of the layers is presented, that will be compared later with TDS results. Fig. 5.5 shows the proton signal of the of the W_2N deposited at $500°C$ substrate temperature (which was discussed earlier in chapter 4). In the figure, both the raw data and the simulation are plotted which are in a good agreement. A summary of the deuterium quantification using both proton and alpha signals, as well as, the average is show in table 5.1.

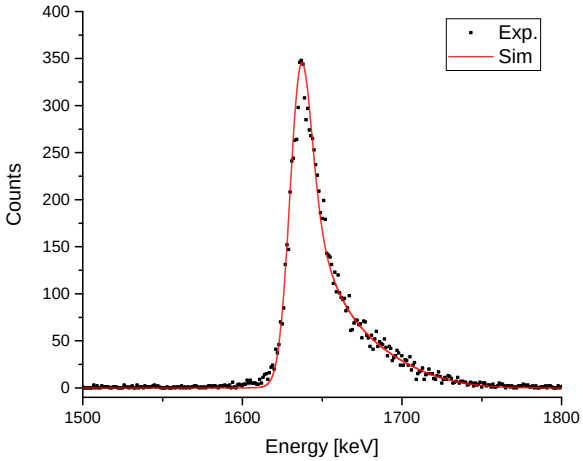

Fig. 5.5 A simulation of the proton signal (red line) resulting from 690 keV $^3He^+$

Table 5.1 A summary of the D_2 amount calculated from the NRA proton and alpha peaks integrals

Detector	Integral $10^{15}\ Atom/cm^2$	Total amount Atoms
Proton	57.4 ± 5.3	5.74×10^{16}
Alpha	64.4 ± 6.1	6.44×10^{16}
		$Avg. \approx 6.09 \pm 0.57 \times 10^{16}$

5.4 Deuterium Quantification Using TDS

Another approach to quantify the deuterium amount is thermal desorption spectroscopy. The optimized layers have shown improvements on the thermal stability which, in turn, shifted the decomposition to higher temperatures. It was possible to record the main deuterium release masses separately before the formation of deuterated nitrogen compounds. Such compounds like ammonia NH_3 can be formed by deuterium resulting in molecules like ND_3, NHD_2 or NH_2D which are very difficult to identify, calibrate or quantify.

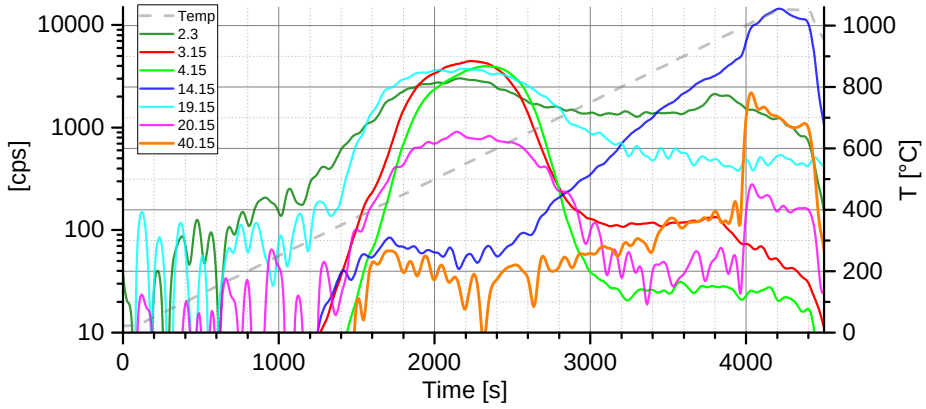

Fig. 5.6 TDS spectrum showing certain recorded masses of a D_2-containing W_2N layer (loaded) plotted on a log scale as a function of time. The oven temperature (light-gray dashed line) is plotted on the right hand side y-axis. The D_2-related masses are $3, 4, 19$ and 20 *amu*. The blue curve is the nitrogen signal mass 14 *amu*.

Fig. 5.6 and Fig. 5.7 show the QMS signals of certain masses plotted in the log scale and the linear scale respectively. This sample is an identical copy of the sample discussed in chapter 4 which is W_2N deposited at $500°C$ substrate temperature. A prior run of the TDS experiment is performed without the sample being inserted to measure the background. Afterwards the background is subtracted from all the plotted spectra. The main masses used for deuterium quantification are 4 *amu* for D_2 and 3 *amu* for HD. Some additional masses which can contain D are 19 *amu* and 20 *amu* are mainly for heavy water HDO and D_2O respectively.

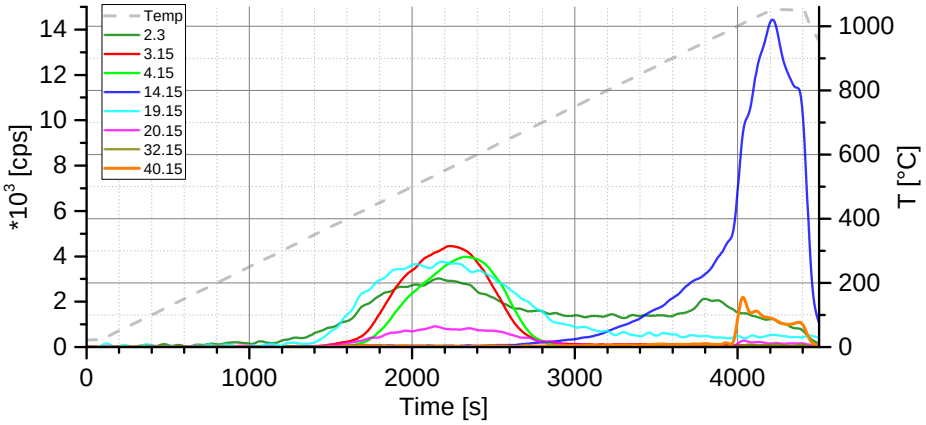

Fig. 5.7 Linear plot of Fig.5.6 showing the behavior of D_2-related masses release in comparison with N_2 (blue line).

The desorption temperature of the D_2 (mass 4 *amu*) is $\sim 380°C$ while the rest of the masses get released a bit earlier $\sim 350°C$ supporting the assumption of that is due to surface contribution. By integrating each spectrum and using the calibration factors for the different masses the total deuterium amount can be concluded. Table 5.2 summarizes the used masses integrals and the corresponding D amount. The uncertainty of the measurements is $\sim 10\%$ mainly from the calibration.

Table 5.2 Summary of D_2 amounts in the measured masses as well as an estimation in the D_2-related molecules (accurate calibration not possible), as well as, the total amount.

Molecule	counts	Atom
D_2	2.62×10^6	1.77×10^{16}
HD	3.11×10^6	1.05×10^{16}
HDO	4.13×10^6	2.09×10^{16}
D_2O	6.17×10^5	3.12×10^{15}
		sum = 5.21×10^{16}

By comparing the obtained value of the total D amount using NRA which is $6.09 \pm 0.57 \times 10^{16}$, it can be seen that the measured value using NRA is 17 % higher than the measured value using TDS. That can lie in the error window of each measurement ($\sim$ 10 %). Despite the taken care during the measurements and the analysis, some other factors limit the achievable accuracy in the evaluation. Among these factors are the current measurements during NRA measurements and the calibration factors for HDO and D_2O for TDS. The calibration factors for these two masses were taken to be the same as H_2O which might be not very correct.

5.5 The Effect on the Micro-Structure

To get an idea about the effects on the surface morphology of the layer and the erosion, Fig. 5.8 shows two SEM images from the surface before and after plasma exposure. The surface seems to be slightly smeared out and sharp edges are somehow smoothed. However, that corresponds to a few *nm*'s erosion which can't be measured by SEM cross section or RBS.

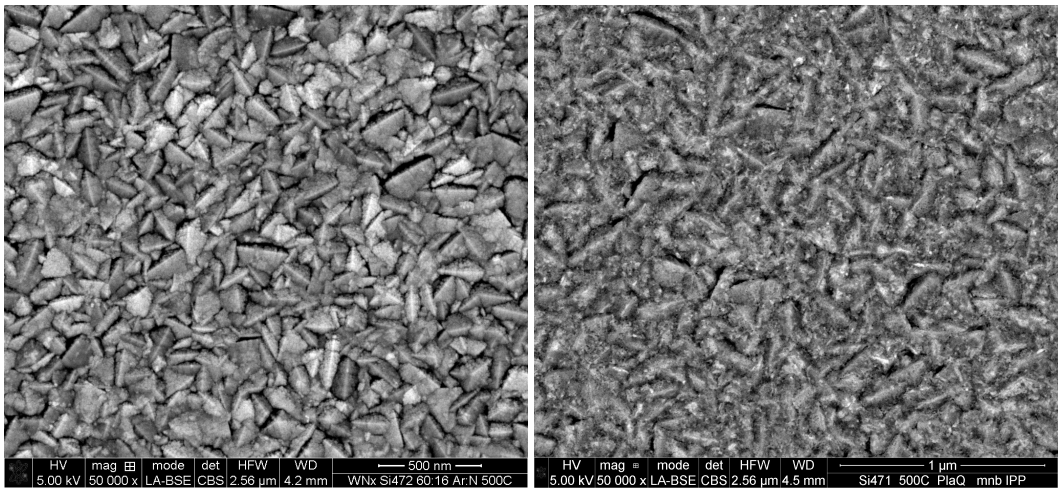

(a) **(b)**

Fig. 5.8 SEM images showing the changes on the surface morphology due to exposure to D_2-plasma. (a) Before exposure. (b) after exposure.

On the other hand, exposure of a layer which has an amorphous structure led to a noticeable erosion as well as surface enrichment of tungsten. Fig. 5.9a shows the RBS spectrum of the surface measured by 800 keV ^3He. In the figure a clear tungsten enrichment on the surface can be seen. Fig. 5.9b shows the surface of this layer after plasma exposure.

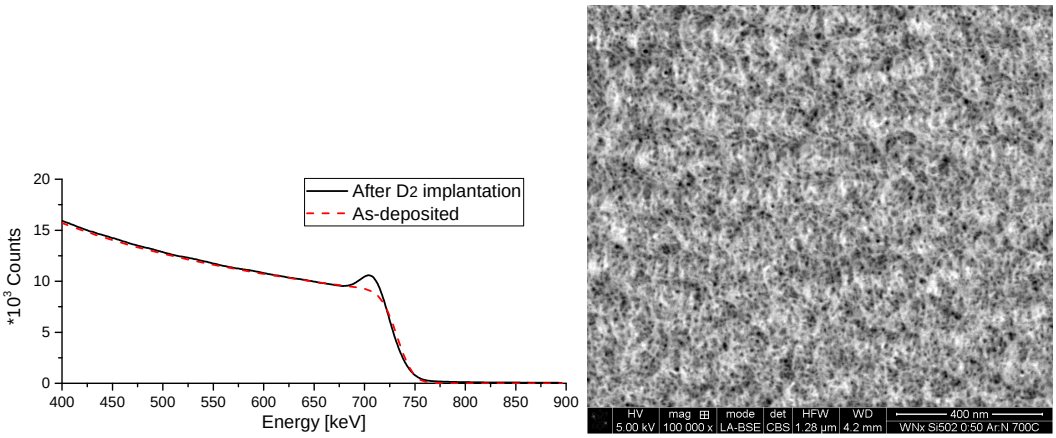

(a) **(b)**

Fig. 5.9 Other layers deposited with pure N_2 as sputtering gas showed preferential sputtering of N_2 and W enrichment on the surface after plasma exposure. (a) Typical RBS spectra of the WN_x peak (zoomed-in) measured at 800 keV $^3He^+$. (b) SEM image of the layer before deposition, however, it is difficult to recognize the difference after the exposure.

5.6 Chapter Summary

Deuterium amount in W_2N due to loading of layers deposited at the optimized conditions were compared with a common layer. The optimized layer has shown higher resistance to deuterium diffusion with diffusion depth ~ 80 *nm*. Moreover, The total retained deuterium amount is also less. Quantification with two independent methods, NRA and TDS, showed a comparable deuterium amount within the uncertainty of both measurements. Furthermore, the optimized layers showed much more resistance to *D*-plasma sputtering.

Chapter 6

Conclusion and Outlook

6.1 Thesis Conclusion

It has been shown through out this thesis, that tungsten nitride, which is produced via magnetron sputtering, can form three stable phases W_2N, WN and WN_2. However the crystallinity of the produced layers is somehow limited. W_2N showed promising properties, therefore the deposition of this phase was further optimized. The optimized W_2N layers showed much better crystallinity and thermal stability than previously produced layers. The grain size of the best layers was $\sim 150\ nm$ which is 15 times larger than what has been reported before. These layers were thermally stable up to $\sim 1000\ ^{\circ}C$ ($\sim 1300\ K$), which is about 500 K higher than previously reported values. It was found that at this temperature a reaction between the silicon substrate and the WN_x layer occurred leading to the formation of WSi_2 was observed. That led to N_2 release from the film, however in a slow process which can be attributed to the interdiffusion of W and Si. That was a novel step towards more robust tungsten nitride films which have potential applications, e.g., in nuclear fusion research. Therefore, the investigation of deuterium retention in the optimized W_2N layers showed that it has much better resistance to deuterium diffusion compared with the layers which has been reported before, which makes these layers a potential diffusion barrier.

6.2 Outlook and Further Experiments

For further investigation of the thermal stability of such layers, a proper substrate has to be used, since the deposited films on silicon are only up to $\sim 1200\ K$. The chemical stability is not the only criterion, but also a proper thermal expansion match has to be taken into account. The thermal stability of such layers can be, thermodynamically, stable up to $\sim 2100\ K$ as it has been reported in the phase diagram of the W-N system. This work showed that can be possible via further optimization.

References

[1] Shahriar Shafiee and Erkan Topal. “When will fossil fuel reserves be diminished?” In: *Energy policy* 37.1 (2009), pp. 181–189.

[2] Alexander Piel. *Plasma physics: an introduction to laboratory, space, and fusion plasmas*. Springer, 2017.

[3] John Stachel and Roberto Torretti. “Einstein’s first derivation of mass–energy equivalence”. In: *American Journal of Physics* 50.8 (1982), pp. 760–763.

[4] Niels Bohr and John Archibald Wheeler. “The mechanism of nuclear fission”. In: *Physical Review* 56.5 (1939), p. 426.

[5] JET Team et al. “Fusion energy production from a deuterium-tritium plasma in the JET tokamak”. In: *Nuclear Fusion* 32.2 (1992), p. 187.

[6] Asher Peres. “Fusion cross sections and thermonuclear reaction rates”. In: *Journal of Applied physics* 50.9 (1979), pp. 5569–5571.

[7] *Cross section*. Accessed: 30 Aug. 2017. URL: http://www.crossfirefusion.com/nuclear-fusion-reactorcrossfire-fusion-reactor.html.

[8] Harmon Craig. “Standard for reporting concentrations of deuterium and oxygen-18 in natural waters”. In: *Science* 133.3467 (1961), pp. 1833–1834.

[9] Roscoe B White. *Theory of tokamak plasmas*. Elsevier, 2017.

[10] *Tokamak*. Accessed: 30 Aug. 2017. URL: fig:https://www.pinterest.com/orlesovvieneilg/tokamak/.

[11] R. Maingi. “3 - Plasma exhaust”. In: *Magnetic Fusion Energy*. Ed. by George H. Neilson. Woodhead Publishing, 2016, pp. 31–59. ISBN: 978-0-08-100315-2. DOI: http://doi.org/10.1016/B978-0-08-100315-2.00003-9. URL: http://www.sciencedirect.com/science/article/pii/B9780081003152000039.

[12] R Neu et al. “Tungsten: an option for divertor and main chamber plasma facing components in future fusion devices”. In: *Nuclear fusion* 45.3 (2005), p. 209.

[13] *Tungsten*. Accessed: 30 Aug. 2017. URL: https://www.ipp.mpg.de/3634236/wolfram.

[14] *Plasma wall interaction*. Accessed: 30 Aug. 2017. URL: http://www.fysik.dtu.dk/english/Research/PPFE.

[15] R. Neu et al. “Tungsten behaviour in radiatively cooled plasma discharges in {ASDEX} Upgrade”. In: *Journal of Nuclear Materials* 415.1, Supplement (2011). Proceedings of the 19th International Conference on Plasma-Surface Interactions in Controlled Fusion, S322–S326. ISSN: 0022-3115. DOI: http://doi.org/10.1016/j.jnucmat.2010.09.036. URL: http://www.sciencedirect.com/science/article/pii/S0022311510005465.

[16] R Neu et al. “Plasma wall interaction and its implication in an all tungsten divertor tokamak”. In: *Plasma Physics and Controlled Fusion* 49.12B (2007), B59.

[17] Jill S Becker and Roy G Gordon. "Diffusion barrier properties of tungsten nitride films grown by atomic layer deposition from bis (tert-butylimido) bis (dimethylamido) tungsten and ammonia". In: *Applied Physics Letters* 82.14 (2003), pp. 2239–2241.

[18] Jean E Kelsey et al. "Low temperature metal-organic chemical vapor deposition of tungsten nitride as diffusion barrier for copper metallization". In: *Journal of Vacuum Science & Technology B: Microelectronics and Nanometer Structures Processing, Measurement, and Phenomena* 17.3 (1999), pp. 1101–1104.

[19] AE Kaloyeros and E Eisenbraun. "Ultrathin diffusion barriers/liners for gigascale copper metallization". In: *Annual review of materials science* 30.1 (2000), pp. 363–385.

[20] K Schmid et al. "Interaction of nitrogen plasmas with tungsten". In: *Nuclear Fusion* 50.2 (2010), p. 025006.

[21] G Soto et al. "Tungsten nitride films grown via pulsed laser deposition studied in situ by electron spectroscopies". In: *Applied surface science* 214.1 (2003), pp. 58–67.

[22] Tomonari Yamamoto et al. "Effects of nitrogen concentration on microstructures of WN x films synthesized by cathodic arc method". In: *Surface and Coatings Technology* 193.1 (2005), pp. 372–374.

[23] Steven D Marcus and RF Foster. "Characterization of low pressure chemically vapor-deposited tungsten nitride films". In: *Thin Solid Films* 236.1-2 (1993), pp. 330–333.

[24] Peter Hones et al. "Structural and mechanical properties of chromium nitride, molybdenum nitride, and tungsten nitride thin films". In: *Journal of Physics D: Applied Physics* 36.8 (2003), p. 1023.

[25] XX Zhang et al. "Thermal stability of tungsten sub-nitride thin film prepared by reactive magnetron sputtering". In: *Journal of Nuclear Materials* 485 (2017), pp. 1–7.

[26] H Chhina, S Campbell, and O Kesler. "Thermal and electrochemical stability of tungsten carbide catalyst supports". In: *Journal of Power Sources* 164.2 (2007), pp. 431–440.

[27] Erik Lassner and Wolf-Dieter Schubert. *Tungsten: properties, chemistry, technology of the element, alloys, and chemical compounds*. Springer Science & Business Media, 2012.

[28] Hugh O Pierson. *Handbook of Refractory Carbides & Nitrides: Properties, Characteristics, Processing and Apps.* William Andrew, 1996.

[29] PJ Kelly and RD Arnell. "Magnetron sputtering: a review of recent developments and applications". In: *Vacuum* 56.3 (2000), pp. 159–172.

[30] H. A. Wriedt. "The N-W (nitrogen-tungsten) system". In: *Bulletin of Alloy Phase Diagrams* 10.4 (1989), pp. 358–367. ISSN: 0197-0216. DOI: 10.1007/BF02877592. URL: http://dx.doi.org/10.1007/BF02877592.

[31] B. Predel. "N-W (Nitrogen-Tungsten)". In: *Li-Mg – Nd-Zr*. Ed. by O. Madelung. Berlin, Heidelberg: Springer Berlin Heidelberg, 1997, pp. 1–4. ISBN: 978-3-540-68538-8. DOI: 10.1007/10522884_2144. URL: https://doi.org/10.1007/10522884_2144.

[32] L Gao et al. "Influence of nitrogen pre-implantation on deuterium retention in tungsten". In: *Physica Scripta* 2014.T159 (2014), p. 014023.

[33] *Magnetron Sputtering Schematics*. Edited, Accessed: 20 Sep. 2017. URL: http://farotex.com/technology.html.

[34] John A Thornton. "Influence of apparatus geometry and deposition conditions on the structure and topography of thick sputtered coatings". In: *Journal of Vacuum Science and Technology* 11.4 (1974), pp. 666–670.

[35] Bernard Dennis Cullity and John W Weymouth. "Elements of X-ray Diffraction". In: *American Journal of Physics* 25.6 (1957), pp. 394–395.

[36] B.D. Cullity. *Elements of X-ray Diffraction*. Addison-Wesley metallurgy series. Addison-Wesley Publishing Company, 1956. URL: https://books.google.co.jp/books?id=XJVCgGFTODMC.

[37] *Braggs Law*. Accessed: 30 Aug. 2017. URL: https://commons.wikimedia.org/wiki/File:Braggs_Law.svg.

[38] *Miller Indices (hkl)*. Accessed: 22 Sep. 2017. URL: http://www.chem.qmul.ac.uk/surfaces/scc/scat1_1b.htm.

[39] *Basic concept of an X-Ray Diffractometer*. Edited, Accessed: 20 Sep. 2017. URL: https://www.spec2000.net/09-xrd.htm.

[40] M.F. Campos et al. "Uncertainty estimation of lattice parameters measured by X-Ray diffraction". In: (Sept. 2006).

[41] R Curtis Bird and James Stanislaus Williams. *Ion beams for materials analysis*. Elsevier, 1990.

[42] Matej Mayer. *Rutherford Backscattering Spectrometry (RBS)*. Accessed: 20 Sep. 2017. URL: http://users.ictp.it/~pub_off/lectures/lns022/Mayer_1/Mayer_1.pdf.

[43] M. Mayer. *SIMNRA User's Guide*. Bericht / 9: Bericht. Max-Planck-Inst. für Plasmaphysik, 1997. URL: https://books.google.de/books?id=-n02HAAACAAJ.

[44] Joseph R Tesmer and Michael Nastasi. "Handbook of modern ion beam materials analysis". In: *Materials Research Society, 9800 McKnight Rd, Suite 327, Pittsburgh, PA 15237, USA, 1995. 700* (1995).

[45] *NRA*. Accessed: 30 Aug. 2017. URL: http://allaboutrutherford.weebly.com/innovations.html.

[46] E. Salançon et al. "Redeposition of amorphous hydrogenated carbon films during thermal decomposition". In: *Journal of Nuclear Materials* 376.2 (2008), pp. 160–168. ISSN: 0022-3115. DOI: http://dx.doi.org/10.1016/j.jnucmat.2008.02.070. URL: http://www.sciencedirect.com/science/article/pii/S0022311508001633.

[47] Rudolf Reichelt. "Scanning electron microscopy". In: *Science of microscopy*. Springer, 2007, pp. 133–272.

[48] *Scanning electron microscope*. Accessed: 30 Aug. 2017. URL: https://www.jeol.co.jp/en.

[49] David B Williams and C Barry Carter. "The transmission electron microscope". In: *Transmission electron microscopy*. Springer, 1996, pp. 3–17.

[50] Peter J Goodhew, John Humphreys, and Richard Beanland. *Electron microscopy and analysis*. CRC Press, 2000.

[51] Lucille A Giannuzzi et al. *Introduction to focused ion beams: instrumentation, theory, techniques and practice*. Springer Science & Business Media, 2006.

[52] Rene Van Grieken and Andrzej Markowicz. *Handbook of X-ray Spectrometry*. CRC Press, 2001.

[53] *Energy Dispersive Spectrometer*. Accessed: 31 Aug. 2017. URL: http://mcff.mtu.edu/acmal/electronmicroscopy/MA_EDS_Basic_Science.htm.

[54] Ch D Wagner. *Handbook of X-ray photoelectron spectroscopy*. Perkin-Elmer, 1979.

[55] *XPS*. Accessed: 30 Aug. 2017. URL: http://jacobs.physik.uni-saarland.de/english/instrumentation/uhvl.htm.

[56] Th Nelis and R Payling. "Glow Discharge Optical Emission Spectrometry". In: *Surface Analysis Methods in Materials Science*. Springer, 2003, pp. 553–559.

[57] *RF glow discharge optical emission spectroscopy*. Accessed: 31 Aug. 2017. URL: http://www.nanoanalysis.co.jp/en/business/case_example_93.html.

[58] William N Sharpe. *Springer handbook of experimental solid mechanics*. Springer Science & Business Media, 2008.

[59] W.C. Oliver and G.M. Pharr. "An improved technique for determining hardness and elastic modulus using load and displacement sensing indentation experiments". In: *Journal of Materials Research* 7.6 (1992), pp. 1564–1583. DOI: 10.1557/JMR.1992.1564.

[60] *Nanomechanical Testing Probes*. Accessed: 31 Aug. 2017. URL: https://www.bruker.com/products/surface-and-dimensional-analysis/nanomechanical-test-instruments/nanomechanical-upgrade-options/test-probes.html.

[61] Fiala. "Beta W2N". In: *Central Research Institute, SKODA, Czechoslovakia* (1975).

[62] YG Shen et al. "Composition, residual stress, and structural properties of thin tungsten nitride films deposited by reactive magnetron sputtering". In: *Journal of Applied Physics* 88.3 (2000), pp. 1380–1388.

[63] Bernard Borie. "X-Ray Diffraction in Crystals, Imperfect Crystals, and Amorphous Bodies." In: *Journal of the American Chemical Society* 87.1 (1965), pp. 140–141.

[64] T Migita et al. "Effect of dc bias on the compositional ratio of WN X thin films prepared by rf-dc coupled magnetron sputtering". In: *Applied surface science* 169 (2001), pp. 362–365.

[65] C.J.M. Denissen, J. Liebe, and M. van Rijswick. "Recrystallisation temperature of tungsten as a function of the heating ramp". In: *International Journal of Refractory Metals and Hard Materials* 24.4 (2006). Selected presentations from the 16th International Plansee Seminar 2005, pp. 321–324. ISSN: 0263-4368. DOI: http://dx.doi.org/10.1016/j.ijrmhm.2005.10.012. URL: http://www.sciencedirect.com/science/article/pii/S0263436805001447.

[66] *Tungsten Nitride Density*. Accessed: 25 Oct. 2017. URL: http://www.reade.com/products/tungsten-nitride-powder-tungsten-nitridetargets-wn-and-wn2.

[67] Victor E Borisenko and Peter J Hesketh. "Diffusion Synthesis of Silicides in Thin-Film Metal—Silicon Structures". In: *Rapid Thermal Processing of Semiconductors*. Springer, 1997, pp. 149–191.

[68] Alex Lahav, Karen A Grim, and Ilan A Blech. "Measurement of thermal expansion coefficients of W, WSi, WN, and WSiN thin film metallizations". In: *Journal of applied physics* 67.2 (1990), pp. 734–738.

[69] Yasumasa Okada and Yozo Tokumaru. "Precise determination of lattice parameter and thermal expansion coefficient of silicon between 300 and 1500 K". In: *Journal of applied physics* 56.2 (1984), pp. 314–320.

[70] WC Morgan. "Thermal expansion coefficients of graphite crystals". In: *Carbon* 10.1 (1972), pp. 73–79.

[71] John W Hutchinson. "Stresses and failure modes in thin films and multilayers". In: *Notes for a Dcamm Course. Technical University of Denmark, Lyngby* (1996), pp. 1–45.

[72] David Nečas and Petr Klapetek. "Gwyddion: an open-source software for SPM data analysis". In: *Open Physics* 10.1 (2012), pp. 181–188.

[73] YG Shen et al. "Structural properties and nitrogen-loss characteristics in sputtered tungsten nitride films". In: *Thin Solid Films* 372.1 (2000), pp. 257–264.

[74] Claude A Klein. "How accurate are Stoney's equation and recent modifications". In: *Journal of Applied Physics* 88.9 (2000), pp. 5487–5489.

[75] YG Shen et al. "Residual stress, microstructure, and structure of tungsten thin films deposited by magnetron sputtering". In: *Journal of Applied Physics* 87.1 (2000), pp. 177–187.

[76] A Manhard, T Schwarz-Selinger, and W Jacob. "Quantification of the deuterium ion fluxes from a plasma source". In: *Plasma Sources Science and Technology* 20.1 (2011), p. 015010.

[77] L. Gao et al. “Deuterium implantation into tungsten nitride: Negligible diffusion at 300K”. In: *Journal of Nuclear Materials* 451.1 (2014), pp. 352–355. ISSN: 0022-3115. DOI: https://doi.org/10.1016/j.jnucmat.2014.04.029. URL: http://www.sciencedirect.com/science/article/pii/S002231151400244X.

[78] V.Kh. Alimov, M. Mayer, and J. Roth. “Differential cross-section of the D(3He,p)4He nuclear reaction and depth profiling of deuterium up to large depths”. In: *Nuclear Instruments and Methods in Physics Research Section B: Beam Interactions with Materials and Atoms* 234.3 (2005), pp. 169–175. ISSN: 0168-583X. DOI: https://doi.org/10.1016/j.nimb.2005.01.009. URL: http://www.sciencedirect.com/science/article/pii/S0168583X05000121.

Appendix A

RBS and NRA Cross Section Data

A.1 RBS N_2 Cross Section

In addition to the low cross section of N_2, it also has high uncertainty as it has always been measured in a compound. It is not easy to measure the cross section of N_2 in it's gaseous form. Therefore different cross sections were reported. Fig. A.1 shows the first resonance peak of N using $^4He^+$ from different sources at angle of $165° \pm 5°$. Consequently that will change the simulation which will, in turn, change the simulated value of nitrogen amount in the range of ± 20 %. Therefore using only the cross section of W was used. Fig. A.2 shows the corresponding SIMNRA simulations of a WN_x layer on C substrate using 3.8 Mev $^4He^+$ using different cross sections.

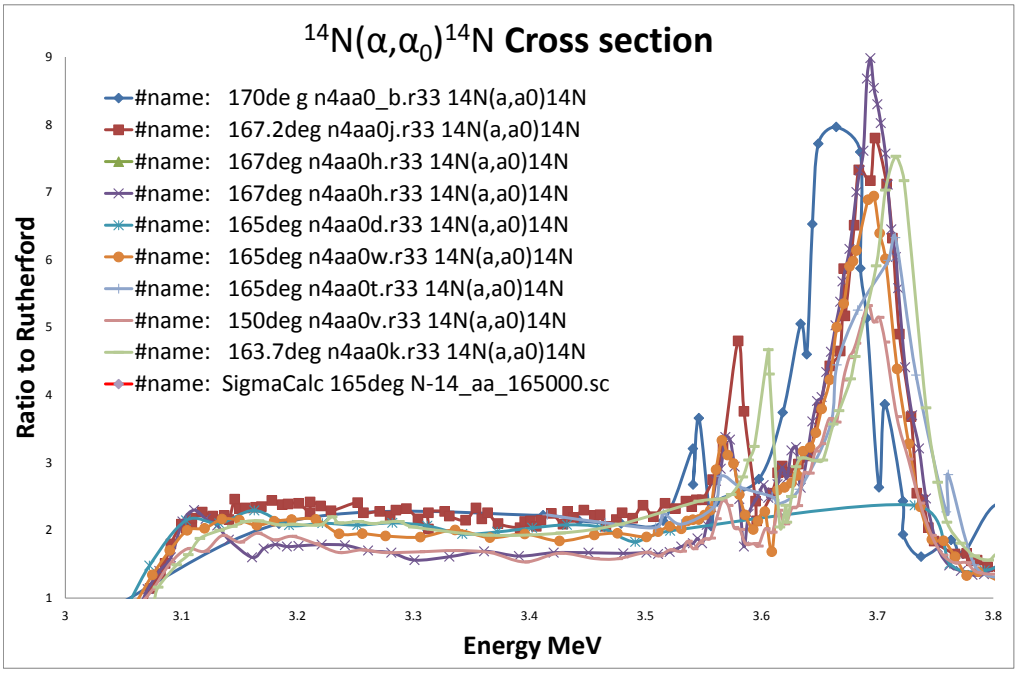

Fig. A.1 Multiple RBS cross section data for ^4He at angle of $165^\circ \pm 5^\circ$ which show the the uncertainty.

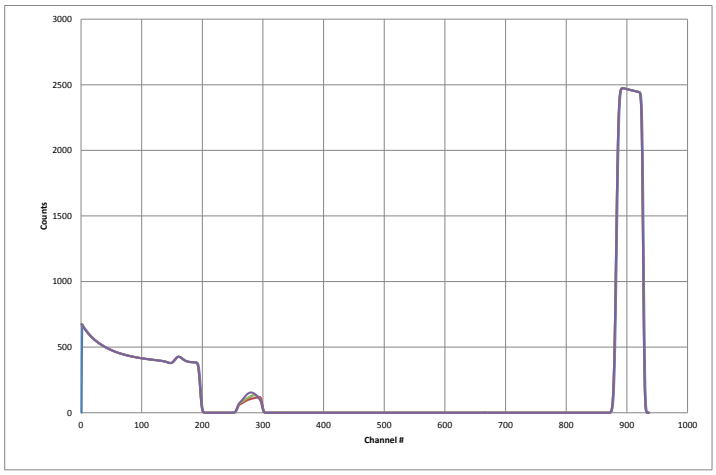

(a)

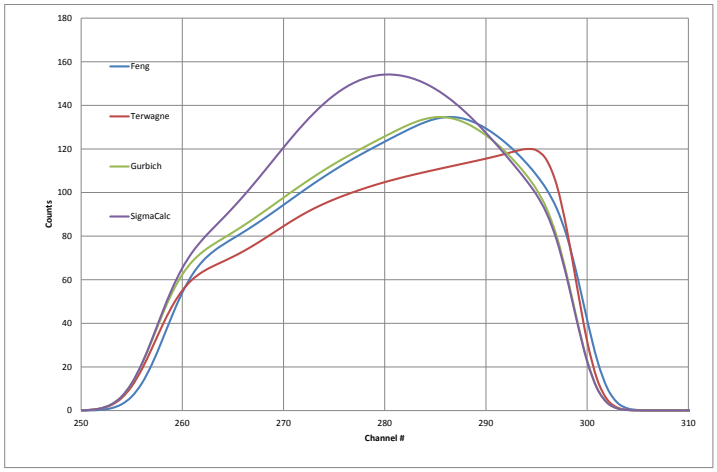

(b)

Fig. A.2 (a) SIMNRA simulations of a WN_x layer on C substrate using 3.8 Mev $^4He^+$ using different cross sections. (b) Zoom-in to the nitrogen peak shows the effect of using different cross sections.

A.2 RBS Cross Section of N_2, Si and C

It's important to choose the beam energy depending on the substrate. That's in case of the overlapping of the nitrogen signal with the substrate. Fig. A.3 shows the cross sections of N, Si and C.

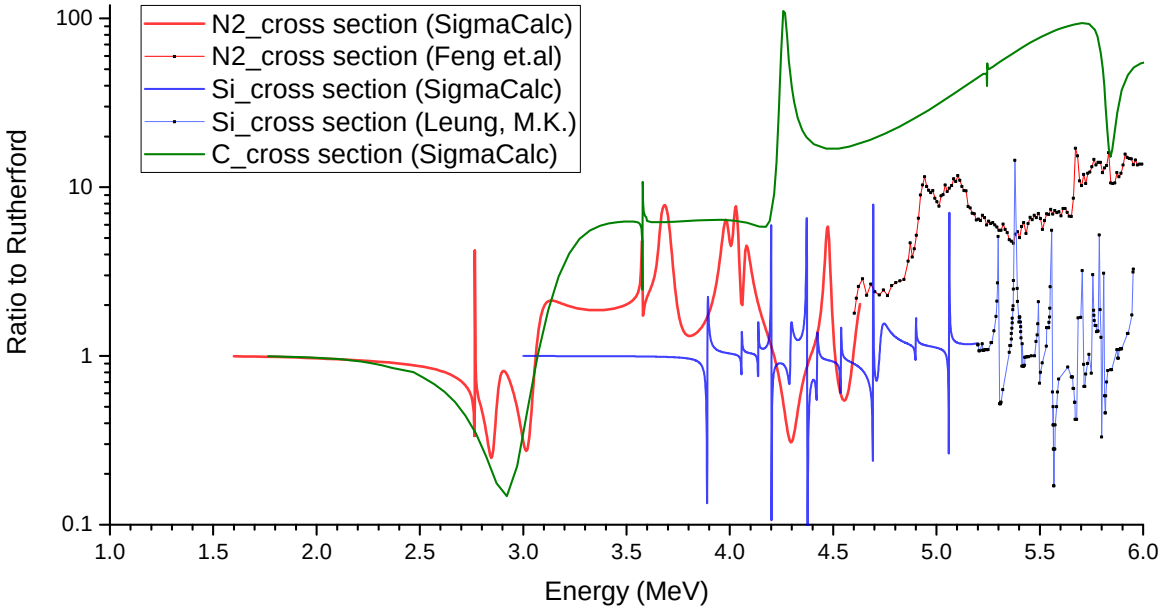

Fig. A.3 RBS cross section data of *N*, *Si* and *C*

A.3 NRA

The used *N*-cross-sections for NRA analysis are shown in Fig. A.4.

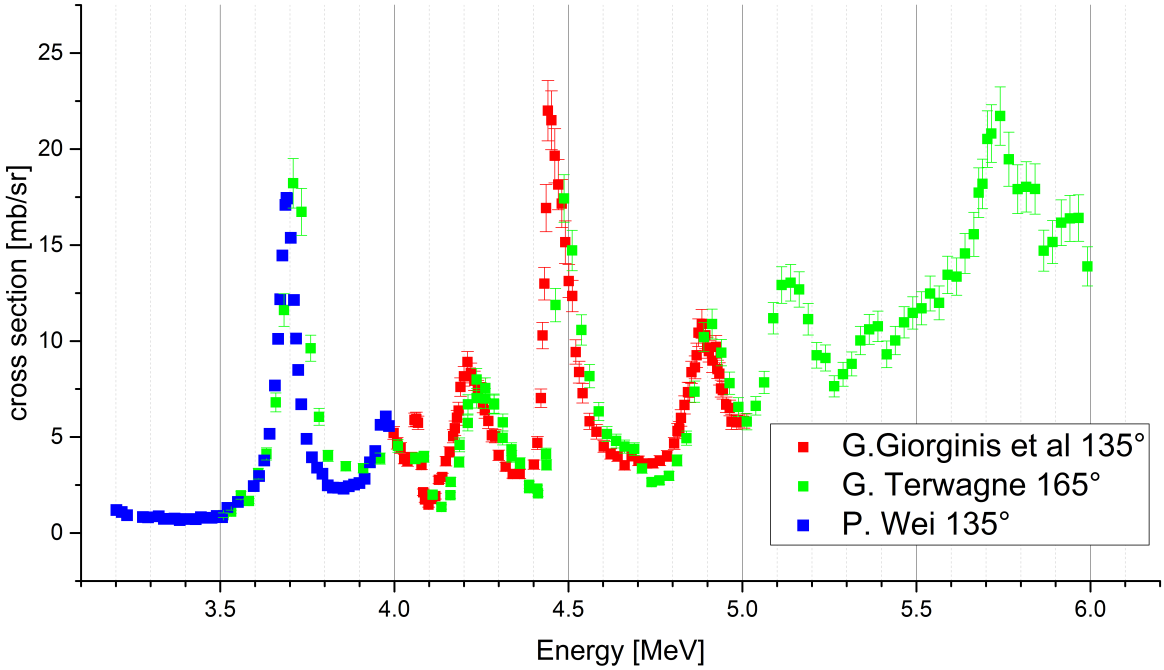

Fig. A.4 NRA cross section data of the reaction $^{14}N(\alpha, p_0)^{17}O$.

Appendix B

Specimen Preparation Using FIB

The process of fabrication TEM lamellas is shown briefly in figures taken using SEM during fabrication.

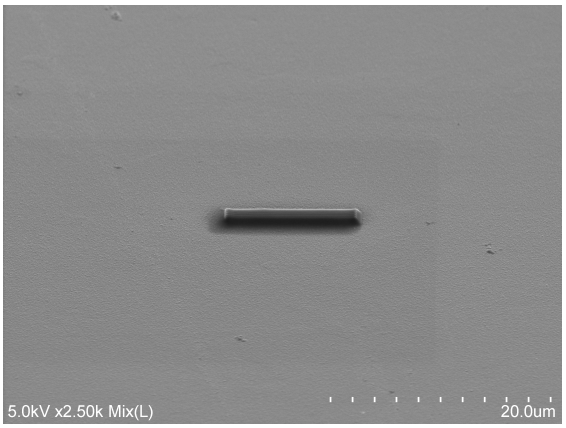

(a) Carbon coating

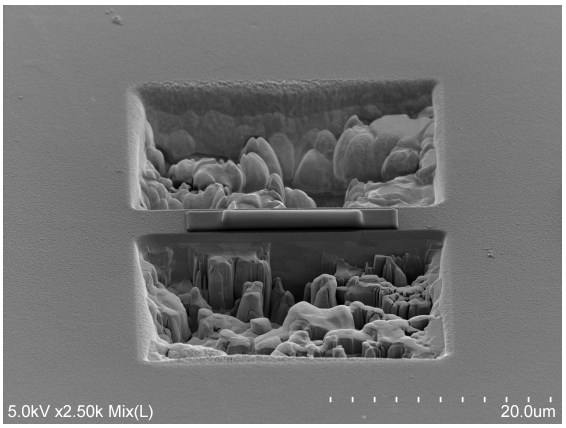

(b) Tungsten coating and sputtering

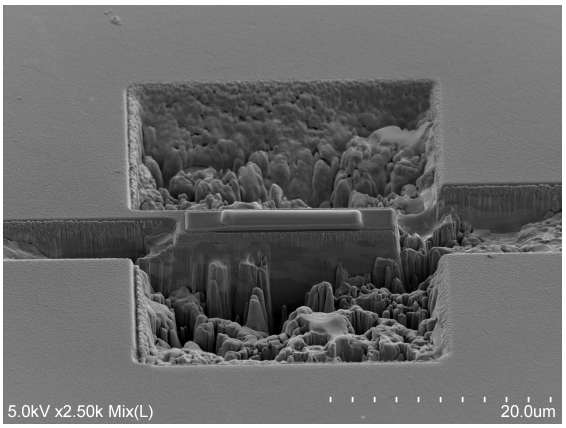

(c) Deep cutting from all sides

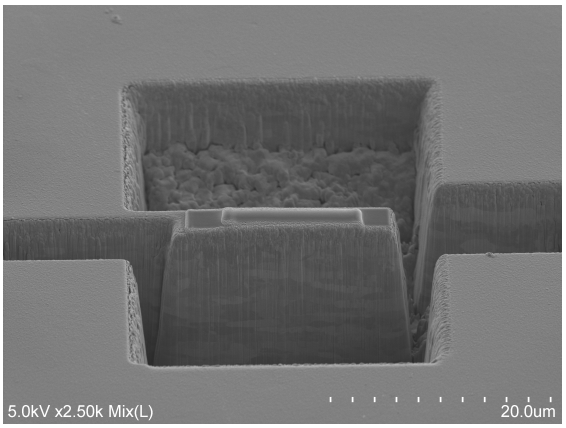

(d) Suitable and clean depth

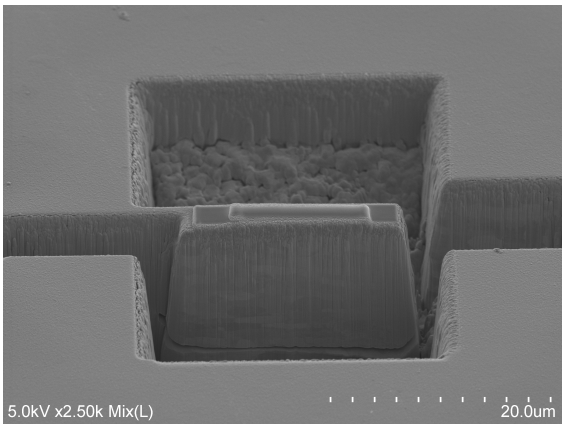

(e) Horizontal cut

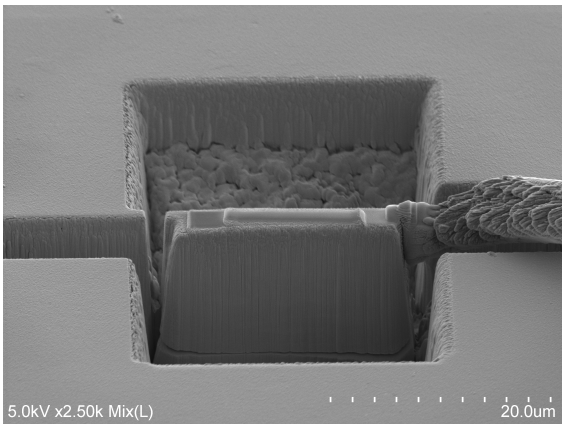

(f) Needle inserted

Fig. B.1 TEM lamellas fabrication process part I

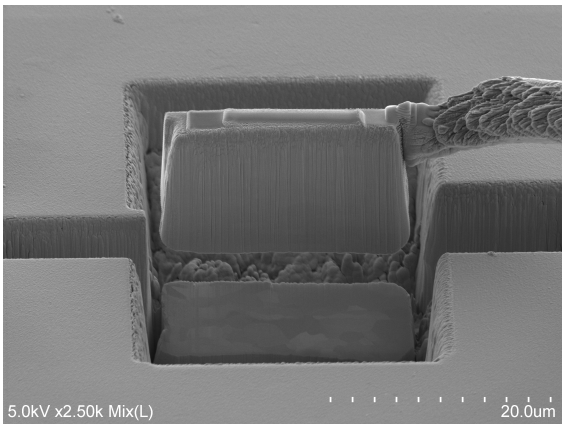

(a) Lamella freed from the sample

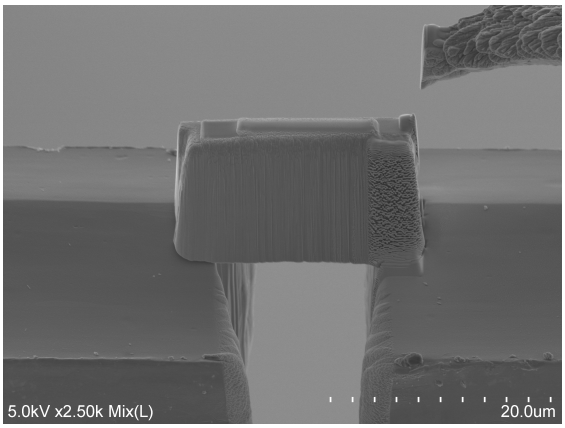

(b) Lamella placed on a *Mo* holder and soldered

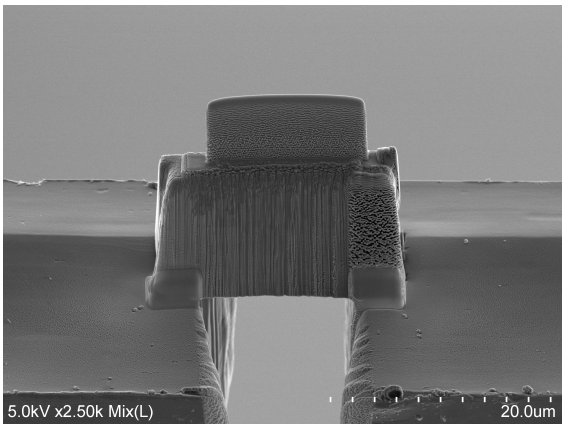

(c) Further soldering and thick *W* coating

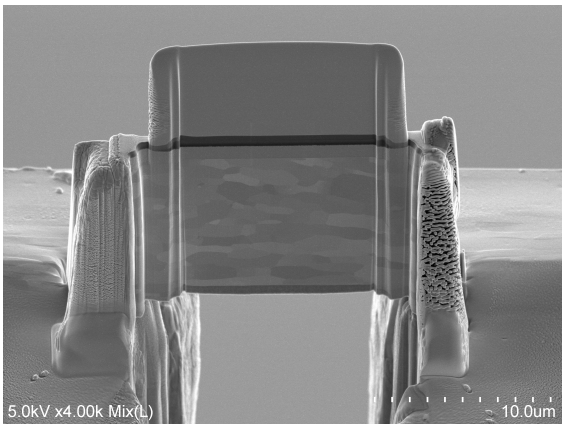

(d) Cutting extras for suitable shape

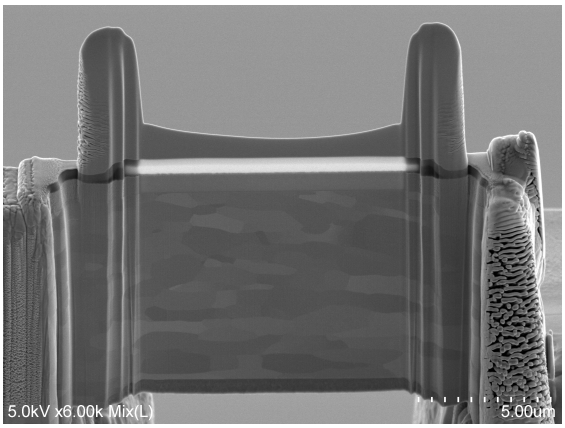

(e) Thinning down

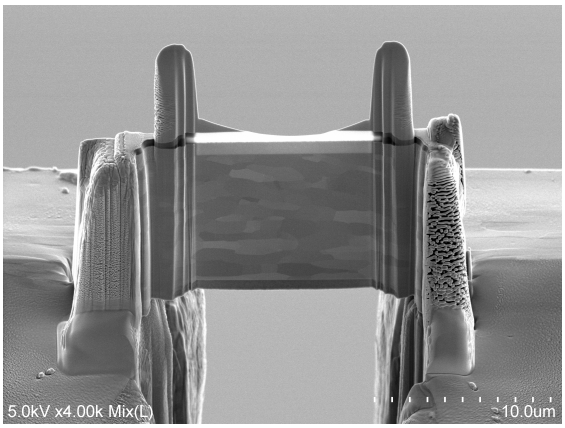

(f) ~ 50 *nm* thickness is achieved

Fig. B.2 TEM lamellas fabrication process part II